Final Project Report

Contractor:	General Electric Company d/b/a GE Research
Project Title:	Impact of Low-Level Jets on Atlantic Coast Offshore Wind Farm Performance
Agreement Number:	147504
Agreement Effective Date:	May 1, 2020
Date of the Report:	June 30, 2023

Prepared for:

The National Offshore Wind Research and Development Consortium

Albany, NY

Melanie Schultz
Program Manager

Prepared by:

General Electric Company, GE Research

Niskayuna, NY

Dr. Balaji Jayaraman

Senior Research Scientist

Contributors: Dr. Tanmoy Chatterjee (GE) and Dr. Shashank Yellapantula (NREL)

Notice

This report was prepared by General Electric Company, GE Research in the course of performing work contracted for and sponsored by the New York State Energy Research and Development Authority and U.S. Department of Energy's Office of Energy Efficiency and Renewable Energy (EERE) (hereafter the "Sponsors") under the Wind Energy Technologies Office Award Number DE-EE0008390.

Preferred Citation

New York State Energy Research and Development Authority (NYSERDA). 2022. "Milestone 4.2 Report – Impact of Low-Level Jets on Atlantic Coast Offshore Wind Farm Performance," NYSERDA Report Number xx-yy (added by NYSERDA). Prepared by General Electric Company, GE Research, Niskayuna, NY. nyserda.ny.gov/publications

Table of Contents

List of Figures

List of Tables

Acronyms and Abbreviations

AEP	Annual Energy Production
AMR-Wind	AMR-Wind wind farm flow modeling software
CART	Controls Advanced Research Turbine
CC	Cumulative Curl model
CPC	Collective Pitch Control
CW	Clockwise
CCW	Counter Clockwise
DEL	Damage Equivalent Loads
DOF	Degree of freedom
DTU	Technical University of Denmark
ExaWind	ExaWind software suite for wind farm flow modeling
IEA	International Energy Agency
IPC	Individual Pitch Control
LES	Large-eddy simulation
LLJ	Low-level jet
LSS	Low-speed Shaft
MBC	Multi-body Coordinate Transform
MMC	Mesoscale-to-microscale coupling
MS	Monotonically sheared
NREL	National Renewable Energy Laboratory
OOP	Out-of-plane
OpenFAST	OpenFAST aeroelastic wind turbine modeling software
PSD	Power Spectral Density
RD	Rotor Diameter
RNA	Rotor-nacelle assembly
ROSCO	(NREL) Reference Open-Source Controller
SISO	Single Input Single Output
WS	Wind Speed

Executive Summary

This is the final report for the project titled "Impact of Low-Level Jets on Atlantic Coast Offshore Wind Farm Performance" funded by the National Offshore Wind Research & Development Consortium (NOWRDC). This effort originated from energy industry needs for site- and condition-specific windfarm modeling to improve simulation-driven estimation of performance and reliability metrics. In conjunction with this technological need, the burgeoning offshore wind installations in the New York Bight and the associated turbine design interest for manufacturers such as GE required more nuanced understanding of the offshore environment and its impact on wind turbine arrays. To this end, as part of this project, we characterized the impact of North Atlantic coastal low-level jets on offshore wind installations through high-fidelity simulations. In particular, coastal low-level jets (LLJ) are mesoscale-driven wind events associated with a non-monotonic velocity profiles whose maximum value occurs at the so-called "jet nose", producing bands of strong positive shear below the nose and a corresponding negative shear above it.

In this project, we accomplished the following tasks:

- Characterize the feature of North Atlantic Low-level jets using buoy-mounted lidar data
- Assess ability of weather-scale modeling tools to characterize LLJ features and develop/validate methods for high-fidelity turbulence resolving models of LLJ wind environments using LES.
- Develop necessary advances within the Exawind suite of tools to simulate at high-fidelity and system-level complexity (aero-servo-elastic turbine representations), the interactions between LLJ turbulence and windfarm systems.
- Analysis and characterization of windfarm system response to LLJ turbulence relative to canonical atmospheric conditions.
- Exploration of control-based mitigation strategies to minimize the deleterious effects of LLJs
- Assessment of the state-of-the-art low-fidelity models used in industry for their ability to capture the complex atmospheric-turbine interactions.

Analysis outcomes show that low-level jets primarily impact windfarms similar to stable boundary layers resulting in deep wakes and strong veer and sheer- induced out-of-plane loads. The deep wakes result in available power for capture by downstream turbines which result in AEP drops. The higher out-of-plane loads arise from the strong veer and shear causing varied responses across the rotor disk and thereby, higher fluctuations in the loads. Our efforts at mitigation show that pitch control operating at the individual blade level can reduce the loads with little reduction in generated power. We also observe that yaw deflections under such environments produce nuanced outcomes under such environments.

1 Project Overview

The wind energy industry is increasingly looking at site- and condition-specific windfarm modeling to improve simulation-driven estimation of performance and reliability metrics. This requires algorithmic, theoretical and computational advances in microweather prediction where one can generate (and ultimately, predict) microscale (scales of O(1m)-O(100m)) atmospheric turbulence at a chosen spatial coordinate and time window on demand. The motivations underlying this demand can be wide ranging, including evaluation of critical design choices under specific conditions of extreme or atypical nature, characterizing performance of specific turbine systems at a given geographic site and so on. Historically, investigation of microscale atmospheric physics of relevance to wind farm operations focused on idealized equilibrium boundary layers due to the inability to model realistic surface layer turbulence in all its complexity. On the other hand, the mesoscale modeling community focused on realistic meteorological predictions. To accomplish the above goals of realistic atmosphere-windfarm interactions, the gap between idealized representation of microscale atmospheric physics and realistic mesoscale meteorology has to be bridged. In this NOWRDC funded project (with GE Offshore Wind cost share), we attempted to characterize the interactions of North Atlantic coastal low-level jets with offshore windfarms representative of the NY Bight. To this end, we adopted a three-step plan for this project as in Figure 1.

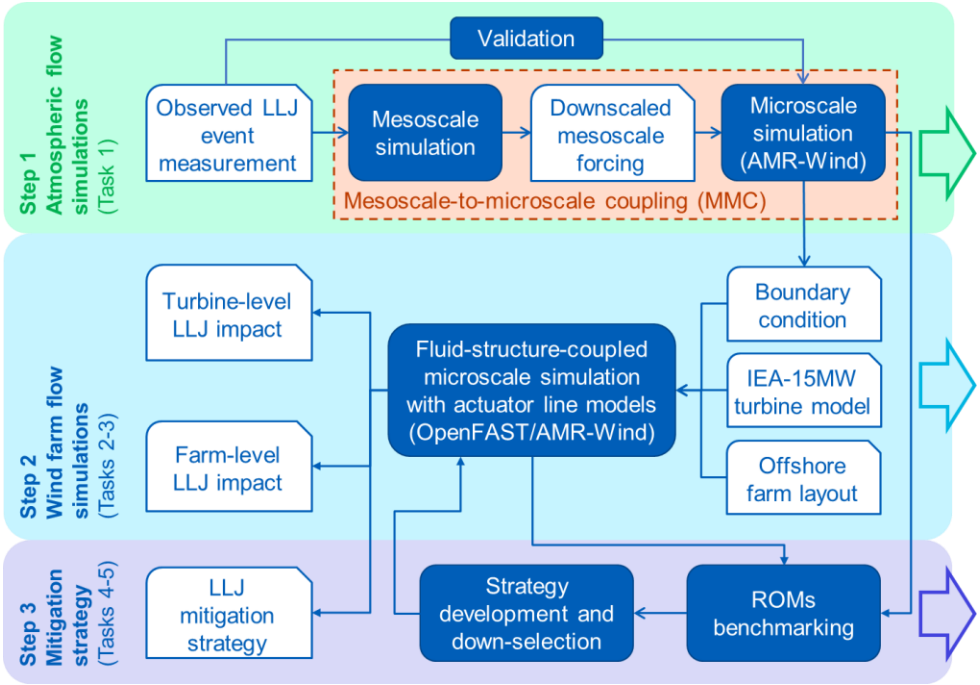

Figure 1: High-fidelity atmospheric flow and wind farm flow simulations in Tasks 1-5 of the project.

In step 1, we characterize the atmospheric flow representative of the NY bight through analysis of site measurements made available by the New York State Energy Research and Development Authority (NYSERDA) as part of the efforts to advance offshore wind deployment in the region. Our analysis of these buoy-mounted LIDAR measurements within the lowest 200m marine Atmospheric Boundary Layer (ABL) in the New York Bight has shown that low-level jets (LLJs) occur 2-7% within a year and as high as 20% in the summer months. Naturally, the criteria to identify LLJs has some impact on these estimates, but the takeaway is that LLJs can impact windfarm operations and wind turbine reliability as a non-mainstream, but likely wind event. The second part of this stage in the project is to evaluate the state-of-the art in modeling LLJs and the associated turbulence. We evaluated the capability of mesoscale modeling tools such as Weather Research and Forecasting (WRF) to predict the LLJ wind profiles and observed reasonable match for periods of interest. Although WRF predictions match the field data, they are typically simulated on coarse grids relative to the most energy containing turbulence scales within the atmospheric surface layer and therefore characterized as not turbulence resolving. In the last decade, there have been attempts to bridge complex mesoscale meteorology (at the kilometer scale) and microscale turbulence resolving predictions (scale O(few meters)) by leveraging the vast history of data-assimilation based ideas from the weather forecasting realm. Specifically, we implemented a profile-assimilation-based coupling framework (first developed in Allaerts et al. (2020)) to couple the meso- and microscales of atmospheric turbulence - a robust engineering approach towards incorporating non-stationary and non-equilibrium mesoscale effects into microscale modeling. We implemented this meso-micro-coupling in the GPU-acceleration capable Exawind compute stack to perform large-eddy simulation (LES) of the microscale atmospheric boundary layer. The challenge with downscaling of turbulence to the microscale from non-turbulence resolving mesoscale simulations is that it is inherently an under-constrained inverse problem with multiple solutions possible. Our analysis in section 2.3 illustrates this aspect of these state-of-the-art techniques where the predicted turbulence state can differ in its intensity and assimilation depending on the choice of assimilation strategy for the temperature data which can result in very different buoyancy-driven turbulence structure. However, the different downscaling methods explored were able to generate a turbulent flow field which in the mean can match the mesoscale wind profiles from WRF on account of its direct assimilation into the LES. This allows us to generate turbulent fields somewhat representative of realistic conditions measured in the field, but more in-depth research is needed to better understand the sensitivity of the different model choices in predicting the higher-order details of the predicted turbulence.

Tasks 2 and 3 represent step II of this project where we applied Mesoscale-to-Microscale Coupling (MMC) to aeroelastically-coupled wind farm flow LES simulations to elucidate the impact of LLJ events

on the performance and loads of a single offshore wind turbine, a single array of five turbines and finally, a multi-array farm of twenty wind turbines. However, to accomplish this, we needed to realize a series of technical advances within the Exawind capability as itemized below:

1. Implement inhomogeneous boundary conditions in the horizontal directions to model finite-sized windfarms
2. Develop the interface to feed meso-micro-coupled ABL turbulence data generated from a precursor simulation with the finite-sized windfarm simulation with inhomegenous boundaries.
3. Develop capability for restarting simulations at the system-level, i.e. the aero/fluid, servo and elastic modules.

These were accomplished with much effort and reported in section 3. In section 4, we report the key simulations executed using this virtual windfarm simulation capability (as part of task 2/3) and identify the key learnings in particular detail. At a high level, we observed that the presence of strong shear and veer in the low-level jet produces asymmetric load distributions across the rotor disk resulting in higher mean and damage-equivalent fatigue loads of the out-of-plane moment variety. We observe that these load increases are associated with losses in power capture ability (relative to rated capacity) due to the persistent deep wakes within the windfarm operating in a low-level jet environment. We particularly note that these observations were qualitatively like that observed for canonical stable atmospheric boundary layer turbulence and therefore, any mitigation approaches developed in this project will apply broadly to the class of stable atmospheric conditions encountered in the offshore setting.

Tasks 4 and 5 represent step III of this project where the high-fidelity dataset from the simulations in steps I and II are being leveraged in two-different ways: (i) assess (and improve) the performance of low-order models relevant to simulation of windfarms and (ii) identify the deleterious impact of LLJ on wind farm performance (loads, power capture) and explore mitigation concepts. The latter aspect is presented in detail in section 5 where we executed both preliminary evaluation of the effectiveness of the different LLJ mitigation strategies on single turbines using standalone decoupled analysis as well as coupled LES of single array windfarm simulations. The different mitigation strategies explored include,

- Derating of wind turbines within a windfarm for modulating wake persistence and loads
- Controlling individual blade pitch operation for wake and load modulation.
- Steering of upstream wakes to ensure performance improvements in downstream wakes.

While, the standalone decoupled single wind turbine analysis turned out to be an effective and inexpensive way to identify broad performance trends, the details of these mitigation strategies on turbine and farm performance showed different outcomes when adopting fully coupled medium-to-higher fidelity models. Specifically, the fully-coupled simulations allowed us to interpret the coupled dynamics of the

turbulent inflow, turbine response and the wake which resulted in quantitatively different performance characteristics, thus highlighting the need for medium-higher fidelity modeling. This need for medium-higher fidelity modeling is more systematically explored in section 6 as part of our systematic efforts to characterize the accuracy of the different models spanning the range of fidelity levels. While significant progress was achieved in our understanding of the impact of low-level jets and stable atmospheric environments on windfarm performance using LES, there do exist challenges that are yet to be overcome before such virtual windfarm capabilities can contribute to mainstream design – namely, computational cost, fidelity of multiscale atmospheric modeling and turbine representations.These aspects will be summarized in section 7.

2 Understanding Wind Resource Modeling and Low-level Jets

2.1 Analysis of Observational Data

Along the north US Atlantic coastline several meteorological and oceanographic (metocean) measurement datasets were investigated to study wind characteristics and LLJ events typical of the US Atlantic Coast. All the datasets were evaluated to meet the following criterion: (1) data should be continuous over a long enough period of time, (2) data should be taken in areas that are not too close to the coast and thus representative of conditions that will be experienced by actual offshore wind farms, (3) data included a range of heights relevant to offshore rotor layers, and (4) data was available to the public. After some detailed analysis, we decided to consider the dataset acquired by the campaign funded by New York State Energy Research and Development Authority (NYSERDA), in which two floating lidar buoys were deployed in the New York Bight within two current Bureau of Ocean Energy Management (BOEM) wind energy call Areas.

For this campaign funded by (NYSERDA), two motion-compensated floating lidar systems were commissioned. These two buoys were validated, first onshore against an onshore met mast, and then offshore against an offshore met mast, in terms of mean wind speed and mean wind direction measurement accuracy. Unfortunately, the current lidar remote sensing technology does not yet provide accurate enough turbulence measurement. These buoys include near-surface (2 m above mean sea level, MSL) meteorological and sea-state measurements, as well as lidar measurements of wind speed and wind direction at 10 levels from 20 to 200 m above MSL. The buoy “E05” located in the “Hudson North” call area will be referred to as the “North Buoy”, and “E06” in the “Hudson South” call area the “South Buoy” (Figure 2).

Measurements collected within a year from September 2019 to August 2020 were considered in the following analysis. A data quality assurance procedure, similar to what was done in the work of Schultz [11] and Nybø et al. [12], is performed on the data before they are admitted into the analysis. Missing data and data that have failed the quality check are replaced by a NaN value.

Before listing the LLJ identification criterions a few terminologies used throughout the document are first introduced below.

a. Jet nose: the location of peak wind speed (U_{nose}) in a profile. If multiple peaks exist, the location of the maximum wind speed is the jet nose.
b. Jet top: the location of the first local wind speed minimum (U_{top}) above the jet nose.

c. Jet wind speed drop-off: the difference in wind speed between the jet nose and the jet top ($\Delta U_{drop}=U_{nose}-U_{top}$).

To fully quantify occurrences of low-level-jets (LLJ) along NY coastline, a set of criterions for detecting 10-min LLJ observations were used in the present study, largely following the recent work of Debnath et al. [13].

1) The wind speed at 140 m is no less than 3 m/s, to exclude observations that are below the cut-in wind speed for the IEA 15MW reference offshore wind turbine which has a hub height of 150 m ([11]).
2) The jet wind speed drop-off ΔU_{drop} is no less than 1.5 m/s, and the non-dimensional drop-off $\Delta U_{drop}/U_{nose}$ is no less than 10%, to exclude very flat jet profiles.

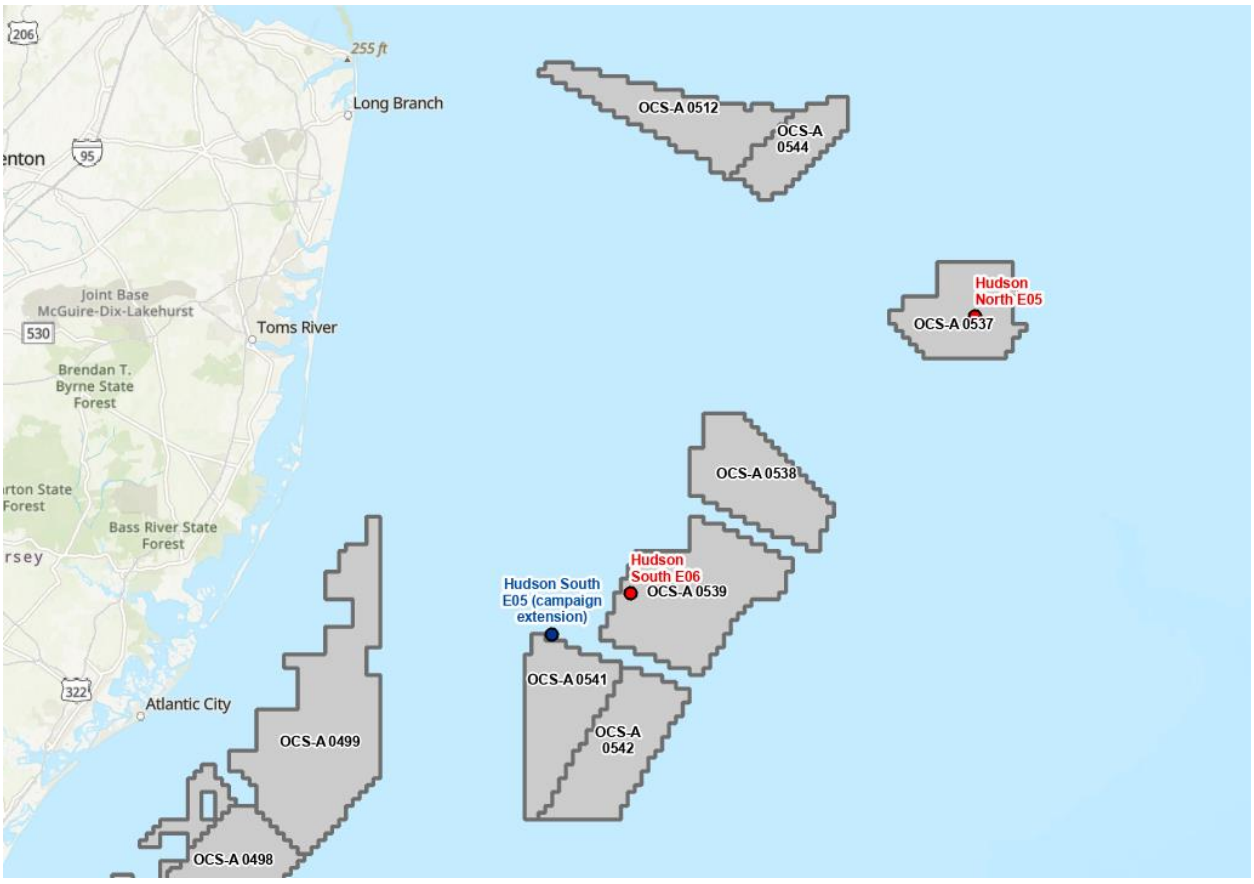

Figure 2: Regional map of the BOEM wind energy lease areas and location of the NYSERDA floating lidar buoys.

Using the criteria above, 1252 (2.4%) out of the 51821 10-min observations recorded at the South Buoy, and 1244 (2.4%) out of the 52704 10-min observations recorded at the North Buoy within a year, are identified as LLJ observations. On top of these detected LLJ observations, following Debnath et al. [13],

an additional search was done to find LLJ periods, defined as consecutive 10-min LLJ observations persisting for at least 1 hour. In total, 57 and 55 LLJ periods were found at the South and North Buoys, respectively.

Figure 3 shows wind roses measured by the lidar at 140 m above MSL at both buoys. All observations – with and without LLJ – as well as LLJ observations are shown. The wind roses are nearly identical at two buoys due to the close distance between them (approximately 77 km). Non-jets dominate at both locations; their 10-min mean wind speed profiles largely conform to an approximately log-law or power-law shape that is typically developed within the surface layer (or Prandtl layer) of the atmospheric boundary layer (ABL), although it is quite possible that many also include part of the Ekman layer as the marine ABL (MABL) can be much shallower than over land (Emeis & Türk [14]). The LLJ observations are concentrated in south-to-southwest sectors with an average wind direction of 224° and 221° for the North and South Buoys, respectively. This wind direction is roughly parallel to the coastline. Coastline-parallel LLJ are frequently reported in the Californian coast and have been attributed by Parish [15] to both the horizontal land-sea temperature contrast and the cross-shore sloping MABL. Colle & Novak [16] have also found LLJ in the New York Bight to be associated with a sloping MABL, the differential heating between land and water, as well as the inertia forces and the large-scale weather system. These LLJ cases detected in the NYSERDA dataset may also be linked to these mechanisms. Statistics of LLJ occurrences and characteristics are given in this and the following sections. The analysis is shown only for the North Buoy since results on both buoys are very similar. Histograms of 10-min LLJ observations are shown in Fig. 4 as

monthly and hourly distributions. The bars are plotted against the y-axis as a fraction of the total number of LLJ observations in an entire year. The number at the top of each bar records the LLJ count.

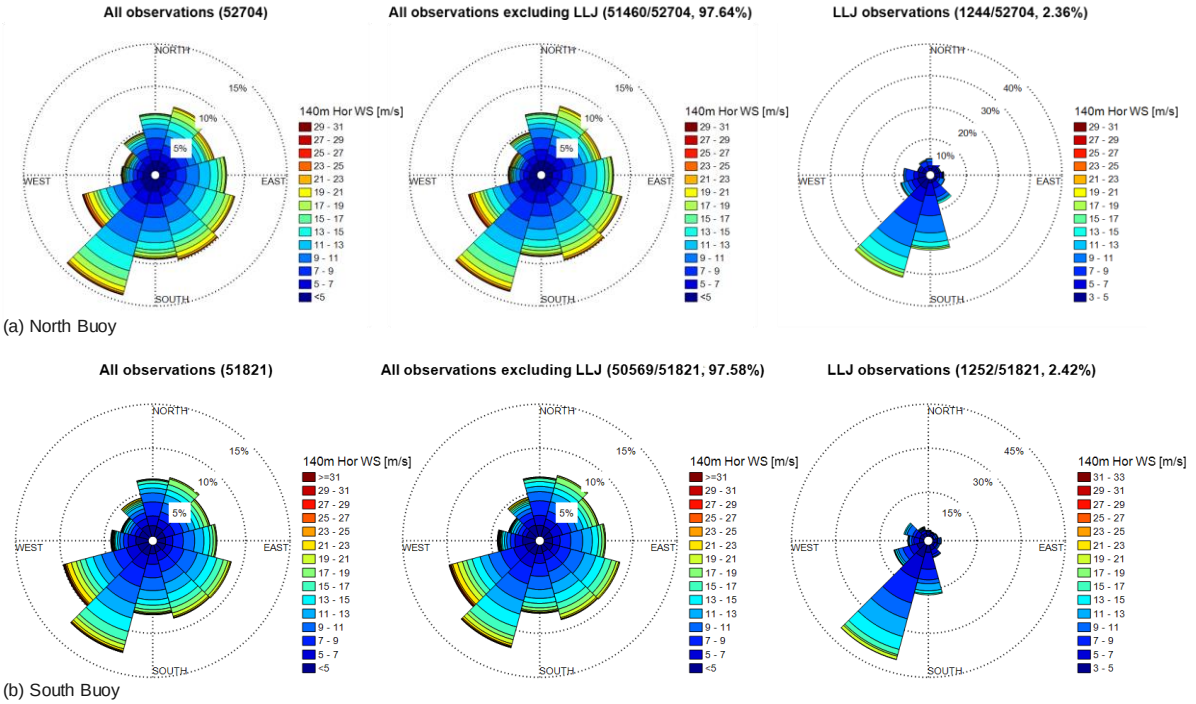

Figure 3: Wind rose for all observations (left), all observations excluding LLJ (middle), and LLJ observations (right) for (a) the North Buoy and (b) the South Buoy at 140 m above MSL.

Figure 4a shows that LLJ are highly concentrated in warm months especially in May, June and July: Of the 1244 10-min LLJ profiles observed in a year, more than 70% occurred in these 3 months. More than one third (438) occurred in the month of June alone; that is more than 10% of the entire 10-min observation pool in June (4320) which nearly quadruples the annual LLJ frequency of 2.4%. This strong seasonal variability of LLJ is consistent with previous findings of LLJ elsewhere in the world. The hourly distribution of jet observations (Figure 4b) shows that LLJ more frequently occur in day-night transition hours from 18 to 00 hour Local Standard Time (LST) which is consistent with what was reported for the onshore Great Plains LLJ (Gutierrez et al. [15]) and the NY Bight LLJ (Colle & Novak [16]).

LLJ cases are usually associated with stably stratified ABL. Stable atmosphere is promoted by less thermal mixing when the sea surface is cooler than the air above. We compute the difference between the air temperature measured at 2 m above MSL and the sea-surface temperature; this distribution is plotted in Figure 5. The histograms are normalized by the total number of all (blue) and LLJ (orange) observations, respectively. A comparison between them shows that the LLJ population is skewed towards stronger

association with a positive differential i.e. cooler sea surface than air, suggestive of a stable MABL giving rise to coastal LLJ. Characteristics of the detected LLJ observations – its jet nose location, wind speed, and wind shear – are statistically analyzed and summarized in the following. The normalized histogram of jet nose height is shown in Figure 6a. Most LLJ cases have a jet nose in the range from 40 to 120 m which falls within the rotor layer of most offshore wind turbines. For the IEA 15MW reference offshore wind turbine considered in this work which has a hub height of 150 m and a rotor diameter of 240 m, the rotor experiences wind from 30 to 270 m above MSL. These LLJ profiles all coincide with the rotor swept face and can directly impact its loading and performance.

Two wind speed magnitudes associated with LLJ – one measured at a reference height of 140 m (close to the turbine hub height) and the other measured at the jet nose – are shown in Figure 6b in comparison with the 140 m wind speed distribution of all the observations. A Weibull distribution is fit to each of these normalized histograms with its scale factor (A) and shape factor (k) displayed in the legend. The results highlight an increase in the average wind speed associated with LLJ in comparison to that of all observations which are dominated by non-jets.

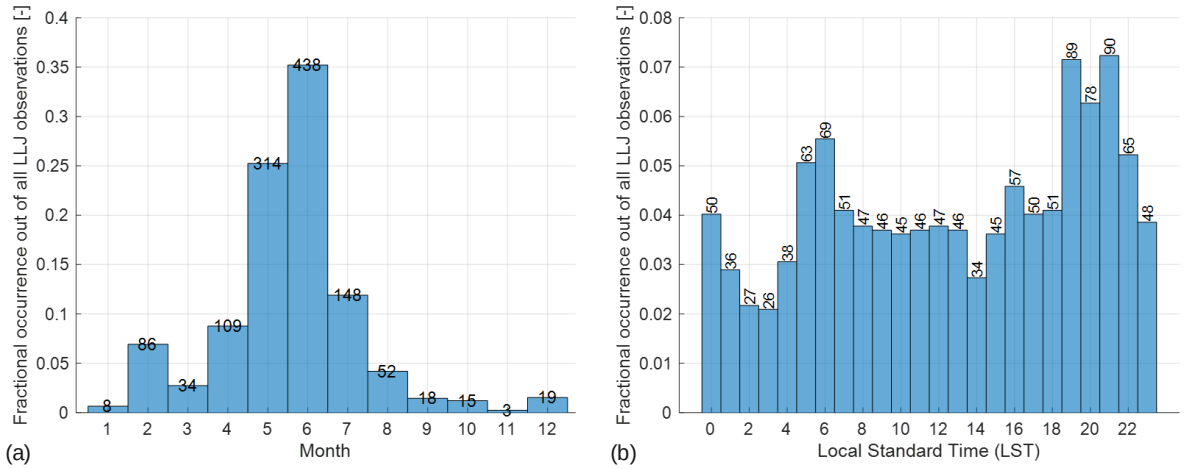

Figure 4: Distribution of LLJ occurrences at the North Buoy: (a) Monthly distribution and (b) hourly distribution.

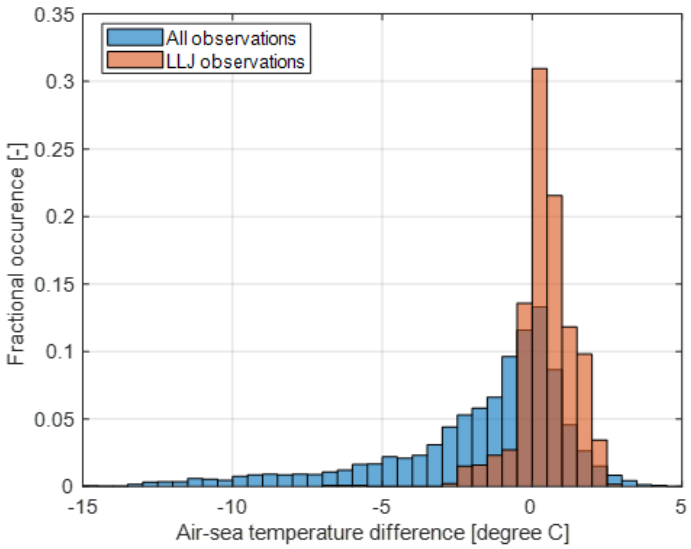

Figure 5: Distribution of measured air-sea temperature difference at the North Buoy: All observations vs. LLJ observations.

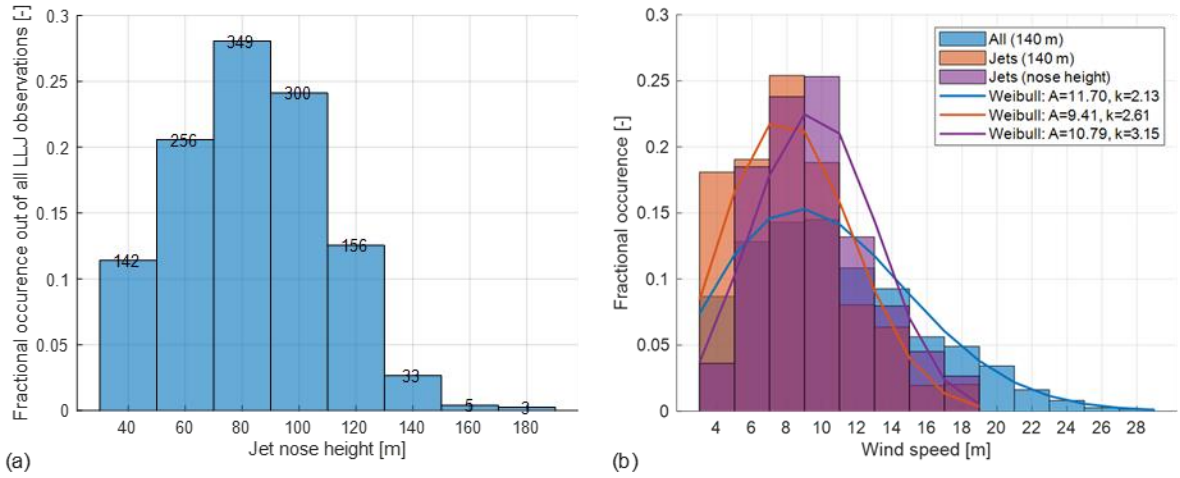

Figure 6: North Buoy measured (a) distribution of the jet nose height and (b) distribution of the wind speed at 140m above MSL for all observations, 140 m for LLJ observations, and the nose location for LLJ observations; The fitted Weibull curves, scale factor, and shape factor are also included.

2.2 Analysis of Weather Forecasting Simulations

To simulate the impact of coastal LLJs on wind energy generation, we first need to demonstrate the capability of mesoscale weather simulations to predict the regional weather and capture LLJ events where the buoys are located. In this project we used the Weather Research and Forecasting (WRF) solver (Skamarock et al. [18]) which is widely used in operational and research numerical weather prediction (NWP). In the following we will describe the WRF model, simulation result, and a comparison between the predictions and measurements.

A WRF model developed by Dr. Mike Optis of NREL was shared with this project team. Its spatial domain is that of Figure 2a centered around the NYSERDA buoys and is suitable for our use. The specification of several key model features is listed in Table 1. These model choices are an outcome of an extensive sensitivity study where the best-performing model configuration was chosen out of 16 model set-ups that vary in input sources, physics parameterizations, and grid and temporal variations (Optis et al. [19]). The model was run over the same time window on which the measured data analysis was performed, i.e. a year from September 2019 to August 2020. The simulation result was also shared with the team. Specifically, the predicted time series at the locations of the buoys were extracted from the WRF result and were interpolated to the lidar measurement heights. A comparison was then made between WRF result and the measured data which will be described below.

Table 1: Specification of key features of the WRF model used in this project.

Feature	Specification
WRF version	4.2.1
Nesting (horizontal grid resolution)	6 km, 2 km
Vertical grid levels	61 vertical cells in total Near-surface levels: 12, 34, 52, 69, 86, 107, 134, 165, 200 m
Output time resolution	5 min
Atmospheric nudging	Nudging performed on the 6-km resolution domain every 6 hours
Planetary Boundary Layer (PBL) scheme	Mellor-Yamada-Nakanishi-Niino (MYNN)
Land-use data source	Moderate Resolution Imaging Spectroradiometer (MODIS) 30 arc-second at 1 km resolution
Global-scale weather data source	ERA5 reanalysis

Comparison between WRF result and measured data

The wind roses predicted by WRF at 140 m above MSL are compared against the measurements in Fig. 7. A decent agreement is found at both buoys; even the nor'easters that occur in winter months were captured in the mesoscale simulation, although WRF noticeably overpredicts the likelihood of wind coming from the southwest direction. A comparison was made in Fig. 8 on the annual-averaged wind speed profile to assess the overall model skill in predicting offshore wind resource. The mean wind speed interpolated at 150 m above MSL, hub height of the IEA-15MW reference offshore wind turbine, is given. The mean power-law shear exponent of the entire profile is also computed by using wind speed values at 20 and 200 m. WRF underestimates both wind speed and wind shear for heights above 40 m while the rotor layer is in the range of 30 to 270 m. This level of agreement is similar to what was reported by Optis et al. [19] using the same model, and highlights a conclusion made in a 2018 study by Banta et al. [20] that "the rotor-layer wind speed errors in NWP were larger than required for siting decisions for offshore wind farms".

We also made a direct comparison between the modeled and measured time series. An example is given in Figure 9 for May 2020 at the South buoy in which many LLJ occurrences were found. The level of agreement is good. One can observe very weak signature of diurnal cycle in the air-sea temperature difference in both the modeled and measured results, an important characteristic of the MABL that differs from the land ABL. It is also found that LLJ occurrences are usually associated with positive air-to-sea temperature differential, i.e. when the sea surface temperature is lower than that of the air. This is captured both in measurements and in WRF and agrees well with previous findings that surface cooling discourages turbulent mixing and promotes a stable MABL which gives rise to stronger shear and potential development of LLJ.

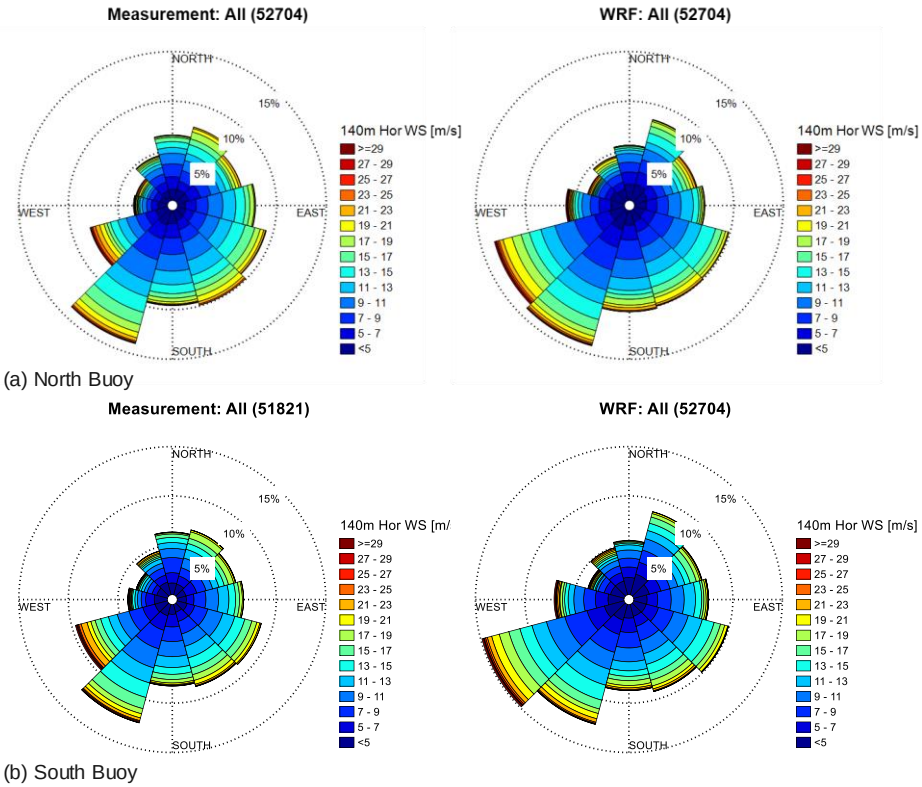

Figure 7: Measured vs. modeled wind rose evaluated at 140 m above MSL for (a) the North Buoy and (b) the South Buoy.

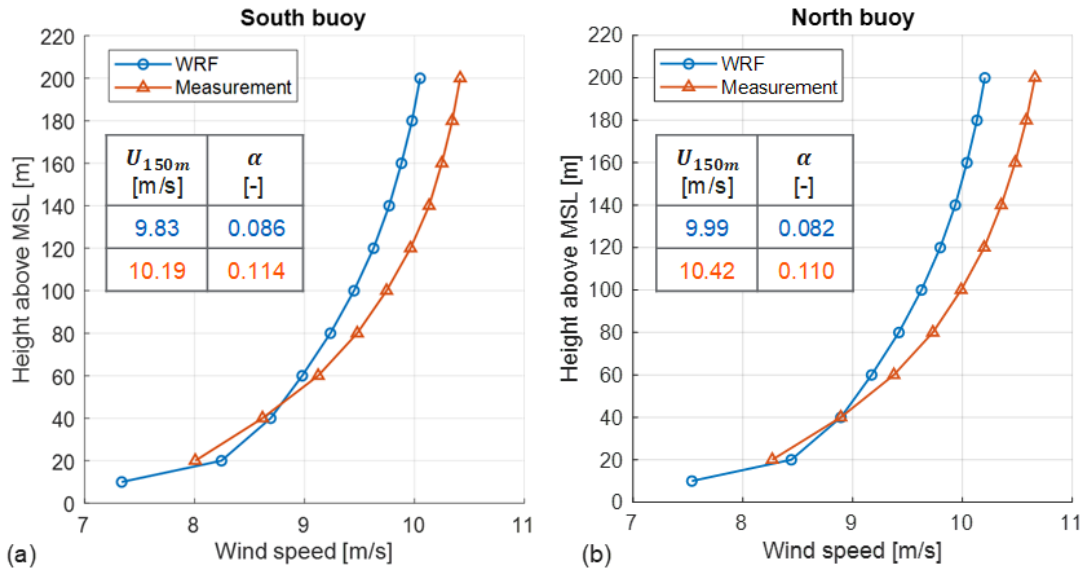

Figure 8: Annual-averaged wind speed profile at (a) South and (b) North Buoys as a comparison between WRF prediction and measured data. Mean hub-height wind speed and power-law shear exponent are given.

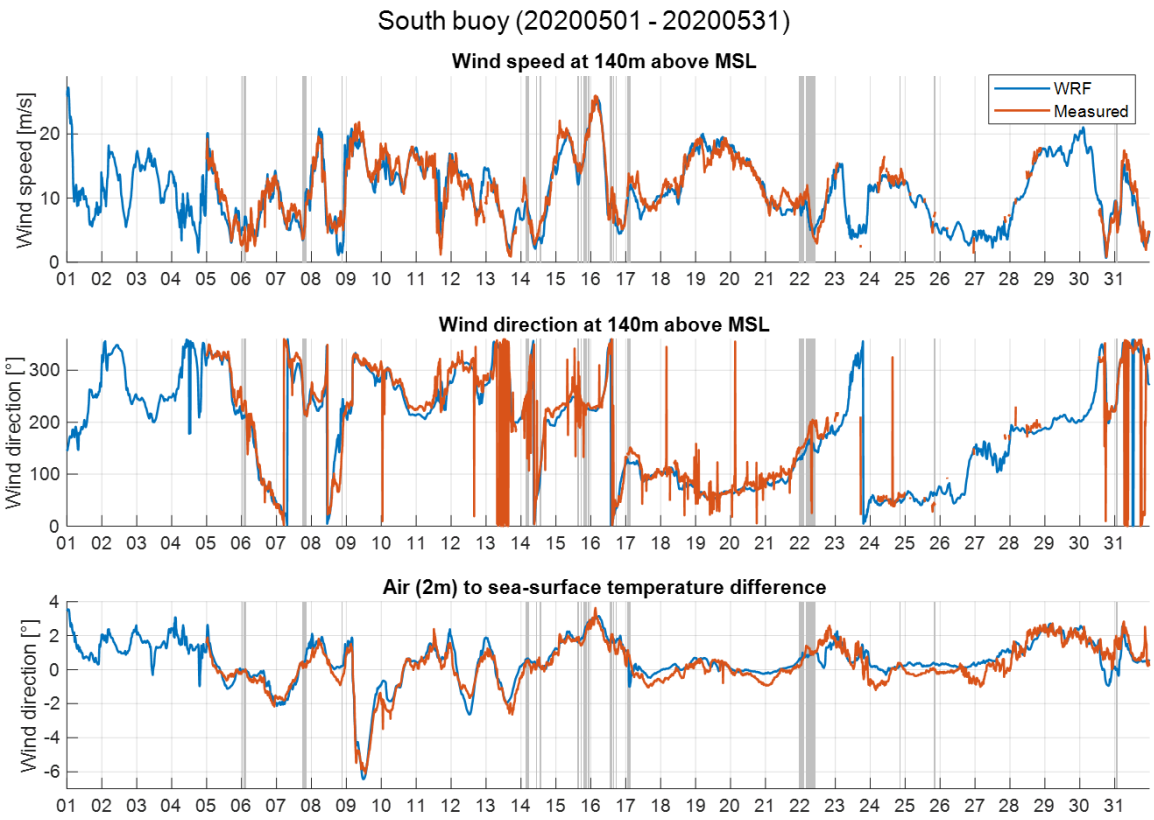

Figure 9: Time series over May 2020 at the South Buoy as a comparison between WRF prediction and measured data: Wind speed (top) and wind direction (middle) at 140m above MSL, and the air to sea-surface temperature difference. The abscissa is days within the month. The shaded grey areas correspond to the detected LLJ observations in the measurements.

10-min LLJ observation predictions

In the following a comparison is made on the averaged LLJ profiles. Figure 10 all 10-min LLJ profiles are averaged and displayed. A good agreement is found. The model performs better at the North Buoy, which may be explained by its longer distance to the coastline and thus less affected by the complex coastal atmospheric processes that are particularly challenging to model. The average jet nose is measured at 80 m and is accurately captured by WRF. An under-prediction of rotor-layer wind speed, similar to what was shown in Fig. 8, is present here. Three power-law shear exponents are computed: one for the entire profile based on wind speeds at 20 and 200 m, one for the upper half of the profile at 80 and 200 m, and the other for the lower half at 20 and 80 m. WRF strongly under-predicts the positive wind shear in the bottom half and slightly over-predicts the negative shear in the top half.

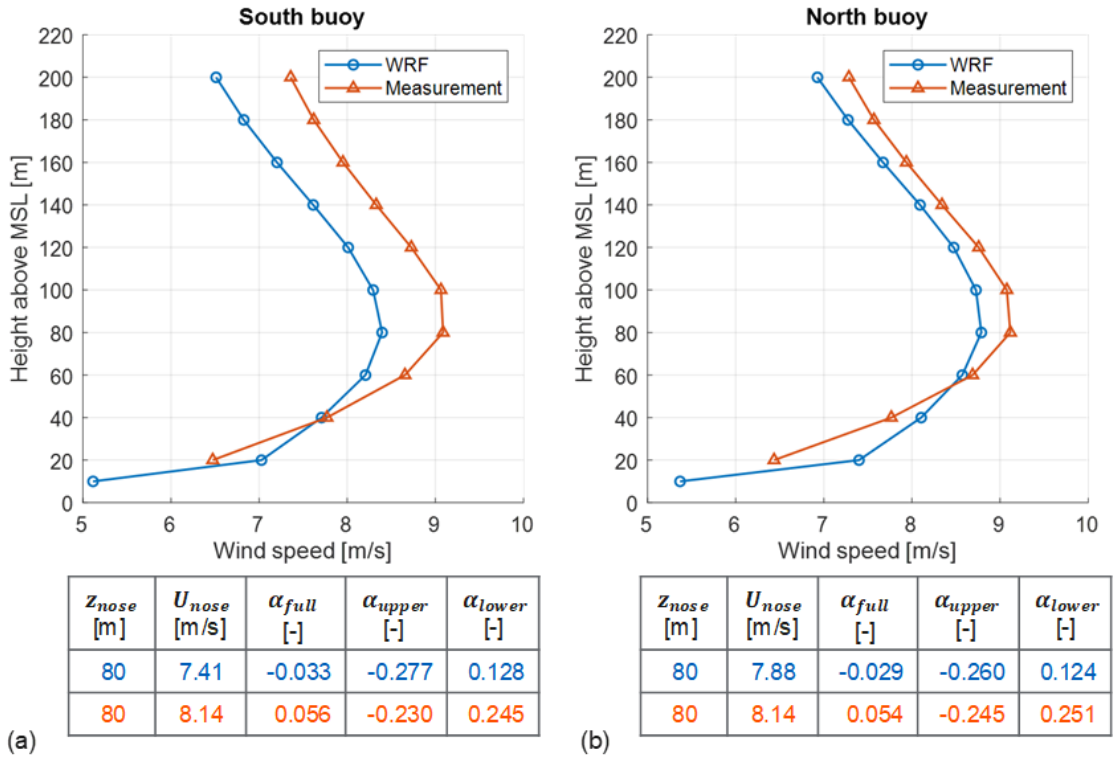

z_{nose} [m]	U_{nose} [m/s]	α_{full} [-]	α_{upper} [-]	α_{lower} [-]
80	7.41	-0.033	-0.277	0.128
80	8.14	0.056	-0.230	0.245

z_{nose} [m]	U_{nose} [m/s]	α_{full} [-]	α_{upper} [-]	α_{lower} [-]
80	7.88	-0.029	-0.260	0.124
80	8.14	0.054	-0.245	0.251

Figure 10: Annual-averaged wind speed profile for LLJ observations at (a) South and (b) North Buoys as a comparison between WRF prediction and measured data. Mean jet nose location, jet nose wind speed, power-law shear exponent for the entire profile ($\boldsymbol{\alpha_{full}}$), upper half of the profile above the jet nose ($\boldsymbol{\alpha_{upper}}$), and lower half of the profile below the jet nose ($\boldsymbol{\alpha_{lower}}$) are given.

Persistent LLJ event predictions

Two specific LLJ events are used as examples to further compare the simulated and measured results for the South Buoy. Figure 11a shows the time window from May 14th to 16th while Fig. 11b shows May 21st to 22nd. The WRF result is in excellent agreement with the measurement in the first example as can be seen from the time-height wind speed contours in terms of the wind speed, jet nose location, jet intensity and its evolution over time. A comparison on several 10-min average wind speed profiles is also given and an excellent agreement is found especially in the latter portion of the event.

The second example in Figure 11b shows a shallower LLJ at lower wind speed. Although not shown here, the wind blows from open sea at an average wind direction of 150° in this case, while the wind is roughly parallel to shore at 233° in the first example. Although WRF can predict LLJ, the quantitative agreement is poorer with a significant under-prediction of wind speed and the jet intensity. There also appears to be an offset in time which may be due to an inaccuracy in the ERA5 global-scale boundary condition as report

by Tay et al. [21]. Although not shown here, additional comparisons were made on other LLJ events; a few were completely missed by WRF. This highlights that the capability of the WRF model to predict LLJ varies from case to case, which may indicate that differing LLJ mechanisms are at play for which the WRF model skills vary.

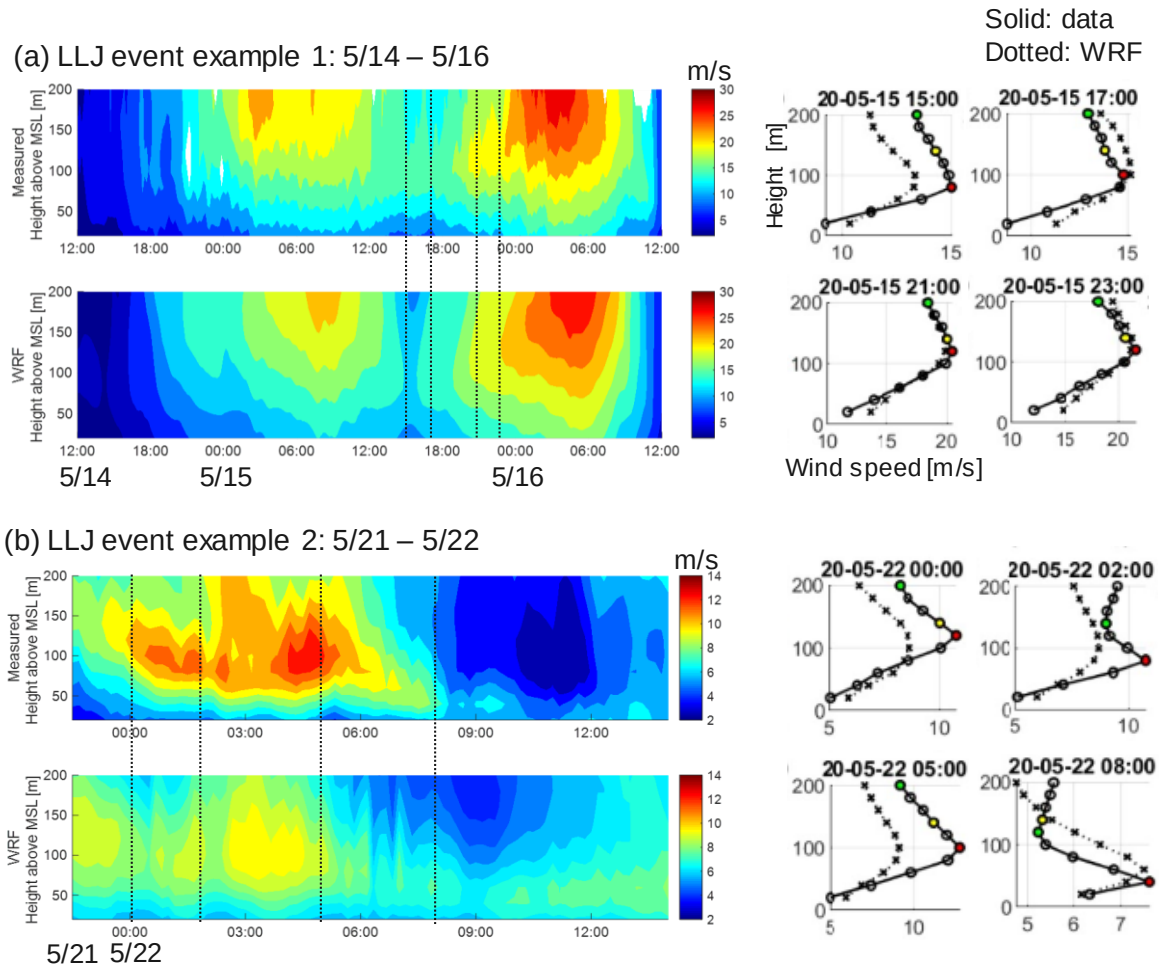

Figure 11: Two examples of LLJ events detected at the South Buoy. Left: Time-height contour plots of wind speed, shown as a comparison between measurements (top) and WRF prediction (bottom). Right: Wind speed profiles of four 10-min averaged time instances that correspond to the four black dotted lines on the left figures. The solid line is the measured data. The dotted line is the WRF prediction.

2.3 Meso-micro Coupling and LES of Low-level Jets Turbulence

Mesoscale-to-microscale coupling (MMC) is an active area of research that has become increasingly important for both the meteorology and wind energy communities, and aims to bridge modeling gaps that have long existed in atmospheric flow and wind farm flow simulations [22]. It is one of the key innovation

thrusts of this project to demonstrate MMC in modeling coastal LLJ. In this section, we briefly review coupling techniques that were considered in this project.

As illustrated at the top of Figure 12, the current modeling approach of high-fidelity microscale LES simulation is based on *stationary forcing*, e.g., through the specification of a constant geostrophic wind speed and surface heat flux over time and space, and is therefore largely *decoupled* from realistic mesoscale processes like diurnal cycles, frontal events, and terrain effects, etc. that determine microscale atmospheric flow conditions. Therefore, this decoupled approach relies on the use of periodic lateral boundary conditions (LBC) and is limited to the representation of simple, idealized atmospheric flow with horizontal homogeneity, and makes an accurate characterization of microscale LLJ features not possible.

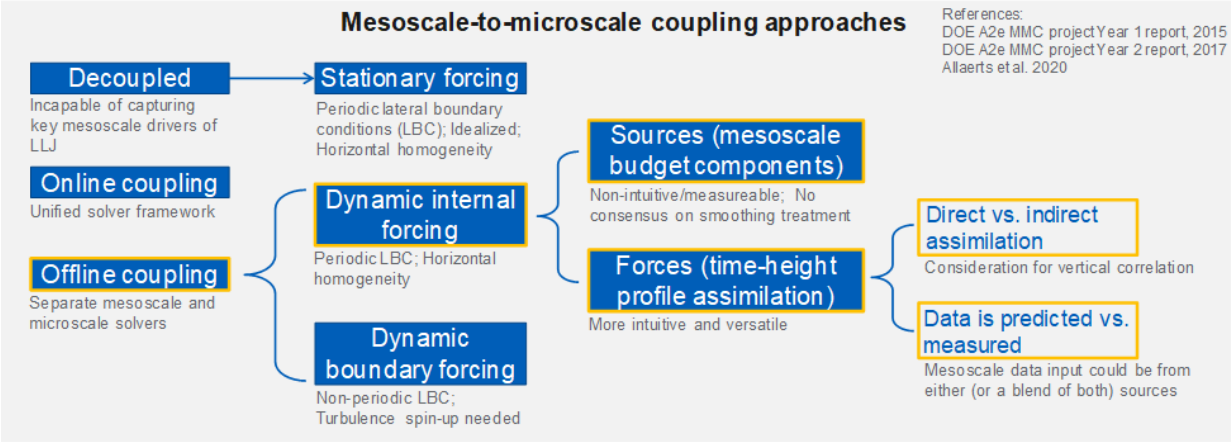

Figure 12: Decoupled vs. mesoscale-and-microscale-coupled techniques. Highlighted boxes are the approaches that will be considered in this project.

To overcome this limitation, this project expanded the microscale wind modeling capabilities by applying MMC techniques and demonstrating it on the characterization of LLJ. There are several considerations for making MMC modeling choices:

1) **Communication directionality:** The cross-scale information transfer may be one-way where the mesoscale parameters are downscaled to provide forcing for the microscale domain, or two-way where a backward upscaling also occurs [23]. The former has received the most attention in recent MMC research and is thus also used in this project.

2) **Communication strategy:** The coupling may be achieved "online" or "offline": The online approach usually means the use of a unified solver framework with scale-appropriate physics available for both scales and solved concurrently. The offline approach, on the other hand, permits

greater flexibility and allows mesoscale and microscale processes to be simulated separately with solvers tailored for their respective regimes of interest. The latter approach is adopted in this project.

3) **Information transferred:** As discussed in Allaerts et al. [24], the exact mesoscale information that is to be downscaled and transferred may be components that directly make up the mesoscale momentum and temperature transport equations budgets, i.e., large-scale driving horizontal pressure gradient, momentum advection, and temperature advection. Alternatively, this information may be generated by data assimilation based on either i) mesoscale profiles of wind and temperature; or ii) measurable meteorological quantities, e.g., wind speed, temperature, pressure, momentum and heat fluxes, and moisture. While the former approach relies on a mesoscale solver to output those budget terms, the latter approach permits the use of either solver or observational data. We tested both approaches in the present study.

4) **Location of information transfer:** The coupling may be applied at domain boundaries such as the inflow and surface planes, or act upon the entire flow volume. The former, *dynamic boundary forcing* method permits the use of non-periodic LBC at the expense of extra computational overhead of either long upwind stretch or added turbulence spin-up treatment to accelerate the generation of microscale turbulent structures. The latter, *dynamic internal forcing* method doesn't require such added cost, but it still relies on a periodic LBC under the assumption of horizontal homogeneity that somewhat limits the range of atmospheric processes that may be simulated, e.g. complex terrain [25]. The assumption used in the latter approach is considered valid for LLJ events that are reasonably distant from the coastline where the horizontal heterogeneity is weak and the LLJ can be described as a planar jet; therefore, the dynamic internal forcing technique is chosen for this project.

In summary, this project achieved MMC through one-way, offline coupling via dynamic internal forcing. The specification of mesoscale parameters both in the form of direct mesoscale budget components (from WRF results) and in the form of data-assimilated time-height profiles (from either WRF results, or measured data, or a blend of both) were all fully explored in this work.

For the mesoscale-forced microscale simulations, we have selected a computationally efficient MMC strategy that utilizes a horizontally homogeneous domain forced by WRF. Stable conditions with westerly winds can develop land-sea breezes and form an internal boundary layer emanating from the coastline, which can both propagate far offshore. Our assumption of homogeneity is based on the spatial scales of resolved coastal features being on the order of the microscale domain or larger; all large-scale heterogeneity is represented as uniform variation over time in the flow quantities in the microscale.

Figure 13 illustrates mesoscale flow quantities of interest around the lidar buoys deployed by NYSERDA, extracted from a subset of the inner WRF domain during our case study. Large-scale horizontal gradients in the winds can be seen, along with non-uniform sea-surface temperature (SST) distribution likely driven by upwelling. However, for the purposes of forcing the microscale, the mesoscale-simulated surface-layer properties including the sensible heat flux and friction velocity are relatively uniform throughout the region of interest spanning the two buoys. Similarly, the turbulence kinetic energy (TKE) aloft at approximately 143 m above MSL—near the hub height of the IEA 15-MW reference turbine, the planned subject of future study—is also approximately uniform in the region of interest. The time-averaged standard deviations of values within a 2760 km^2 region spanned by the two buoys are 1.1 m/s and 2.3° for wind speed and direction; 6.9e-3 m^2/s^2 for TKE; 1.8e-2 m/s for friction velocity; 0.3 K for SST; and 2.4 W/m^2 for heat flux.

To validate the MMC approach we selected a 12-hr simulation window in the last 12 hours of May 15th, 2020 (UTC) in which an LLJ event was observed and was well predicted by the WRF mesoscale simulation (Figure 11 a). We chose to focus on the South Buoy since the root-mean-square error (RMSE) of hub-height wind speed is slightly lower than the North Buoy over the entire 12-hr window. In the following, we first describe the LES model configuration. Thereafter we introduce several variant configurations which the team built to investigate how the simulation outcomes would change when different MMC profile assimilation strategies were used. Both qualitative and quantitative comparisons of results and detailed discussions are included in this final report.

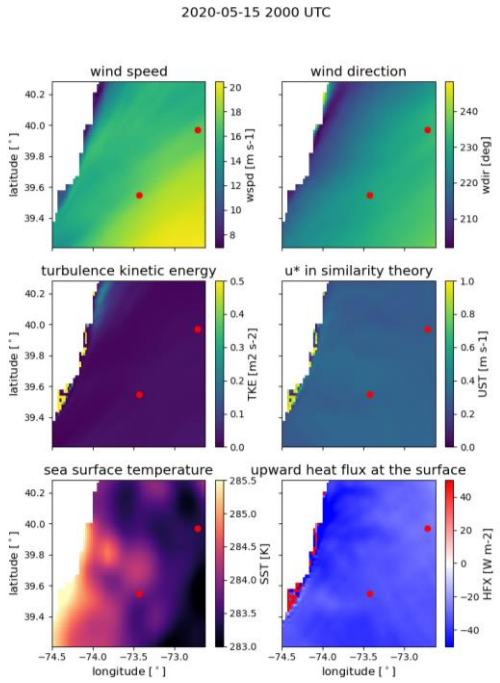

Figure 13: Comparison of quantities of interest in a subset of the WRF inner nested domain with 2-km grid spacing; wind speed, wind direction, and turbulence kinetic energy have been sampled at approximately 143 m above mean sea level; the red dots indicate locations of the NYSERDA buoys.

As mentioned previously, we used NREL's AMR LES solver, part of the exawind tool suite, to simulate the microscale atmospheric flow. All simulations were performed on a 5120 m by 5120m doubly periodic domain (in the horizontal directions); the domain height was 1280 m. A uniform grid spacing of 10 m was used in all cases. Whereas such spatial resolution is adequate for neutral and convective conditions, it presents a lower resolution bound for simulations of a stable boundary layer. WRF provides the initial conditions, surface boundary conditions, and internal forcing. Since the entire microscale LES domain lies within the WRF inner domain, both the initial conditions and the assimilated planar-average profiles for velocity and temperature are completely specified for the duration of the simulation. A surface heat flux, which in this case provides cooling, is specified at the lower boundary from the WRF surface solution. Wall modeling is provided through a Meong surface shear-stress boundary condition. The upper temperature boundary has a fixed vertical gradient, based on an adiabatic lapse rate of 1 K/km. Lastly, subgrid-scale turbulence closure is provided by the one-equation Deardorff eddy viscosity model.

Two approaches of internal MMC were considered with three different treatments of the mesoscale temperature profiles. The two approaches considered are direct and indirect profile assimilation (DPA and IPA, respectively)—the former guarantees that the microscale planar-average profiles exactly match the specified WRF profiles whereas the latter aims to provide more realistic momentum and virtual potential

temperature source terms by not requiring the mean profiles to exactly follow the mesoscale solution. In our studies performed in this project, we used DPA for velocity and used a few variations of IPA on the potential temperature solution. Allaerts et al. [24] observed that WRF temperature profiles may be unrealistic and lead to excessive buoyancy production in a resolved microscale daytime ABL; the converse may also be true, that an incorrect WRF profile can also lead to excessive buoyancy consumption and suppress turbulence. In all cases, the full WRF temperature profile was used to initialize the SOWFA simulation. However, we consider three model variations in which (1) the full temperature profile is assimilated over time; (2) the temperature is assimilated at a single level only, which in this case we have chosen to be the observed 2-m virtual potential temperature; and (3) no temperature assimilation is performed, i.e., no temperature source terms are included.

The Mesoscale to Microscale Coupling (MMC) project team under the U.S. Department of Energy's (DOE's) Atmosphere to Electrons (A2e) program published verification and validation metrics to assess models' abilities to reproduce observed variables and turbulence structures (Haupt et al. [23]). Based on the data availability in observations, mesoscale model outputs, and microscale model outputs, we selected a subset of variables in Table 2, recommended in Haupt et al. [23].

Table 2: Variables and metrics from comparing among observations, mesoscale model predictions, and microscale model predictions.

Variable group	Variable	Averaging period	Basic metrics
Lidar measurements (at all heights)	Mean wind speed	10 min	Root mean square error (RMSE), mean absolute error (MAE)
	Wind speed standard deviation and turbulence intensity[1]	10 min	RMSE, MAE (or qualitative comparison)
	Mean wind direction	10 min	RMSE, MAE
Lidar measurement near hub height	Hub height mean wind speed	10 min	RMSE, MAE
	Hub height wind speed standard deviation and turbulence intensity[1]	10 min	RMSE, MAE (or qualitative comparison)
	Hub height mean wind direction	10 min	RMSE, MAE
Near-surface meteorological measurements at 2m above MSL	Mean wind speed	10 min	RMSE, MAE
	Min/max wind speed	10 min	MAE
	Mean air temperature	10 min	RMSE, MAE
Processed quantities	Jet nose location	10 min	MAE
	Jet top location	10 min	MAE

Wind shear across rotor (30-270m) and split between the jet nose location[2]	10 min	MAE
Wind veer across rotor (30-270m)	10 min	MAE

Table 3: Mean absolute error for quantities of interest, calculated from mesoscale-forced microscale simulations in comparison lidar measurements. Indirect and direct profile assimilation (IPA and DPA, respectively) techniques were applied with WRF mesoscale wind and temperature data; while the time-varying wind profile was assimilated in all cases, the temperature assimilation was treated in three different ways: time-varying profile, time history at 2 m above mean sea level, and without any temperature assimilation. Rows are shaded with green-white-red representing the 0-50-100th percentiles.

	IPA, T profile	DPA, T profile	IPA, 2-m T only	DPA, 2-m T only	IPA, no T assim.	DPA, no T assim.
hub-height wind speed [m/s]	1.000664	0.758987	0.954844	0.787399	0.940654	0.842972
hub-height wind direction [°]	9.91527	10.424833	10.343671	10.522423	10.357223	10.366576
resolved+SGS TI [-]						
‣ *rotor bottom (z=30)*	0.007242	0.027776	0.00769	0.125668	0.007068	0.125157
‣ *hub height (z=150)*	0.035653	0.047628	0.036794	0.026835	0.037612	0.027352
‣ *lidar max range (z=200)*	0.046447	0.04933	0.047988	0.0207	0.048183	0.021083
resolved+SGS wind stddev [m/s]						
‣ *rotor bottom (z=30)*	0.20474	0.167447	0.204868	1.882391	0.195875	1.906215
‣ *hub height (z=150)*	0.263044	0.483812	0.274365	0.814135	0.289241	0.822981
‣ *lidar max range (z=200)*	0.357886	0.429631	0.383414	0.691338	0.387759	0.697921
jet characteristics						
‣ nose height [m/s]	34.387755	15.816327	40.714286	16.22449	41.122449	16.836735
‣ max speed [m/s]	0.6698	0.595127	0.643465	0.686214	0.635776	0.737451
‣ shear below nose [-]	0.076716	0.116082	0.096481	0.114695	0.097423	0.119638

The mean absolute errors (MAEs) and root-mean-square errors (RMSEs) of variables defined in Table 2 are summarized in Table 3 and Table 4, respectively, for several MMC variants. Rows are shaded with dark green, white, and red corresponding to the 0^{th} (lowest error), 50^{th}, and 100^{th} (highest error) percentiles, respectively; wind direction errors were excluded from shading because errors were relatively low in all cases. Interestingly, model configurations that perform relatively well in terms of turbulence are poor performers in the mean jet characteristics—namely, the IPA results; conversely, the best performer in the mean jet characteristics is the worst performer in resolved turbulence—i.e., DPA with temperature profile assimilation. The mixed results for DPA with single-level or without temperature assimilation motivate other quantitative assessments of the resulting flow fields.

Table 4: Root-mean-square error for quantities of interest, calculated from mesoscale-forced microscale simulations with SOWFA in comparison lidar measurements. Indirect and direct profile assimilation (IPA and

DPA, respectively) techniques were applied with WRF mesoscale wind and temperature data; while a time-varying wind profile was assimilated in all cases, the temperature assimilation was treated in three different ways: time-varying profile, time history at 2 m above mean sea level, and without any temperature assimilation. Rows are shaded with green-white-red representing the 0-50-100th percentiles.

	IPA, T profile	DPA, T profile	IPA, 2-m T only	DPA, 2-m T only	IPA, no T assim.	DPA, no T assim.
hub-height wind speed [m/s]	1.201767	0.887142	1.149304	0.904983	1.135609	0.976524
hub-height wind direction [°]	19.052457	19.163245	19.129077	19.104568	19.136675	19.266376
resolved+SGS TI [-]						
‣ *rotor bottom (z=30)*	0.009043	0.029578	0.009395	0.127484	0.009098	0.127129
‣ *hub height (z=150)*	0.036574	0.048132	0.037624	0.030693	0.03837	0.032347
‣ *lidar max range (z=200)*	0.047047	0.050183	0.048532	0.025973	0.048783	0.027149
resolved+SGS wind stddev [m/s]						
‣ *rotor bottom (z=30)*	0.234353	0.198689	0.230664	1.903159	0.225059	1.93565
‣ *hub height (z=150)*	0.294888	0.506178	0.310348	0.85844	0.323364	0.880284
‣ *lidar max range (z=200)*	0.389409	0.46016	0.411935	0.718173	0.41896	0.74496
jet characteristics						
‣ nose height [m/s]	36.540444	19.704449	43.195096	20.615528	43.242317	20.714286
‣ max speed [m/s]	0.800905	0.716102	0.777661	0.824602	0.763682	0.943068
‣ shear below nose [-]	0.081782	0.123003	0.101281	0.125094	0.102167	0.12674

Overall, the team found that applying DPA to calculate the exact forcing to attain the mesoscale mean wind profiles, while applying IPA to calculate the approximate forcing that allows the microscale temperature profile to evolve from the mesoscale input. This approach generated more accurate mean wind profiles combined with more realistic temperature profiles and resolved turbulence.

3 Windfarm Modeling Advances in Exawind

Several areas of AMR-Wind development were needed to achieve all the goals and milestones of this project. In the following we will briefly describe these AMR-Wind development efforts:

1) Internal mesoscale forcing with Profile Assimilation: This was required to achieve MMC and to simulate LLJ in the microscale domain driven by the mesoscale forcing from the Weather Research and Forecasting (WRF) model. We implemented in AMR-Wind both a direct and an indirect profile assimilation technique. All these capabilities were verified and validated on both CPU and GPU architectures. The same set of simulations corresponding to the NYSERDA buoys that were described in the previous section were simulated with AMR-Wind. Additionally, some effort was put in to understand how the choice of controller gain and the LES subgrid turbulence model impacts the solution.

2) Modification of the Boussinesq approximation: In the simulations with turbines, a critical element to ensure stability of the simulations is the appropriate outflow boundary conditions to ensure the highly non-homogeneous flow exits the domain without generating any spurious oscillations. In this study we developed a strategy where the mean pressure gradient on the outflow face is balanced by the buoyancy term in the Boussinesq approximation. The project team developed several best practices associated with running simulations with inflow-outflow boundary conditions with inflow BC information generated from a separate precursor simulation.

3) During the course of this study, team found a significant slowdown when writing ABL boundary data, in netcdf file format, with parallel processors. Motivated by the need of this project the Exawind team implemented the boundary data output in the native AMReX file format. This new development significantly reduces the computational time and allows for boundary data file output for longer simulations (> 30 minutes). Additionally, this project team also developed a python-based tool to stitch several boundary data files output from a series of simulations into a single long boundary file.

4) The project team worked with the Exawind and ROSCO development teams to develop restart capabilities for AMR-Wind coupled with OpenFast simulations. This involved outputting and reading all the OpenFast relevant information from AMR-Wind. Additionally, ROSCO controller needs several inputs every time a restart is performed. ROSCO development team implemented

additional routines in ROSCO source to allow for frequent restarts. Both capabilities have now been merged in the respective master versions and is being frequently used by a number of users.

4 Impact of Low-level Jets on Windfarms

4.1 Analysis of LES Data

The current section discusses in detail the impact of flow fields in the coastal-low level jets on the pad level loads of the wind turbines in a 5 X 4 farm layout. The results have been further compared against monotonically sheared convectively unstable boundary layer representative of onshore conditions. Figure 14 illustrates the high-level schematic for the framework for running high-fidelity LES simulations (*"virtual wind farm"*) for wind farms using ExaWind Suite developed by NREL. The Weather Research and Forecasting Model (WRF) simulates the weather condition that pertains to coastal low-level jets at mesoscales in the range of ~ 50 km. The mean wind and temperature conditions of the coastal LLJ are used to drive microscale LES simulations of the atmospheric boundary layer (ABL) precursor (~ 10 m resolution) with proportional controller based data assimilation of mean conditions. The precursor miscroscale-LES data are used to drive wind farm simulations. The farm domain is similar to the precursor ABL domain except that it contains two layers of nesting of mesh around the wind farm with resolutions as low as 2.5 m (~ 10 grid points/rotor diameter D). Aeroelastic solver OpenFAST are coupled at each pad-level locations for computation of the loads with turbine controllers. Figure 15 illustrates the zoomed in view of the wind farm domain with labels for each pad locations for 5 X 4 = 20 turbines, with the turbine ID increasing contiguously in the cross-wind direction. Note, a similar analysis has been carried out in 5 X 1 layout arrangement but is not reported in the final project report for brevity. In the subsequent part of the discussion, we discuss the flow-field characteristics of coastal LLJ and convectively unstable MS and how those correlate with system-level loads providing unique insights to not only the load characterization of the farm but a fundamental framework for load mitigation strategy. In particular, Figure 16 manifests the instantaneous snapshot of planform view of velocity field past the wind farm for LLJ and MS cases. We observe, LLJ is characterized by deep wakes, lack of wake meandering and small scale turbulence. MS contains rather more coherent turbulent eddies, shallow wakes owing strong mixing coupled with prominent wake meandering dynamics. This is further corroborated by more robust features metricized through time-averaged & rotor-averaged data in Figure 17. Please, note that for results involving rotor-averaged data obtained directly from amr-wind, we have in practice established, rather a surrogate rotor-averaged quantity defined by $\int_{z=z_h-D/2}^{z=z_h+D/2} <> \, dz$ replacing $\oint <> \, dA$ (true-rotor average). The surrogate rotor-average ensures that temporal volume data need not be stored, and 4 sets of planar data should be sufficient to perform the operation. Extensive verification and validation study has been done for both LLJ and MS (not shown in the report for brevity) to justify that the surrogate rotor-average or the z-line average model can capture the mean and the temporal characteristics of the true rotor-average. In particular, U_{AD}, TI_{AD} can be written as

$$U_{AD} =< \int_{x=-2.5D}^{x=0} \int_{z=z_h-D/2}^{z=z_h+D/2} \tilde{u}(x,y,z,t)dxdz >_T$$

$$TI_{AD} = \sqrt{< \int_{x=-2.5D}^{x=0} \int_{z=z_h-D/2}^{z=z_h+D/2} \left(\tilde{u}(x,y,z,t) - \overline{\tilde{u}(x,y,z)}\right)^2 >_T} / U_{AD}$$

The rotor quantities are a perfect gateway to understand how the turbine disk influences the flow-field around itself. In particular, we observe, that the LLJ manifest stronger wake deficit and stronger induction compared to the MS cases followed by stronger suppression of pad level turbulence which results in deep persistent wakes in the downstream turbines. Additionally, the mean streamwise variation (U_{AD}, TI_{AD}) illustrates high variability across the different column of wind turbines in wake region for the MS cases indicating strong meandering due to thermal plumes. Contrary to that, the LLJ wakes are stably stratified and show significantly less variability across the different columns of turbines which speaks of strong wake persistence. In order to understand, how these flow-field quantities, especially at the pad level locations correlate with the load characteristics, we "*extract*" the flow-field information at the pad location with a the level of information filter for the loads and a phase-aligned spatial average ($x \in -2.5D, 0$) where $x = 0$ denotes the pad location which also works like a low-pass filter owing to frozen Taylor's field upstream of the turbine location. The low-pass filtering ensures that the temporal characteristics are devoid of frequencies at or greater than 1P and the load vs flow-field correlation calculated is entirely turbulence driven without any structural interception. Figure 18 & Figure 19 illustrates the reconstructed flow-fields calculated at each pad location, in particular the rotor-averaged velocity, TI and the metrics of shear, veer which play a critical role in deciding the rotor blade and shaft loads. Figure 18 demonstrates the time-averaged "reconstructed" rotor-averaged velocity (obtained from phase-aligned averaging) at different pad locations both for the LLJ and the MS case that have been compared against the standard rotor-averaged velocity obtained from OpenFAST. The comparison serves as a verification procedure giving entitlement of a similar trend of reconstructed flow-field vs OpenFAST at different pad locations for both LLJ and MS cases. Figure 19 illustrates the vertical gradient of the dominant wind direction & cross-wind direction $\tilde{u}, \tilde{v}$ where the ~tilde denotes the scale-resolved quantity pertaining to LES simulations. In the subsequent discussion, the tilde is dropped for brevity. du/dz is the shear component while dv/dz is veer associated with the flow. In the 1st row of "reconstructed" shear flow-field, since the data is rotor-averaged the negative and positive shear cancels out giving rise to very low rotor-averaged shear for LLJ. Contrary to that, MS cases have higher positive rotor-averaged shear. As wakes propagate downstream of the turbines, the shear gets stronger in the LLJ case compared to the MS case, and consequently the rotor-averaged shear in the downstream turbines are comparable in the LLJ and MS cases. Strong veer dv/dz are observed in the LLJ

case which are characterized by a short inversion layer and stable stratification. The veer component is significantly lower in the MS cases, and since the height of the inversion layer does not change in LLJ, the strength of the veer component is quasi-preserved in the downstream turbines as well. This section prepares the ground in terms of creating a bucket list of flow-field metrics for the correlation analysis with the loads that will be carried out later.

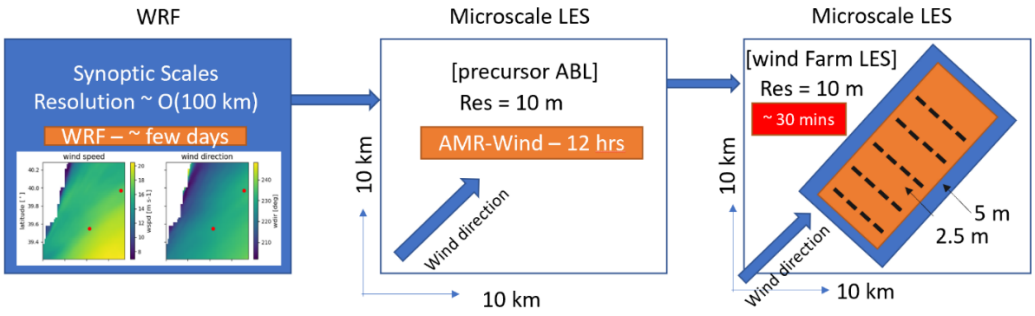

Figure 14: Schematic of WRF driven LES. Left to Right: WRF simulations in mesoscale grid (resol:~ 100 km). WRF forcing drive the precursor microscale ABL LES (resol: 10 m). Precursor ABL body forcing term drive the 2-level nested wind farm LES (max resol: 10 m, min resol: 2.5 m).

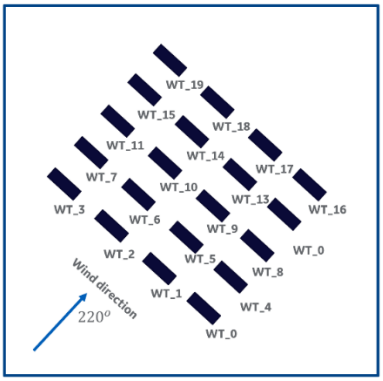

Figure 15: Zoomed schematic wind farm domain with 20WT layout in a 5 X 4 arrangment. 5 rows aligned with wind are R0, R1, R2, R3 & R4. 4 columns are cross wind C0, C1, C2, C3.

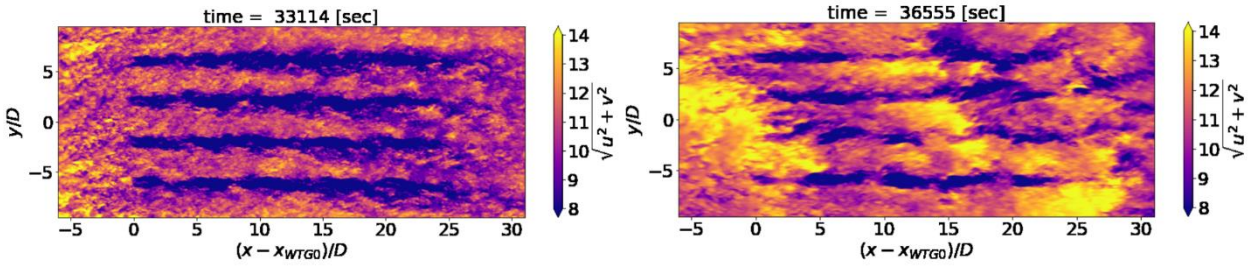

(a) (b)

Figure 16: Instantaneous snapshot of xy plane / planform view of wind farm simulations. (a) LLJ (b) monotonically sheared unstable configuration (MS). Timestamp t = 17 min.

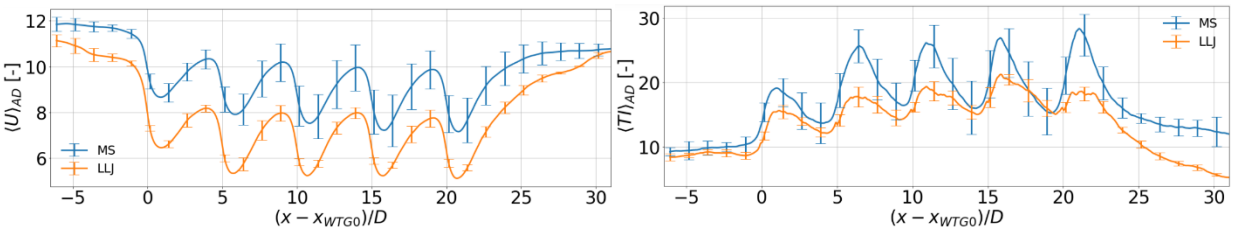

(a) (b)

Figure 17: Streamwise variation of time-averaged & column averaged rotor flow-field quantities. (a) rotor-averaged velocity (b) rotor-averaged TI [%]. Error-bars denote variation across columns C1, …, C4. x_{WTG0} is the location of the first row of turbines.

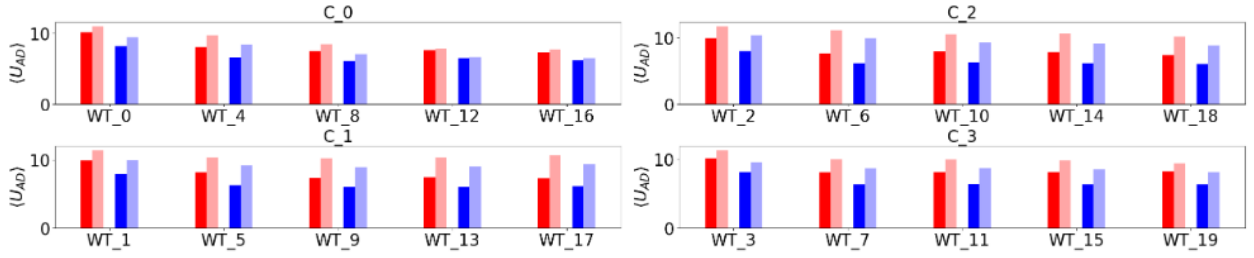

(a) (b)

Figure 18: Comparison of reconstructed flow-field data from amr-wind (red) and from OpenFAST (blue). Darker shade – LLJ, darker shade – MS.

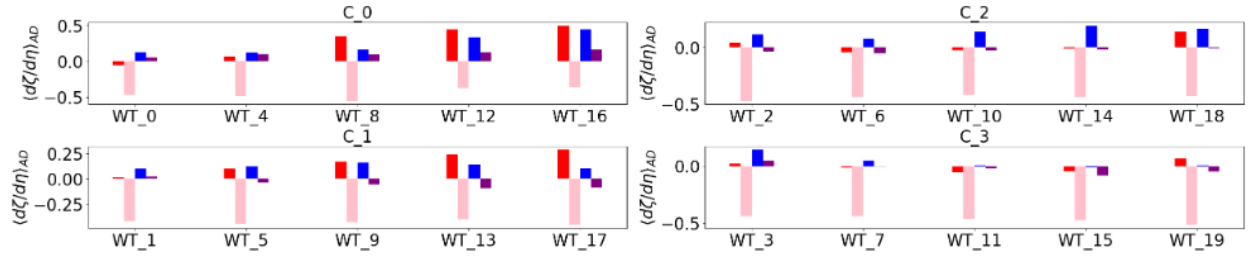

(a) (b)

Figure 19: Comparison of reconstructed flow-field data from amr-wind and from OpenFAST. Red – du/dz, LLJ. Pink – dv/dz, LLJ. Blue – du/dz, MS, Purple – dv/dz, MS.

4.1.1 Analysis of Integral Metrics

This section deals with the analysis of the integral metrics of the turbine system-level loads. Figure 20 documents the row-wise variation of the integral turbine rotor and control parameters, e.g., the generator power, blade pitch, rotor thrust and rotor average velocity. The differences in the topology in the turbulent structures of the LLJ and MS cases gets percolated in the rotor quantities as well. Just like the flow-quantities, the turbine outputs have been averaged across the lateral array of turbines at each row. This ensures that the statistical effects due to the lateral variation of the flow-field is minimized and results primarily demonstrates the effect of stream wise variation. The primary feature that influences almost all rotor quantities is the stronger wake deficit in the LLJ case compared to its MS counterpart. We see an average drop of 50 % turbine power in the downstream rows for the LLJ as opposed to <10 % drop for the MS cases. This can be attributed to the deep wakes (higher velocity deficits) with longer distances of recovery in the LLJ case. The deep wakes also cause progressive decrements of the rotor thrust, rotor torque and rotor aerodynamic twist in the downstream turbines for the LLJ case. The differences in the turbulent flow field between LLJ and MS also influences the blade pitch control. The stronger wake deficits and hence reduced velocity significantly pitches the blade in towards negative values which is finally capped by the controller resulting in zero pitch value (fine pitch β_{fine}) for the downstream turbines in the LLJ case. The primary function of the pitch control is to allow the rotor-shaft to operate in rated rpm condition. Due to the controller capping effect (min pitch $\beta_{min} = 0$), feedback control output for pitch control is capped as well resulting in rotor shaft operating at lower than rated speed condition. Both the wind farm simulation involving LLJ and MS cases were run with identical control algorithms for a fair comparison. The results related to the blade pitch and rotor rpm thus indicate the potential need for redesigning control algorithms for shallow boundary layers with strong wake deficits and wind veer. It is also important to note that turbine-control induces an ABL-specific non-linearity that modulates the wind turbine loads in a complex manner.

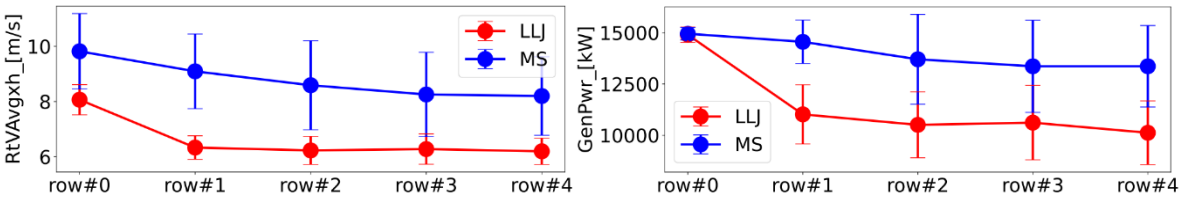

(a) (b)

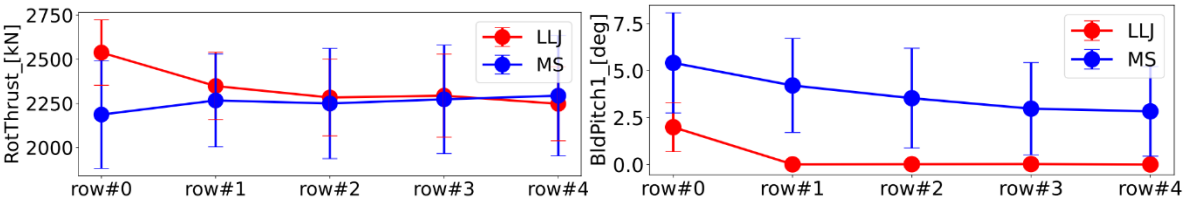

(c) (d)

Figure 20: Comparison of row-averaged mean and std. statistics of rotor quantities. (a) rotor-averaged velocity, (b) generator power, (c) rotor thrust, (d) blade pitch between coastal LLJ and baseline MS case for 20 turbine farm layout.

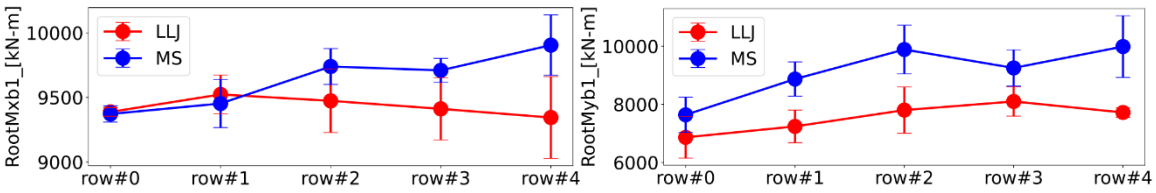

(a) (b)

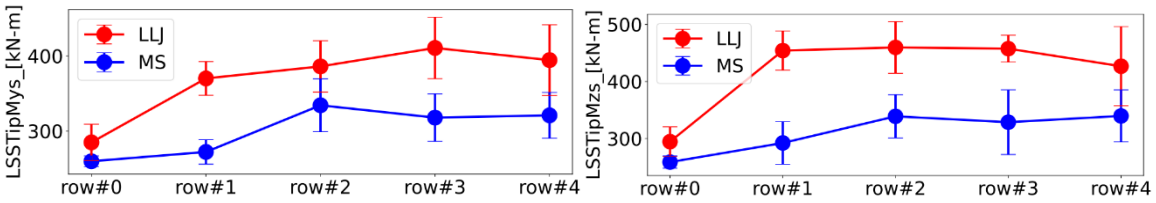

(c) (d)

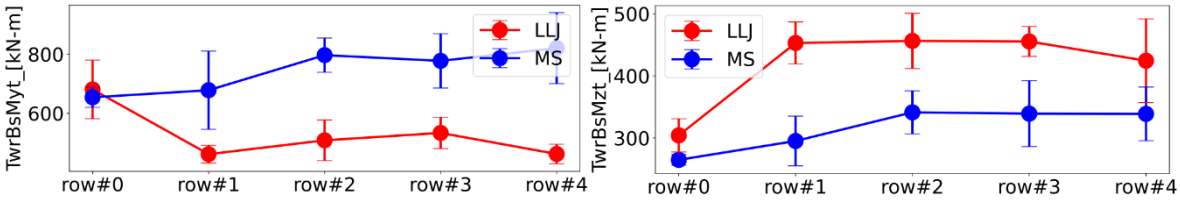

(e) (f)

Figure 21: Comparison of row-averaged DEL loads (a) Blade edgewise moment, (b) Blade Flapwise moment, (c) Low speed shaft y-bending moment (d) Low speed shaft z-bending moment (e) Tower fore-aft moment, (f) Tower torsion moment between coastal LLJ and baseline MS case for 20 turbine farm layout.

The wind turbine loads are a function of several flow features across the rotor and can be mathematically expressed as $\mathfrak{L} = f\left(\langle U\rangle_{AD}, du/dz, d\phi/dz, \langle TI\rangle_{AD}, \sigma_{\mathrm{du}/dz_*}, \sigma_{d\phi/dz}\right)$. While, $\langle U\rangle_{AD}$ is the primary driver for the mean loads $\overline{\mathfrak{L}}, \langle TI\rangle_{AD}$ contributes to the fluctuating loads $\mathfrak{L}'$ which can cause fatigue damage to the turbine systems. Additionally, we will see that certain turbine system loads are also triggered by the shear, veer and their fluctuations / std. dev. The turbine loads can be broadly categorized into the blade loads (edgewise, flapwise and torsion), tower loads (fore-aft, side-side and twist) and the hub loads (low-speed shaft and yaw bearing system). Turbine manufacturers are more interested in fatigue and ultimate (max) loads since they are responsible for turbine system-level damage. In this section we have compared the damage equivalent loads (DEL) of the LLJ and MS cases. For DEL loads a Wohler exponent of 12 is used for the blades while for hub & tower an exponent of 4 is used. We observe expected strong correlation between the std.deviation of the load and DEL owing to the fact that fatigue loads are inherently fluctuating in nature and driven by the turbulent intensity (TI). Strong reductions in the rotor-region TI for the LLJ case (Figure 17) in the progressive downstream can be associated with reduction in the blade DEL as well. The blade DEL loads for the MS case increases for the downstream turbines primarily due to the higher background TI and TI generation in the MS case. In Figure 21, the hub-loads, in particular, the low-speed shaft as well as the tower loads manifest an interesting feature. The mean loads for the rotating low-speed shaft bending moments (LSSTipMys, LSSTipMzs) are much higher for the LLJ case compared to the MS case. The z or the vertical bending moment is influenced by the presence of strong veer in LLJ, while the y or lateral bending moment is modulated by the strong shear in the rotor region that is observed in the LLJ. From Figure 19 it is apparent that the turbine pad locations for the LLJ case experience more negative shear (higher absolute shear) inducing rotor loads that dictate low-speed shaft bending. It is hypothesized that the stronger shear in the rotor-region is modulated by the presence of negative shear structure of the LLJ jet region, but further work is needed to validate the hypothesis. The DEL loads in the tower fore-aft moment are lower in the LLJ case owing to lower TI generation in the pad-level. However, the tower torsional moments (also the yaw-bearing systems torsional moments) are significantly higher (30 – 40%) as we propagate downstream of the turbines. This can be attributed to the strong veer content in the LLJ case. Although, the veer is an essential flow feature influencing the z (torsion/twisting) moment, the std. deviation of veer is smaller for the LLJ case compared to the MS case. It is not known if the presence of strong veer and TI in the LLJ case, themselves would trigger fluctuating structural moments in the z direction. Further in-depth analysis is required to confirm our speculative argument.

4.1.2 Analysis of Timeseries Correlations

In the previous sections we have analyzed the integral loads metrics and have observed the following trends (a) LLJ blade DEL loads are lower than the MS cases (lower TI in LLJ) (b) LLJ shaft bending loads and tower torsion loads are significantly higher than the MS counterpart (higher shear and veer) and made quantitative arguments between the loads and flow-metrics. In the present section, we compare the time-series correlation of the turbine system-level loads and the different flow-metric in order to highlight how the presence of turbine controller adds non-linearity to the arguments on "loads-flow" correlation.

Figure 22 illustrates a time-series comparison map of the rotor-thrust at different pad level locations against the rotor-averaged wind speed at pads for both stably-stratified LLJ case and the convectively unstable MS case. Note, for flow conditions and load conditions we use the same definition of filtering to reconstruct the time-series data as as done in Section 4.1. In the MS cases, the high velocity in the rotor-region forces the controller to pitch out blades which results in the anti-correlation (negative correlation), between the rotor-thrust and the rotor-averaged wind speed. In the downstream turbines the wind speeds are slightly lower (below rated), owing to which we can observe strong positive correlation between the thrust and wind speed. In the LLJ, however, the rotor-averaged wind speeds are mostly in the below-rated configuration resulting in a strong positive correlation between thrust and wind speeds, albeit with a short time-response / phase lag. The first row of turbines however, show smaller correlation between wind speeds and rotor-thrust due to the fact that the wind speed continuously switches from below-rated to above rated conditions inducing a high- amount of non-linearity. The subsequent figures in the section compute the trends of linear correlations (Pearson coefficient) between loads/control metrics and the flow-field metrics fort the LLJ case. In particular, for the surrogate rotor-averaged flow-metrics we look at $M_z, M_y, TI_z, TI_y, du/dz. dv/dz, d\phi/dz, du/dy, dv/dy, d\phi/dy$, where the z and y sub-scripts denote the reconstructed flow-fields using line-averaging in vertical z or lateral y direction. Additionally, the gradients of aligned wind, cross wind and the angle of the wind vector are also considered for a comprehensive understanding of the contribution of wind speed, TI and the shear, veer components of the wind that trigger system-level loads.

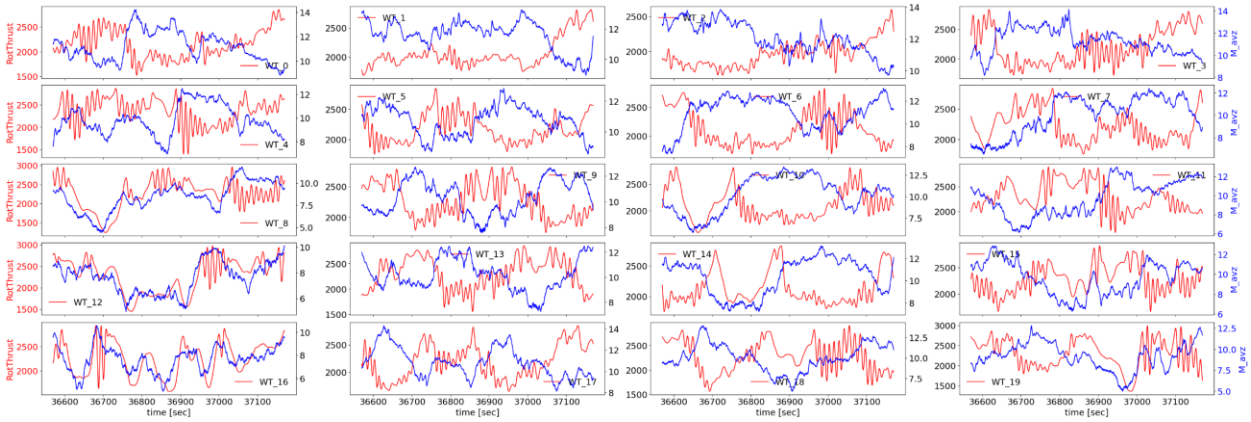

(a)

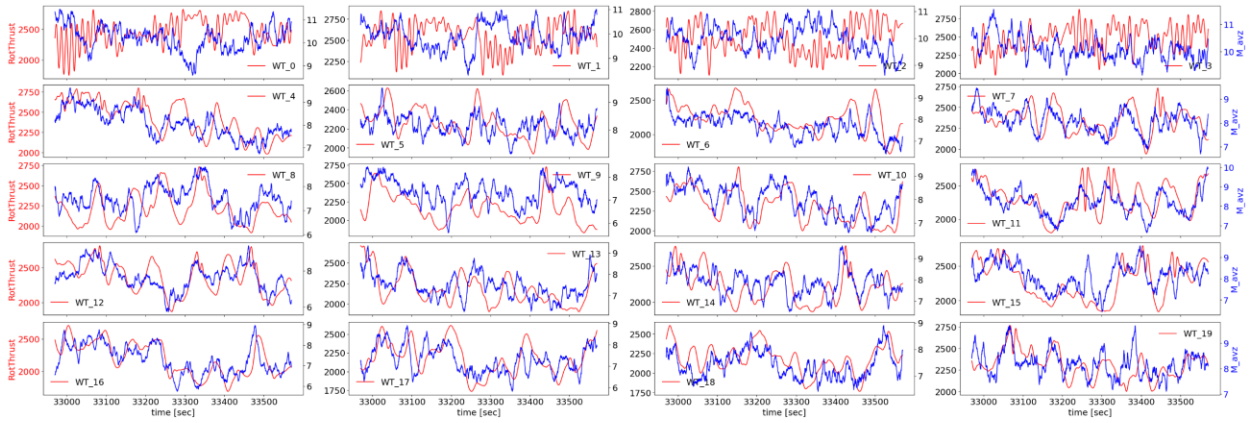

(b)

Figure 22: Time-series comparison of the (a) MS and (b) LLJ cases for the rotor-thrust with the mean rotor-averaged velocity at the 20 pad locations.

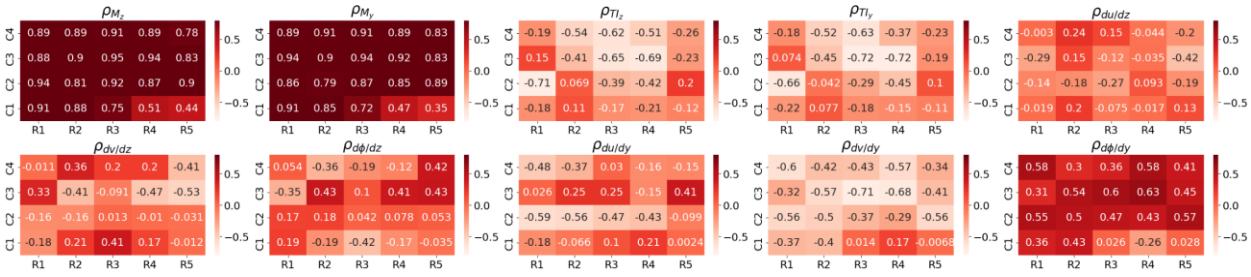

(a)

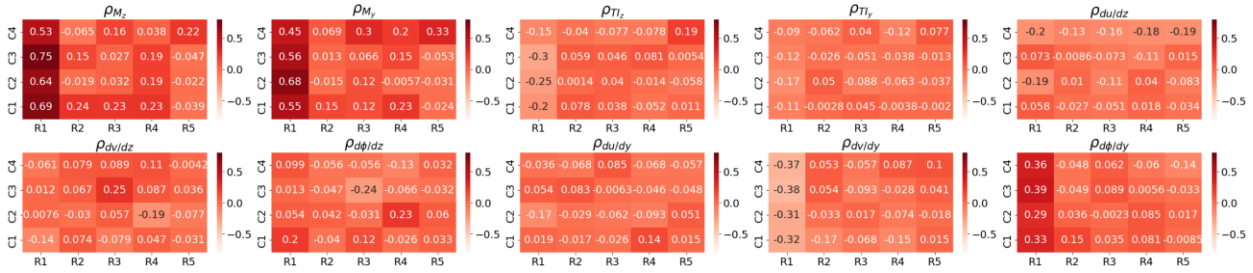

(b)

Figure 23: Comparison of heatmap depicting correlation coefficient of blade-pitch and the flow-metrics $M_z, M_y, TI_z, TI_y, du/dz. dv/dz, d\phi/dz, du/dy, dv/dy, d\phi/dy$ for the 20 wind turbine layout. Each box – arranged in 5 X 4 layout: left-right – aligned to wind direction. (a) MS (b) LLJ

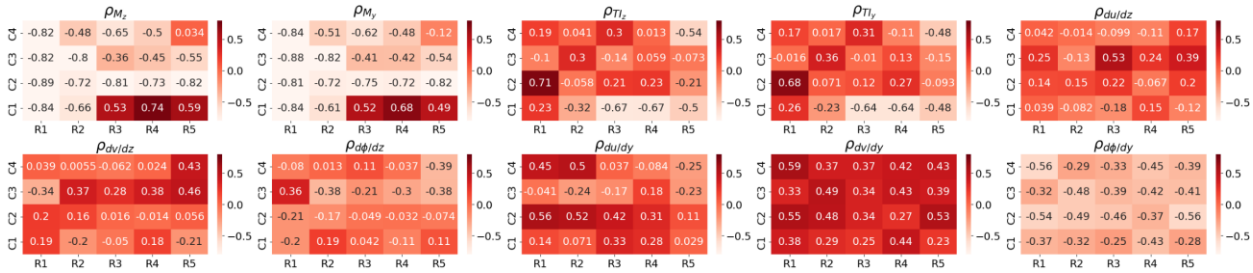

(a)

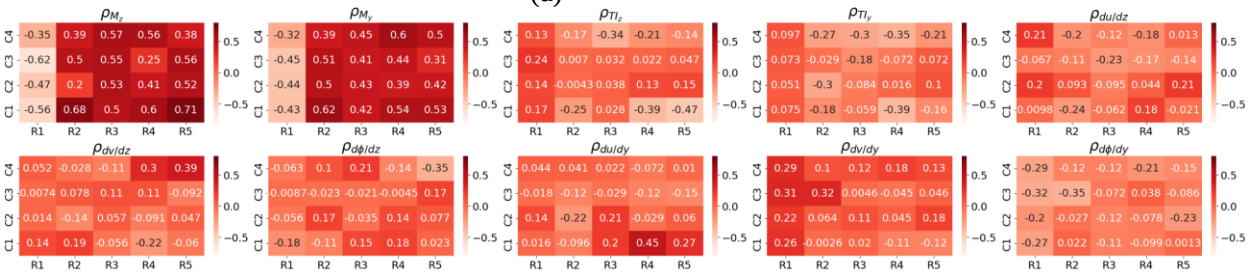

(b)

Figure 24: Comparison of heatmap depicting correlation coefficient of blade-root flapwise moment and the flow-metrics $M_z, M_y, TI_z, TI_y, du/dz. dv/dz, d\phi/dz, du/dy, dv/dy, d\phi/dy$ for the 20 wind turbine layout. Each box – arranged in 5 X 4 layout: left-right – aligned wind direction. (a) MS (b) LLJ

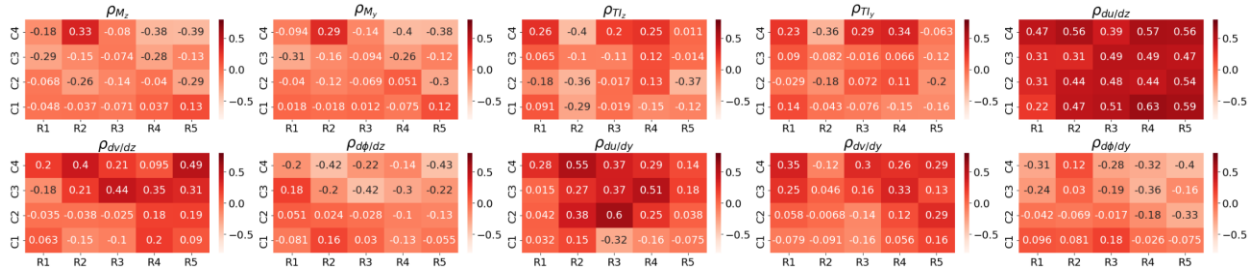

(a)

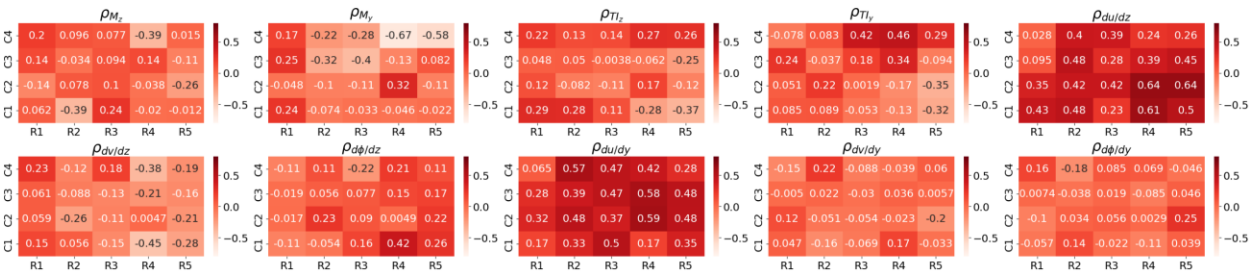

(b)

Figure 25: Comparison of heatmap depicting correlation coefficient of low-speed shaft bending moment and the flow-metrics $M_z, M_y, TI_z, TI_y, du/dz. dv/dz, d\phi/dz, du/dy, dv/dy, d\phi/dy$ for the 20 wind turbine layout. Each box – arranged in 5 X 4 layout: left-right – aligned wind direction. (a) MS (b) LLJ

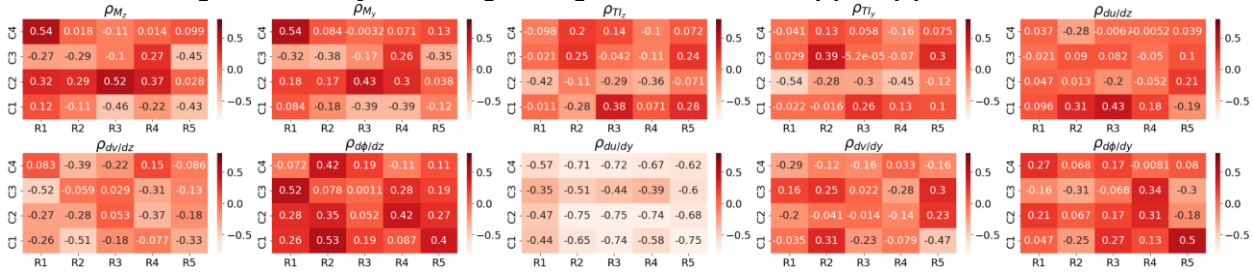

(a)

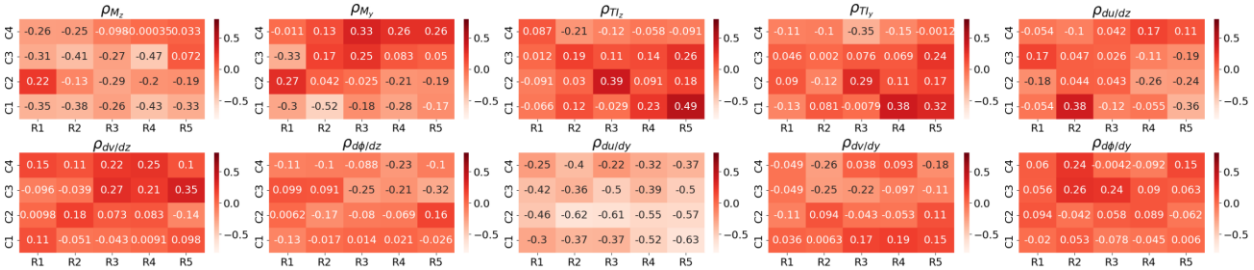

(b)

Figure 26: Comparison of heatmap depicting correlation coefficient of yaw bearing systems torsion moment (tower torsion moment) and the flow-metrics $M_z, M_y, TI_z, TI_y, du/dz. dv/dz, d\phi/dz, du/dy, dv/dy, d\phi/dy$ for the 20 wind turbine layout. Each box – arranged in 5 X 4 layout: left-right – aligned wind direction. (a) MS (b) LLJ

Figure 23 illustrates the heatmap depicting the correlation of the blade pitch with the flow-metric. As seen in the rotor-thrust time-series analysis, we observe a strong positive correlation (~0.8-0.9) coefficient with the both M_z, M_y, indicating that temporal information in both line average of velocity (surrogate of rotor-averaged velocity) are very similar to each other. A strong positive correlation between blade pitch and the rotor-averaged velocity is observed in the LLJ case as well in the first row of the wind farm. These correlations are reflective of the fact In the downstream turbines the wind speed decays significantly owing to stronger wake-deficits and hence the pitch is capped to a minimum pitch ($\beta_{min} = 0$) and reports quasi-zero correlation with wind speed. While sporadic strong correlations with blade pitch and other flow-metrics are observed in both LLJ and MS, but since they are not observed consistently over the entire farm, these correlation effects could be attributed to localized flow-changes owing to neighboring turbines. In a similar essence, strong negative correlations for MS and positive correlations for LLJ with the rotor-

averaged wind speed are observed for the flapwise moments. This is owing to the wind conditions operating in above and below rated conditions and the different effect of controller in those operating regimes. Apart from the rotor-averaged wind conditions, moderate correlations are also observed with the turbulence intensity (TI_z, TI_y) with the flapwise moments with negligible correlations with other flow-field metrics. Similar conclusions can be derived for the blade edgewise moments, rotor-thrust etc. For the blade shaft loads, we observe very strong correlations (~0.5) with shear component du/dz as well as lateral gradients du/dy of the aligned wind. This clearly indicates that apart from shear, du/dz, the lateral gradient also plays a critical role in low-speed shaft loads. Figure 26 illustrates the correlation between the torsion yaw bearing system moments (also tower torsion moment) and the flow field metrics. Moderate weak correlations are found with dv/dz while very strong correlations are found with du/dz indicating those these gradients contribute to the veer content of the flow which in turn influences the tower/yaw-bearing torsional loads at turbine pads.

Figure 27 illustrates a summary of the time-series correlation analysis through scatter plots in 3D space colored by corresponding loads. The scatter plots are done for all the 20 wind turbine pads combined together. The scatter plots clearly indicate clustered regions where the maximum loads are registered. The scatter plots clearly indicate that the clustering happens due a lurking non-linearity in this case the presence of controller.

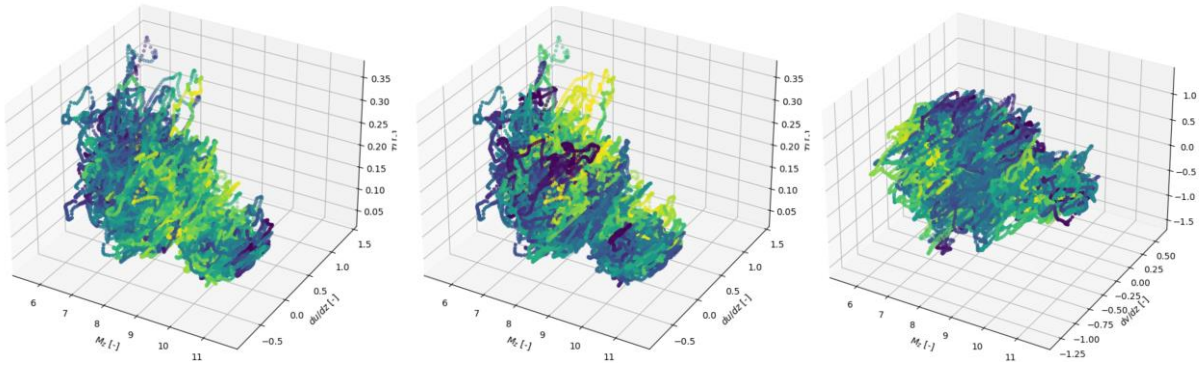

(a)

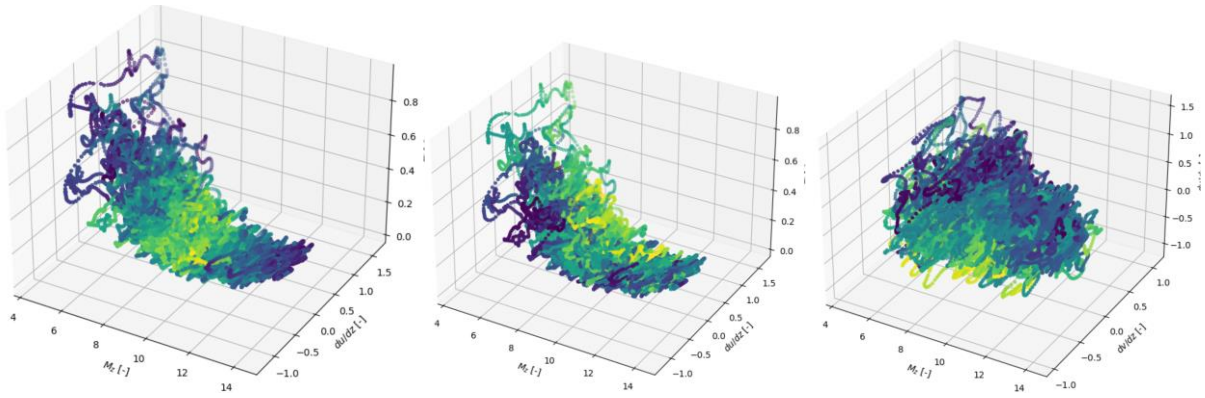

(b)

Figure 27: 3D Cluster map colored by loads. (a) LLJ, (b) MS cases. Left – color : Flapwise root moments, in $M_z, du/dz, TI_z$ space , Middle – color : low speed shaft moments, in $M_z, du/dz, TI_z$ space , Right – color: yaw bearing torsion / tower torsion moments, in in $M_z, dv/dz, du/dz$ space.

4.2 Summary of Key Takeaways

The analysis in the current section indicates that the flow conditions in the coastal LLJ are morphologically different from the convectively unstable MS case which gets reflected in the load response. While the load remains with the DLC load envelopes, the (i) **blade fatigue loads** for the LLJ cases are lower than the MS cases due to lower *TI* while the (ii) **low-speed shaft, yaw bearing/tower torsion DEL** loads are significantly higher for the LLJ due to higher shear and veer content in LLJ. The trends of the integral load metrics are further corroborated by time-series correlation between loads and flow-field metrics. The correlation analysis further illustrates that time-series correlation indicates an additional layer of complexity due to the turbine controller that **cannot be captured solely from the pearson correlation analysis.** However, the correlation analysis do indicate that for regions of stronger correlation – the loads are directly influenced by the variation of flow-fields and the effect of controller is solely linear in nature. This section in principle, addresses a) the integral load metrics – what loads are higher in LLJ, and b) correlation analysis – why the loads are higher (flow-field causality) which provides a gateway of design of load mitigation strategy which is discussed in the next section.

5 Mitigation of Low-level Jet Impacts

5.1 Strategies for Mitigation and their Effectiveness

In section 4.1 we have performed loads analysis in wind turbine framework and have identified how the turbine system level loads are influenced by flow field metrics. Additionally, we have further identified higher low-speed shaft DEL loads in the coastal LLJ environment. The current section takes on the outlining strategy for the damaging loads mitigation and identify the advantages and disadvantages of the mitigation methods using coarse LES simulation study.

5.1.1 Outline Strategies

Table 5 highlights the different strategies that have been used for loads mitigation of coastal LLJ, e.g., (i) Derating, (ii) Individual Pitch Control (IPC) & iii) Yaw-Presets. In principle, derating is a methodology where operating condition of a wind turbine is modified to reduce the C_p and hence the power generated by the wind turbine. Derating is handled via the input files in open-source ROSCO controller in the OpenFAST solver by simply tuning the turbine operating/control parameters. Derating has its implications in the modulation of the operating points in λ, β phase-space where λ is the TSR [-] and β is the pitch angle in degrees. The four primary derating strategies we have used are enumerated as a) Reduction of Ω_{rated}, the rated rotor speed of the low-speed shaft rotor, b) Reduction of the rated power, P_{rated}, c) Increasing the fine-pitch and minimum pitch angle β_{fine} , β_{min} of the blades and d) peak shaving methodology designed to "shave" the peak of the rotor thrust curve and subsequently reduce the tower loads.

Individual pitch control (IPC) is a potential loads mitigation strategy where pitch of each turbine blade is controlled separately on the top of the collective pitch control (CPC). While CPC is activated when the hub-height wind speed is in above rated condition, IPC is intrinsically tied to blade root moments rather than wind speeds. IPC algorithms are designed in the frequency space where the objective is to use pitch to reduce blade root moments at specific frequencies, 1P (once per revolution), 2P and 3P via multibody coordinate transform (MBC). Derating & IPC is handled via the input files in open-source ROSCO controller in the OpenFAST solver by simply tuning the turbine operating/control parameters.

The yaw-preset strategies are thematically different from derating and IPC in the sense that the primary objective of yaw-preset is not tied to loads mitigation, but rather wake optimization to maximize power harvest. Note, the yaw-preset strategy is open-loop in nature and the optimized yaw -misalignments are

obtained from steady-state analysis using FLORIS. Yaw-preset methodology is also evaluated as a potential candidate for loads-mitigation for coastal LLJ since the strategy is also closely tied with modified operational settings of the turbine.

Mitigation Strategies	Controller Tuning Necessary?	Details
Derating	Yes	Modify operational settings of turbine by moving $C_p, C_T \; in \; the \; pitch - TSR \; space$
Individual Pitch Control (IPC)	Yes	Individual pitch control via yaw and tilt blade root moments over collective pitch control
Yaw-Presets (Open Loop)	No	Create yaw-misalignments in farm based on power optimization stategies

Table 5: Various load mitigation strategies for wind-farms in coastal LLJ

5.1.2 Single Turbine Stand-alone Analysis to Guide LES

Evaluation of mitigation strategies can be computationally expensive if performed using LES of wind farms, particularly in the derating and yaw-preset space due to the significant number of degrees of freedom involved (4 derating strategies, many different tunings per strategy, and various sub-optimal yaw-presets with load-mitigation as primary objective). Consequently, the mitigation strategies have been down-selected using stand-alone OpenFAST simulations driven by coastal LLJ wind conditions (precursor-LES) prior to being tested on wind farms using coarse LES. The stand-alone OpenFAST simulations provide an additional advantage of gaining insights to the physics of load-mitigation strategies apart from setting a down-selection criterion. For derating cases & yaw-presets, the down-selection/evaluation is performed by evaluating heat-maps of the mean, std.dev and max loads reduction which are tied to fatigue and ultimate damage. For example, Figure 28 illustrates the heat-map for mean, std.dev and max system-level loads. Derating using lower rated power capacity is the safest option since it leads to significant loads reduction in blade flapwise as well tower loads, the low-speed shaft loads do not

change significantly. However, derating using lower power capacity, also causes a significant reduction in C_p and power, which jeopardizes the farm AEP, and hence not desirable. In that context, peak-shaving strategy is the most desirable from the derating standpoint since it causes nominal changes in power and reduction of tower and shaft loads are observed. In the coarse LES simulations for mitigation strategy evaluation, we have explored peak-shaving strategies as well as reduction of rated rotor strategies for evaluating their performance from the farm -standpoint.

In a similar spirit, Figure 29 illustrates the heatmap of loads for different yaw-preset conditions. The stand-alone runs illustrate that mean, std.dev as well as max loads increase with yaw-misalignments. However, since the DEL loads were observed to increase downstream, we expect yaw-misalignment in the upstream turbines would deflect the wakes and hence have ameliorating effect on the downstream loads.

Figure 28: Heatmaps depicting deviation (%) of turbine system-level loads from the baseline configuration (no derating) for rated wind speed. Deviation of (%) (a) - mean loads, (b) std. dev loads, (c) - max loads. Load considered: Mxb - edgewise blade moments, Myb - flapwise blade moments, LSSy, LSSz - outof plane low-speed shaft bending moment, T wrX - tower foreaft moment, T wrY - tower side-side moment and Y awX, Y awY, Y awZ - yaw bearing systems - pitch, roll and yaw-twisting moments. Ω_η - rated shaft speed reduction - η%. Pwr_η - rated power reduction with η% and PS_η - peak shaving with η% (Symbols used in Heatmaps). Max DLC envelope loads: < 100 [mN-m] with blades, < 400 [mN-m] for tower

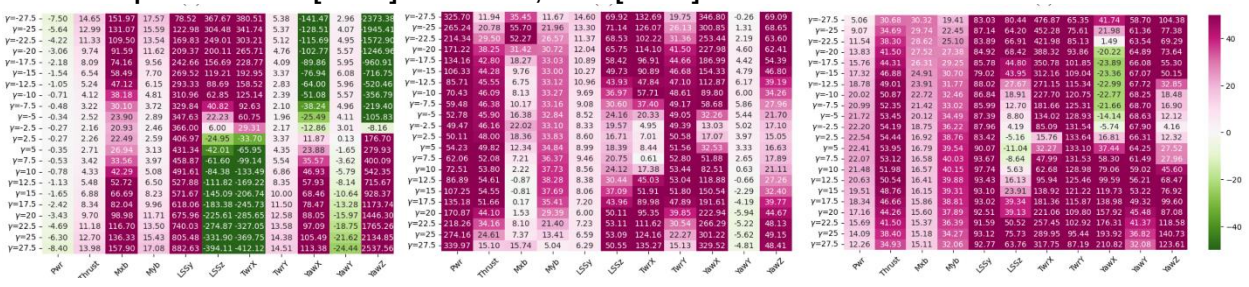

Figure 29: Heatmaps depicting deviation (%) of power, thrust & turbine system-level loads from the baseline configuration (no derating) for rated wind speed. Deviation of (%) (a) - mean loads, (b) std. dev loads, (c) - max loads. Load considered: Mxb - edgewise blade moments, Myb - flapwise blade moments, LSSy, LSSz – out of plane low-speed shaft bending moment, TwrX - tower foreaft moment, TwrY - tower side-side moment and YawX, YawY, YawZ - yaw bearing systems - pitch, roll and yaw-twisting moments. γ – yaw-misalignment

in degrees. (Symbols used in Heatmaps). Max DLC envelope loads: < 100 [mN-m] with blades, < 400 [mN-m] for tower.

5.2 Evaluation of Mitigation Strategies in Windfarms using LES

The current section deals with the results of coarse LES simulations (10 m resolution) conducted for several derating strategies, IPC vs non-IPC and a suite of yaw-preset cases. The section tries to capture of the high-level finding from the study. In this section we handle the different mitigation strategies by analyzing the flow-physics / wake-deficits since it plays a key role in spreading the local derating effects to the entire farm-level. Note, the primary difference between the stand-alone OpenFAST simulations and the higher fidelity coarse LES simulations are differences attributed due to the presence of induction and waked regions and higher pad-level turbulence intensity, which can have significant influence on the load calculation in LES simulations. The implications of the different mitigation strategies in terms of turbine system levels loads and its technical viability are illustrated in Section 5.2.4.

5.2.1 Derating

In general, derating methodologies result in weaker wake deficits at the hub-height and rotor region along with suppression of augmented turbulence owing to LLJ wind interception with the rotor. The outcomes are illustrated in Figure 30 using line plots. The derating strategies modulate the induction region at D upstream of the turbine by $\leq 1\%$ compared to the baseline case, while the wake deficits are reduced by $\sim 50\%$ in the derating cases compared to the baseline. Additionally, the turbulent intensity at the pad locations reduced by $\sim 20\%$ owing to the presence of peak shaving strategies. This is primarily because the wind turbine blades in derating strategies are allowing more air to pass through itself and offering less blockage. This is inherently tied to the minimum pitch schedule implemented in the controllers for peak-shaving strategy. Note, for the baseline cases $\beta_{min} = 0$, for rated and above rated conditions, while peak-shaving strategies illustrate quasi-linear growth of β_{min} with wind speeds and β_{min} increases with the peak shaving intensity. (70% to 95%). For lower shaft speeds, the wake suppression is again tied to the wind turbine offering less blockage to air. Additionally, if derating strategy (peak-shaving / lower shaft speed) is implemented only in the first-row turbine, the effect of suppressed wakes propagates further downstream to a few turbines (***lagged response***) before non-derating effect kicks in with the last turbine demonstrating strong wake deficit. Consequently, it can be said, that even though the derating strategy is localized to a single turbine by tuning the controller, the effect of turbine derating propagates to multiple turbines downstream through the wakes.

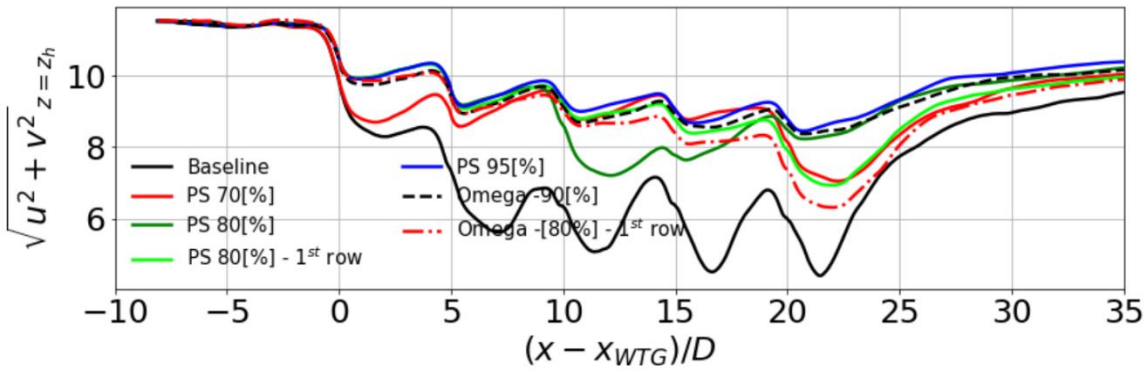

Figure 30. Line plots of streamwise evolution of wind-speed deficits at hub-height in the 5 × 1 wind turbine array using coarse LES. x_{WTG}: streamwise location of 1st turbine, D – turbine diameter. $(x - x_{WTG})/D$ = 0, 5, 10, 15, 20 – pad location of 5 turbines. Legends- Cases: PS-70%, PS-80%, PS-95% , No-PS – apply peak-shaving/no-peak shaving at all 5 rows, PS-80 1st row – apply peak shaving at 1st row – no peak-shaving for row2-5 , Omega 90% - apply 90% rated shaft speed all rows. Omega 80% 1st row – apply 80% rated shaft speed at 1st row, no derating in row 2-5.

5.2.2 Individual Pitch Control

Figure 31 compare the wake behavior between the Collective Pitch Control (CPC) only (baseline) and IPC simulations. From time averaged line plots we can observe qualitatively similar behavior between CPC only and IPC simulation, Figure 31 further shows slight improvement in the wake recovery from the IPC simulations when compared against CPC only simulation. This additional improvement is due to the pitch actuation which controls the wind passing through undisturbed and thus influence the rotor thrust along with the wake behavior. This marginal improvement in wake recovery shows the potential of IPC to not only reduce loads on various components but also positively influence wake recovery and thus overall farm power production.

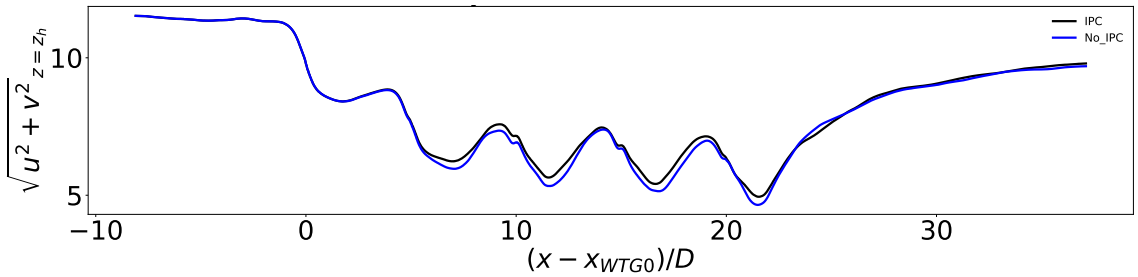

Figure 31. Line plots of streamwise evolution of wind-speed deficits at hub-height in the 5 × 1 wind turbine array using coarse LES. x_{WTG}: streamwise location of 1st turbine, D – turbine diameter. $(x - x_{WTG})/D$ = 0, 5, 10, 15, 20 – pad location of 5 turbineswind speed M at hub-height $z = z_h$. Legends: IPC & No IPC (Baseline).

5.2.3 Yaw Control

We performed LES of a windfarm flow within a single turbine array of 5 turbines with yaw presets determined from FLORIS optimization in response to the mean wind profile. These yaw settings were

optimized to yield ~20% increase in power capture as estimated using FLORIS. We adopted this configuration for the LES runs in the current milestone to assess the relationship between flow science, performance and model fidelity. The yaw misalignments shown in Figure 32 are signed quantities, i.e. positive represents counter-clockwise rotation and negative clockwise. In this case FLORIS predicts a counter-clockwise rotation to help improve performance although a clockwise rotation would work equally well given the symmetric wake structure being estimated in such models. However, given the strong veer and shear in the LES, we expect the sign of these misalignments to have consequences in terms of loads when performing coarse LES simulations. Figure 32 illustrates the mean velocity profile for the baseline and two different yaw configurations. We do observe deflections in the wakes for the yawed turbines. The impact of these flow modifications is not lost on the turbine performance. This counter-intuitive observation is a likely consequence of the controller being able to sufficiently account for the power capture through pitching of the blades appropriately.

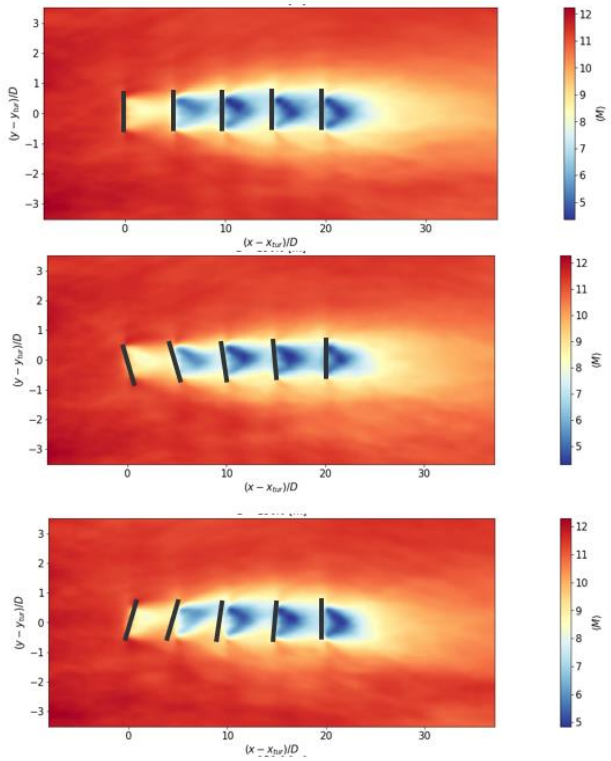

Figure 32 Mean flow structure of the hub height horizontal plane for the three different yawed set-ups – baseline (top), counterclockwise yaw (middle, +25 deg max) and clockwise yaw (bottom, -25 deg max).

5.2.4 Overall Summary

In the current section we provide a comparison of turbine system level loads statistics for different load mitigation strategies evaluated for coarse LES simulations. Figure 33 and Figure 34 illustrates a summary

plot of the relevant loads of wind turbine system for various derating conditions, yaw presets and IPC (individual pitch control) strategy. The box-whiskers plots in Figure 33 illustrate the farm-averaged loads in terms of the mean, std. deviation, max, min and a coarse quartile distribution of the loads time-series. The mean loads are a direct consequence of derating strategies and inherently tied to the controller algorithm, (e.g., pitching out to result in lower aerodynamic torque and hence lower *edgewise moments*). However, the mean loads do not have significant influence on the life of the turbine system if they are within design envelopes. The std. dev of the loads serves as surrogates to the DEL loads while the max and min of loads indicate the ultimate loads of the turbine system. We observe that the edgewise (RootMxb1) loads are minimally influenced by the different strategies of derating, yaw-presets and IPC, the max loads are ~15% lower in the peak-shaving cases. The ultimate and the DEL/std.dev flapwise root moments (RootMyb1) indicate that the max/ultimate flapwise loads are comparable for the yaw & IPC cases (10% decrement at extreme yaw) while they are significantly lower for the derating cases (10-40% decrement). The std. dev loads for RootMyb1 are comparable except in the few derated cases. The max shaft loads (LSSTipMys, LSSTipMzs) are 50% lower in the peak-shaving cases as well as the yaw-presets (yaw-misalignment of + 25 deg). Similar outcomes are illustrated in the yaw-bearing system as well. We observe the sign of shaft and yaw bearing loads are affected by the sign of the yaw-misalignment error (+25, +40 vs -25, -40 deg) but the magnitudes are comparable. The IPC strategy also indicates ~5-10% drop in the max and std.dev of rotor loads and low-speed shaft loads. In general, the IPC & yaw-preset strategy also performs better with the tower fore-aft/side-side and the torsion moments. Due to the *triggering of resonance of the tower vibrations* (modal frequency ~ 0.18 Hz), the std. dev and the max tower loads of the derating strategies are significantly higher (over the DLC envelope of 400 Mn-m) and can cause tower system failure. Figure 34 illustrates the probability density function of the generator power for the different load mitigation strategies implemented in the wind farm LES simulations. The plot is appended with a Generator power violin plot which shows the avg, min and max power generated in the farm for the different strategies. Except for the IPC strategy, both derating and yaw-presets indicate loss of power due to reduced aerodynamic torque and smaller wind speed interception at yaw respectively. But most importantly, the pdf indicates that apart from power loss, the different strategies have different probability distribution of power generation and is inherently tied to the fact that different strategies alter the wind speed in the farm significantly and in a unique way.

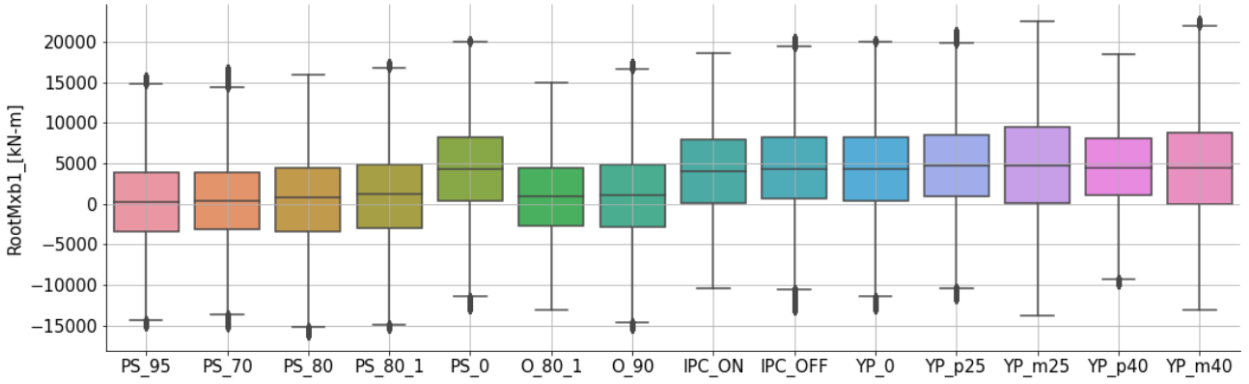
RootMxb1_[kN-m]
20000
15000
10000
5000
0
−5000
−10000
−15000
PS_95
PS_70
PS_80
PS_80_1
PS_0
O_80_1
O_90
IPC_ON
IPC_OFF
YP_0
YP_p25
YP_m25
YP_p40
YP_m40

(a)

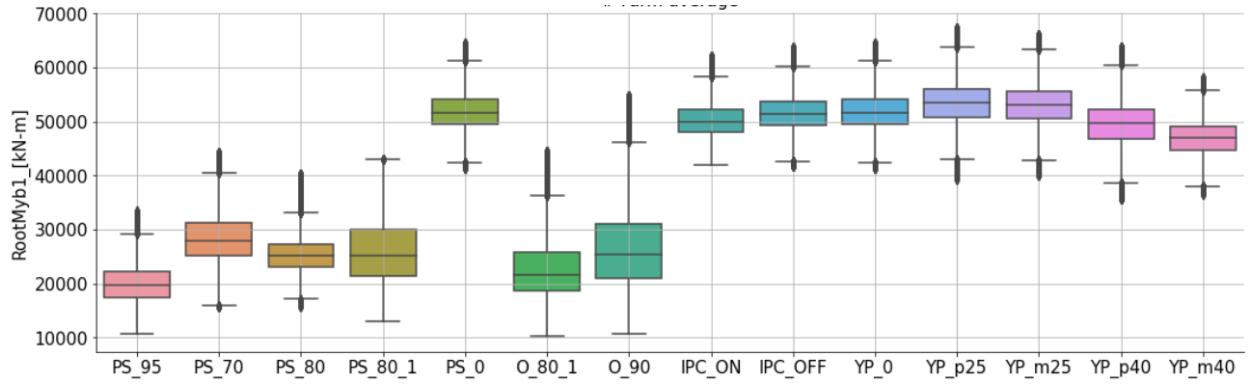
RootMyb1_[kN-m]
70000
60000
50000
40000
30000
20000
10000
PS_95
PS_70
PS_80
PS_80_1
PS_0
O_80_1
O_90
IPC_ON
IPC_OFF
YP_0
YP_p25
YP_m25
YP_p40
YP_m40

(b)

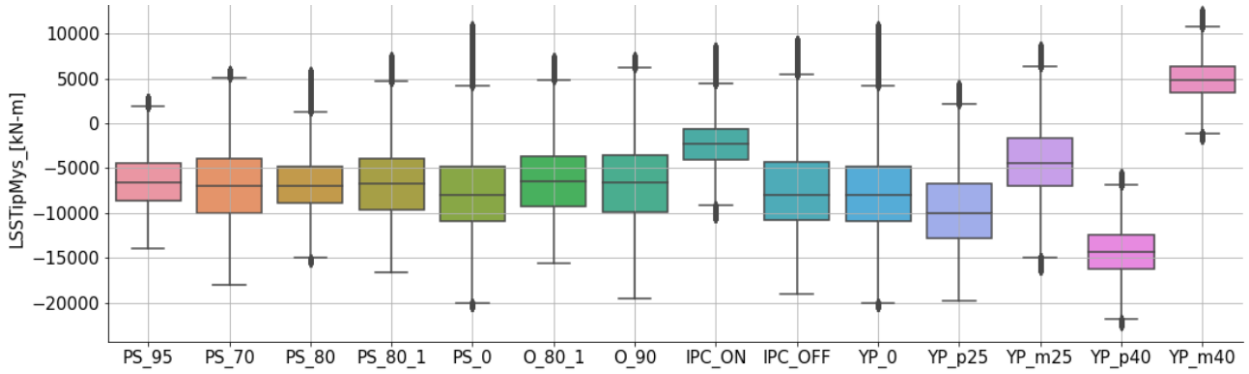
LSSTipMys_[kN-m]
10000
5000
0
−5000
−10000
−15000
−20000
PS_95
PS_70
PS_80
PS_80_1
PS_0
O_80_1
O_90
IPC_ON
IPC_OFF
YP_0
YP_p25
YP_m25
YP_p40
YP_m40

(c)

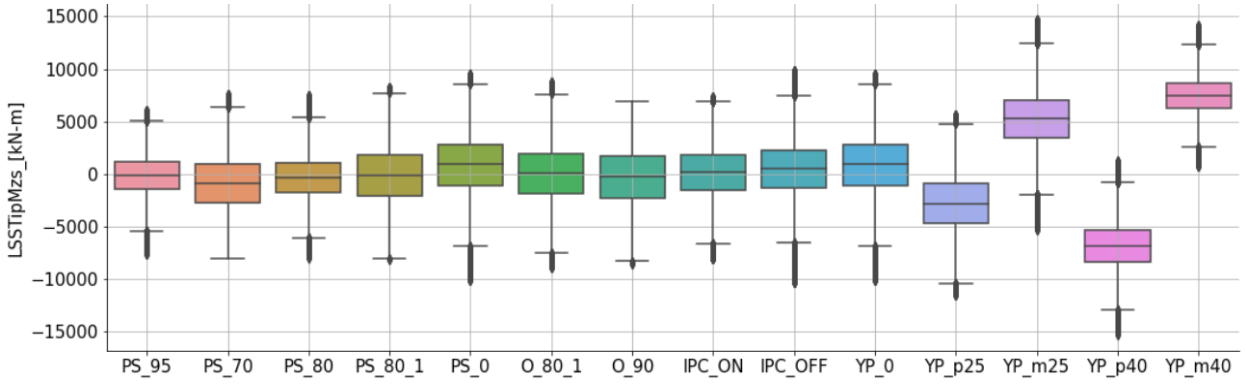
LSSTipMzs [kN-m]
15000
10000
5000
0
−5000
−10000
−15000
PS_95
PS_70
PS_80
PS_80_1
PS_0
O_80_1
O_90
IPC_ON
IPC_OFF
YP_0
YP_p25
YP_m25
YP_p40
YP_m40

(d)

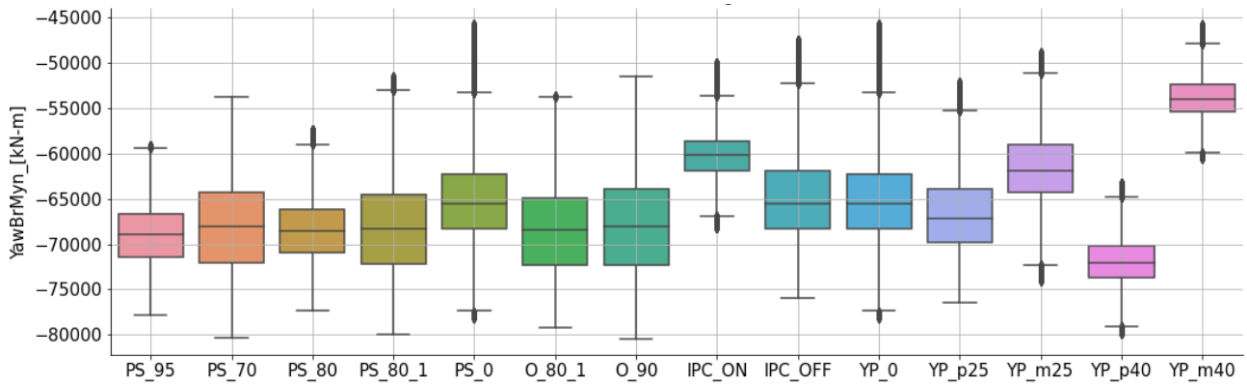
YawBrMyn_[kN-m]
−45000
−50000
−55000
−60000
−65000
−70000
−75000
−80000
PS_95
PS_70
PS_80
PS_80_1
PS_0
O_80_1
O_90
IPC_ON
IPC_OFF
YP_0
YP_p25
YP_m25
YP_p40
YP_m40

(e)

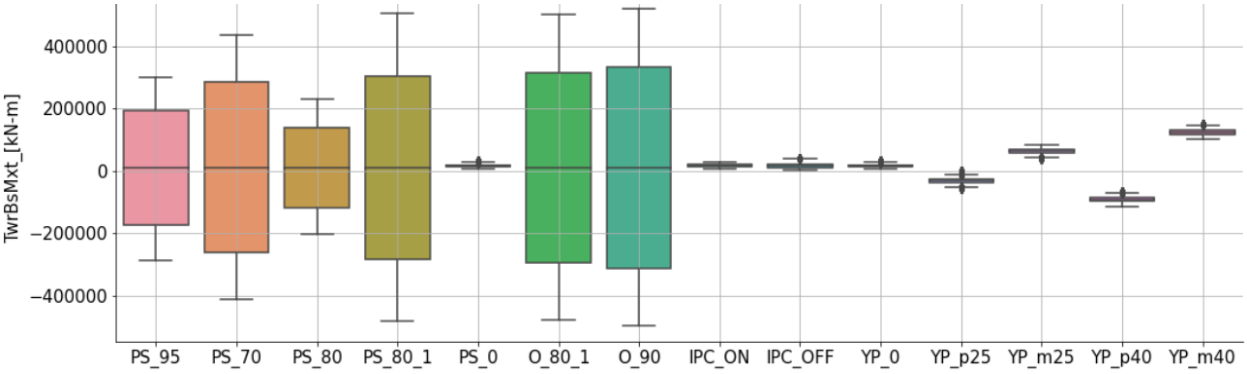
TwrBsMxt_[kN-m]
400000
200000
0
−200000
−400000
PS_95
PS_70
PS_80
PS_80_1
PS_0
O_80_1
O_90
IPC_ON
IPC_OFF
YP_0
YP_p25
YP_m25
YP_p40
YP_m40

(f)

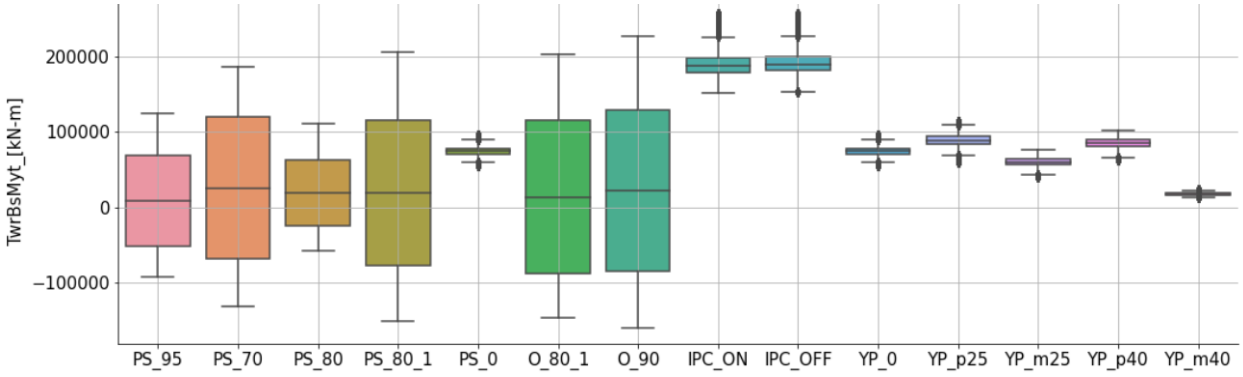

(g)

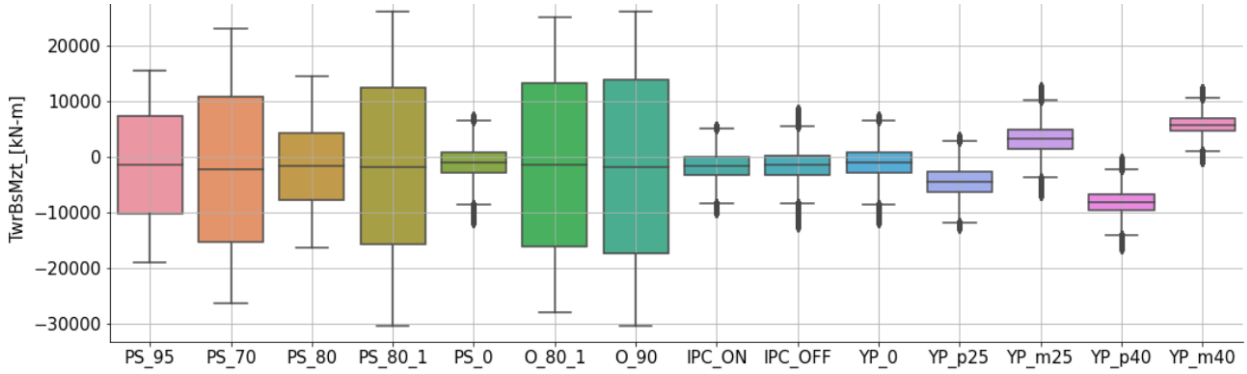

(h)

Figure 33. Categorical box-whiskers plots indicating the mean, std. min and max of the load channels (along with distribution) for the derating, IPC and yaw-preset cases. (a) blade-root edgewise moment (b) blade-root flapwise moment (c) low-speed shaft bending moment in the lateral y direction (d) low-speed shaft bending moment in the vertical z direction (e) yaw bearing pitching moment (f) tower side-side moment (g) tower fore-aft moment (h) tower twisting moment

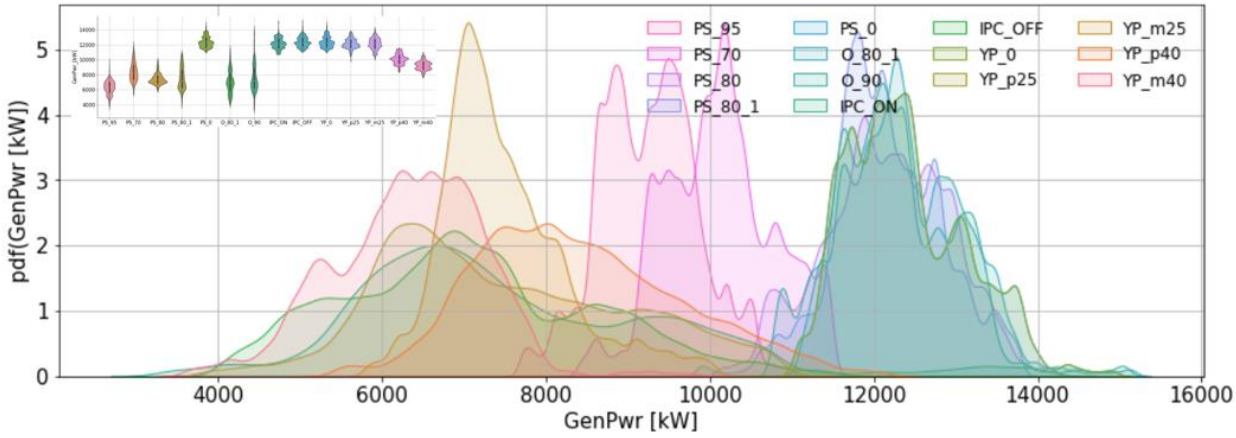

Figure 34. Probability density function of the mean generator power (farm-averaged) for the different derating, IPC and yaw-preset strategies. Inset: Violin plot of farm-averaged generator power for different strategies.

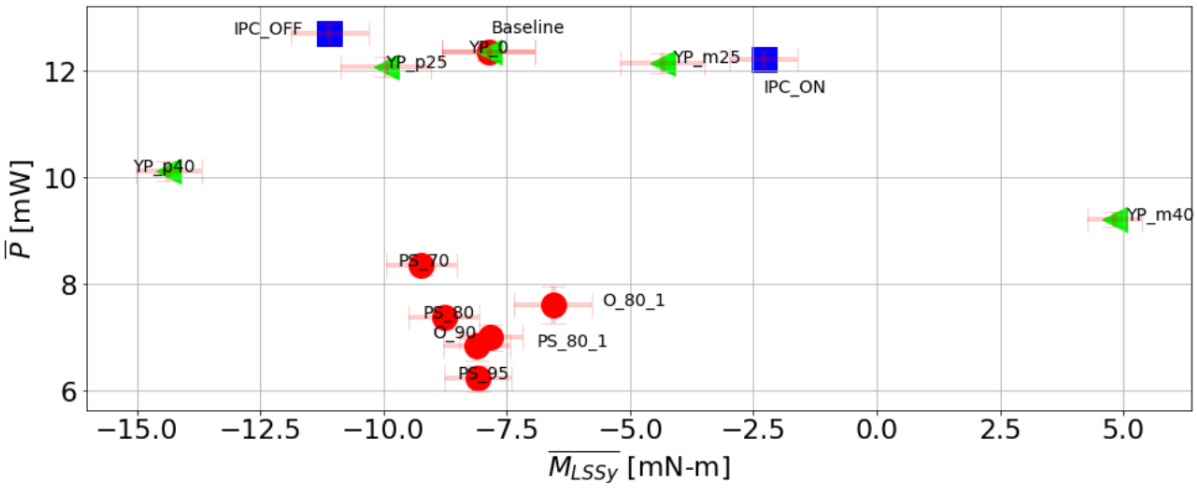

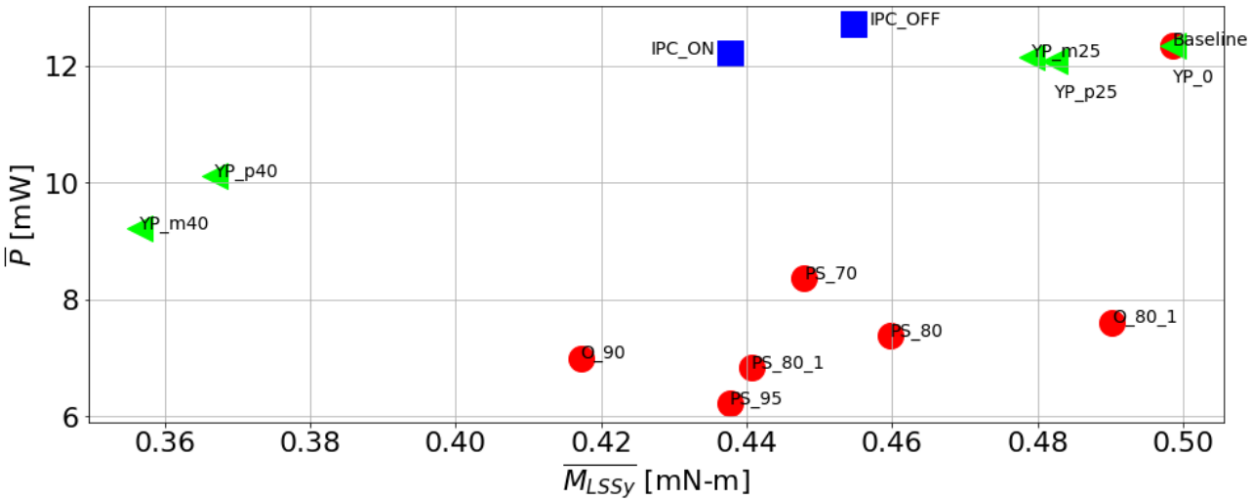

Figure 35 A Comparative analysis of the integral metrics for the single array windfarm across the different mitigation strategies when operating in a low-level jet environment. Top: Scatter plot of farm-averaged power and farm-averaged mean shaft tilt loads; Bottom: Scatter plot of farm-averaged power and farm-averaged DEL shaft tilt loads. The symbols in red represent derating cases, green – yaw steering and blue – individual pitch control.

Given the analysis in the preceding sections, it becomes imperative that we provide a holistic comparison of the different strategies. To this end, we plot integral metrics of the power and shaft loads (mean and DEL) in Figure 35. The integral metrics are the farm averaged temporal means of the rotor power and farm-averaged temporal means (and DELs) of the shaft yaw loads. These are presented as scatter plots in Figure 35 with the top image corresponding to the mean loads and the bottom to the DEL loads. In these plots, the goal of any mitigation strategy will be to not lose farm-level power (if not enhance it) while reducing loads of interest. We observe that the derating strategies (red symbols) result in significant loss of farm level power (by design) with modest changes in mean loads. The most reduction in mean shaft tilt loads is observed for the CW 40deg uniformly yawed condition with modest losses in power capture. However, when power capture is taken together with load reductions, the best performance is realized for the case with IPC.

In practical turbine operation, the variability in loads is more important from the standpoint of fatigue life of components. Therefore, we also consider the DEL loads for these different numerical experiments in the lower image in Figure 35. We observe that the lowest shaft tilt DEL loads (~25% decrease) is observed for the uniformly yawed cases but with ~30% loss of power. Unlike the mean loads, IPC on shows slight decrease in DEL loads (5%) without compromising on power. Therefore, the choice is often between power reduction and load reduction. Table 6 illustrates the summary observations of the various load mitigation strategies implemented in coarse LES simulations. The derating strategies in general do not perform well as far as loads and power are concerned, the yaw-presets do not impact the loads significantly, while allowing for potential farm power gains. The IPC strategy performs the best in terms

of loads reduction with nominal changes in power, coupled with a better wake recovery making it a viable candidate of load mitigation. One of the caveats of IPC is significant increase in pitch rate that will lead to significant load on the pitch actuation mechanism that could eventually lead to premature failure of pitch actuation mechanism. A future activity that can be pursued would be to modify the control algorithm to impose some bounds on the maximum pitch rate while still reducing the blade root moments and loads on other rotating and no-rotating components.

Mitigation Strategy	Observations	Comments
Derating	Minimal improvement on shaft loads, significantly higher max/DEL tower loads along with rotor-loads reduction & farm power loss.	Derating strategies are easy to implement in controller, but no generic solution, and the strategy would be site-specific, wind condition dependent. Derating can potentially give rise to higher turbine tower/yaw loads.
IPC	Improvement in shaft and tower loads, without the significant drop in power & rotor loads, better wake recovery	IPC can cause nominal drops in system-level loads, useful solution for providing loads within envelope, but not a mature technology owing to high pitch rate involved.
Yaw-Presets	Power drop in yawed turbines are nominal – pitch controller adjustment at above rated condition. Nominal turbine load changes.	Yaw presets might be a desirable solution, not from the load mitigation strategy, (no significant load reductions), but would contribute to farm power gains.

Table 6: Summary of observations and outcomes of derating, IPC and yaw-preset as load mitigation strategies.

6 Multifidelity Modeling of Windfarm-Low-level Jet Interactions

6.1 Levels of Modeling Fidelity

A parallel goal in this study is to evaluate and improve the performance of low-order models relevant to simulation of windfarms which form the core of the engineering toolbox. In this study, we explore three levels of modeling fidelity – analytical or semi-analytical models, medium fidelity models that employ hybrid strategies and high-fidelity models where the full complexity of the system is faithfully represented. The high-fidelity model prediction is considered as the ground truth against which the reduced-fidelity models are compared against.

6.1.1 Steady-state Wake Models

The various steady-state analytical wake models were implemented within FLORIS[1] - an open-source framework for modeling windfarm power predictions. FLORIS consists of steady-state analytical wake models derived from time-averaged RANS (Reynolds-Averaged Numerical Simulation) equations that is used primarily to estimate AEP. FLORIS version 3.0.1 includes a number of analytical and empirical wake calculation modules that were covered in more details in milestone 4.1 report (section 2.1).

Recall that the Gaussian wake model is based on analytical solutions to the linearized Navier-Stokes whereby the wake deficit is computed assuming a Gaussian wake for the three-dimensional velocity $u(x, y, z)$

$$u(x, y, z) = U_\infty \left[C_{GCH}(\sigma_y, \sigma_z, c_t \dots)\, e^{-\frac{(y-\delta)^2}{2\sigma_y^2} - \frac{(z-z_h)^2}{2\sigma_z^2}} \right] \quad (1)$$

and where U_∞ is only the U-component vector of the freestream (undisturbed) velocity averaged over the rotor disc plane, C_{GCH} is the velocity deficit at the wake center according to the Gaussian Cumulative Hybrid (GCH) model (a function of wake width σ_y in y direction, σ_z in z direction and thrust coefficient c_t among other variables), δ is the wake deflection, z_h is the hub height, given as (u_R is the velocity at the rotor, u_0 is the velocity behind the rotor, x_0 is the start of the far wake region)

$$\sigma_z = k_z(x - x_0) + \sigma_{z0} \;; \qquad \sigma_{z0} = \frac{1}{2}\sqrt{\frac{u_R}{U_\infty + u_0}} \quad (2)$$

[1] https://floris.readthedocs.io/en/v2/source/code.html

$$\sigma_y = k_y(x - x_0) + \sigma_{y0} \;; \qquad \sigma_{y0} = \sigma_{z0}\cos\gamma\cos\theta \tag{3}$$

and this empirical relationship (tunable constants with recommended values of $k_a = 0.383, k_b = 0.004$)

$$k_z = k_y \equiv \; k = k_a\, TI + k_b \tag{4}$$

Equation (3) adds a rotation angle θ in the wake width calculation. The input to this rotation is defined as a wind veer feature and is only available in the GCH model at the moment.

The notable differences between the CC and GCH models are that the CC model implicitly accounts for wake combinations in its derivation and does not require a separate superposition method, and includes a near-wake model. The cumulative wake effect in the CC model is included by adding the summation of $\sum_{i=1}^{n-1} \lambda_{ni} C_i / U_\infty$ (C_n is the wake center deficit of the current turbine n and λ_{ni} captures the wake contribution of upstream wind turbine i) in the C_{CC} term as well as other major modification of equation (1) as shown (σ_n has the same form as σ_y, σ_z with dependence on parameters k and x_0)

$$u(x,y,z) = U_\infty \left[C_{CC}(\sigma_n, \lambda_{ni}, \gamma \ldots)\, e^{-\frac{\tilde{r}^m}{2\sigma_n^2}} \right] \tag{6}$$

where $\tilde{r}^m$ is a modification of the exponential coefficient in equation (1) with additional tunable parameters.

6.1.1.1 Simulation set-up

The domain in FLORIS was set up to correspond to the sizes of the data slices taken from AMR-Wind for hub height (HH) plane shown in Figure 36 (a), for center line (CL) plane and rotor plane (RP). The three farm configurations are 1) a single turbine is placed at 6 RD from the domain edge 2) five turbines placed in a single row at 5 RD apart and 3) 4 rows of 5 turbines with rows placed at 4 RD apart.

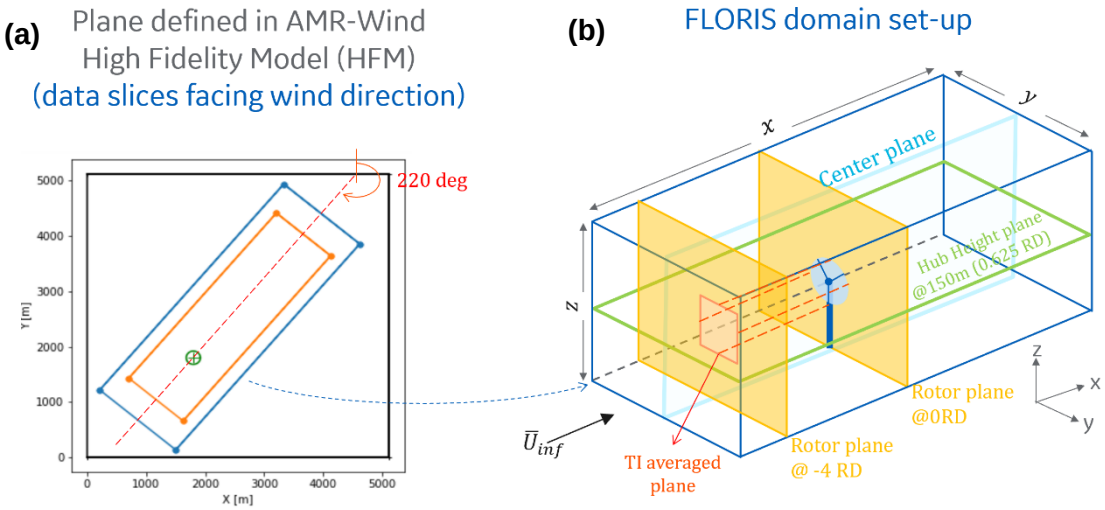

Figure 36: (a) Domain set-up and data slices (blue frame) in AMR-Wind and (b) the matching domain size and initial conditions defined in FLORIS

The initial conditions such as the initial TI and inflow velocity $\overline{U}_\infty$ are averaged across a squared area of 1 x 1 rotor diameter (RD) at -4 RD upstream of the first wind turbine as shown in Figure 36 (b). These initial conditions are extracted from AMR-Wind data slices and fed into FLORIS as input. Note that the magnitude of the freestream velocity $\overline{U}_\infty$ averaged over the rotor disc plane from LES data is supplied as the U-component of the freestream velocity U_∞ in equation (1) as explained in section.

Additionally, the undisturbed velocity profile for the full plane at -4 RD upstream is extracted from AMR-Wind as inputs to FLORIS. This estimate of a 4D upstream was tested for multiple atmospheric conditions to ensure that the inflow wind is reliably undisturbed and carries little induction effects. Lastly, the development of analytical models embedded within FLORIS approximate the turbine wake as periodic (i.e. assumes an infinite wind farm) in the streamwise direction. On the contrary, we note that the wakes modeled using LES/actuator line method (ALM) in AMR-wind represent a finite-sized wind farm. Any discrepancies arising herein from such approximations ought to be considered as a modeling limitation inherent to FLORIS and cannot be altered by considering larger simulation domains to minimize periodicity effects.

6.1.1.2 Model evaluation metrics and tuning strategy

In this study, the GCH and CC wake velocity (deficit) models in FLORIS are evaluated against LES data from AMR-Wind in terms of capturing both accurate wake and power predictions. The initial conditions of freestream velocity magnitude $\overline{U}_\infty$ and turbulence intensity TI are matched in both FLORIS and AMR-Wind and four user-input tunable parameters $\{k_a, k_b, \alpha, \beta\}$ are used to achieve optimum wake and power predictions.

The main properties that describe a wake is its amplitude (depth, peak), width (spread) and shape (distortion, stretching). From both the GCH and CC Gaussian formulation in equations (1) and (6) respectively, we see that the values of $U_\infty C_{GCH}$ and $U_\infty C_{CC}$ will affect the wake amplitude. The values of $\{k_a, k_b, \alpha, \beta\}$ all feed into σ in equations (2) – (4) which in turns affects the wake spread as a function of streamwise distance and ultimately the values of the wake deficit $C_{GCH}(\sigma_y, \sigma_z, c_t \dots)$ and $C_{CC}(\sigma_n, \lambda_{ni}, \gamma \dots)$. In short, the tuning parameters of $\{k_a, k_b, \alpha, \beta\}$ impacts both the wake amplitude and width through parameters k and x_0. We can further decrease the tuning parameters to three by setting $k_a = 0$ and reducing the dependence of k on only k_b from equation (4) since initial TI was constant. This way we can easily obtain the value of $k = k_b$ from this tuning exercise for other cases with different TI values.

The default values for all parameters in FLORIS have been tuned to agree with empirical values in literature based on power generation predictions. As pointed out in Bay et al [11] study which tuned the velocity models with high fidelity data from SOWFA, the TI has a dominant effect on the wake depth (TI effect is linear on wake width/spread and inversed on wake amplitude/depth). The study also chose to compare the GCH and CC models with SOWFA at a specific point of 7 rotor diameter downstream. We perform both qualitative (isocontours of flow field) and quantitative assessment (averaged profiles and line plots, integral metrics) to understand the complex effects of the selected tunable $\{k_b, \alpha, \beta\}$ variables on wake and power predictions while matching $\overline{U}_\infty$ and TI with the LES data.

6.1.1.3 Qualitative wake characteristics

Contour error plots of the rotor planes provide a qualitative metric to assess the wake shape i.e where the wake cross-sectional shape in AMR-Wind departs from the typical axi-symmetrical Gaussian. Therefore, Figure 37 and Figure 38 show the contour error plot of the wind speed magnitude difference between FLORIS and AMR-Wind in the rotor planes at various distances x at $\{-2.5, 1.5,4,5,6\}$ rotor diameters using the GCH and CC models respectively. Figure 39 shows the contour error plots in the center line plane for using (a) GCH and (b) CC models. All three contour error plots show matching initial condition for $\overline{U}_\infty = 12\ \mathrm{m/s},\ TI = 9.66\%$ in both FLORIS and AMR-Wind and default model parameters $k_a = 0.38, k_b = 0.004, \alpha = 0.58, \beta = 0.077$. They offer an important qualitative metric in cases where wind veer has significant effect. Under these idealized monotonically-sheared wind conditions, it is clear there are no significant wind veer effects as the wake deficit remains almost perfectly centered around the rotor center.

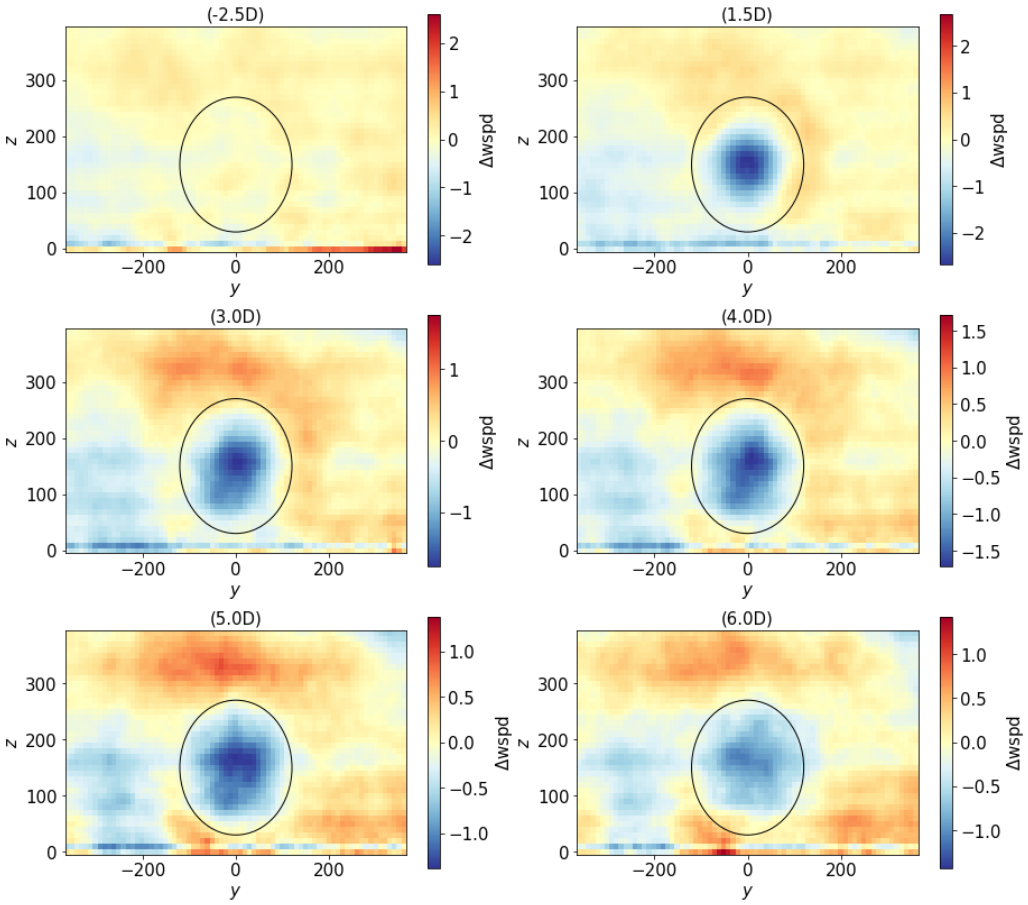

Figure 37: Contour error plot of the wind speed magnitude difference between FLORIS and AMR-Wind in the rotor planes at distances {-2.5, 1.5, 3, 4, 5, 6} RD using the GCH model [$\bar{U}_\infty = 12\ \mathrm{m/s},\ TI = 9.66\%$] with default tunable parameters. Note the black circular line is the outline of 1 rotor diameter.

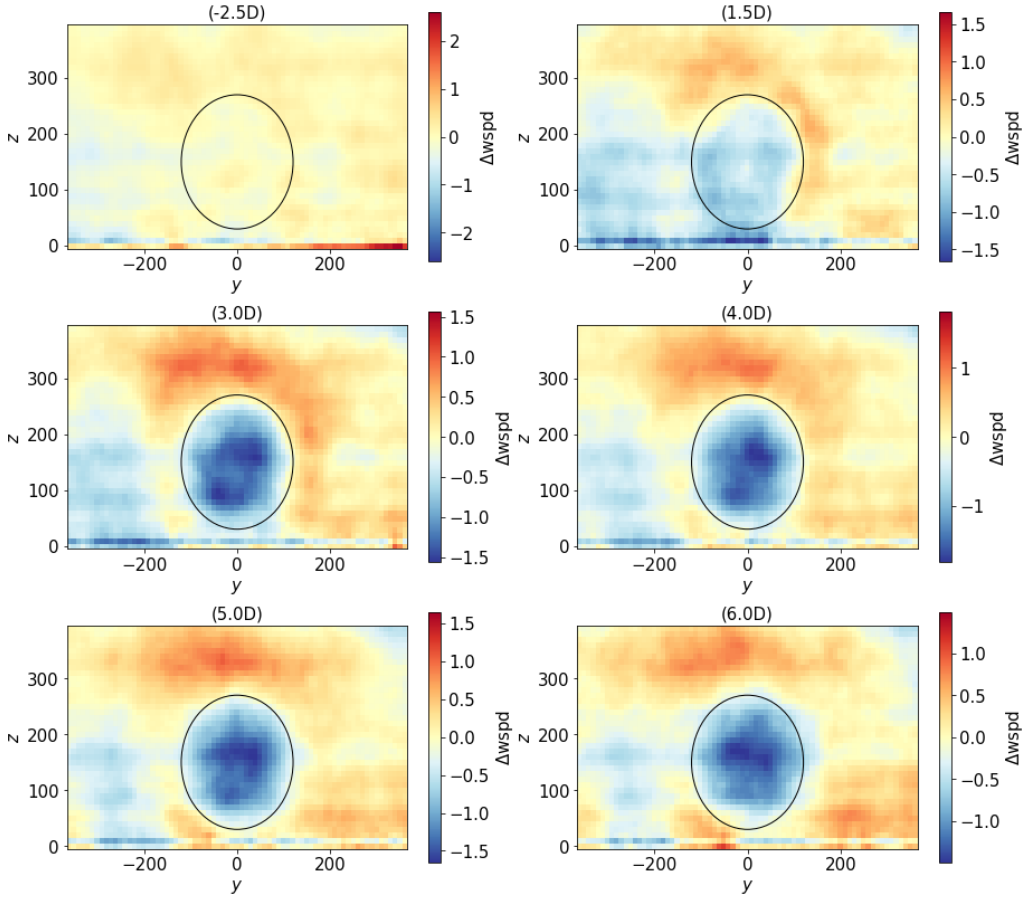

Figure 38: Contour error plot of the wind speed magnitude difference between FLORIS and AMR-Wind in the rotor planes at distances {-2.5, 1.5, 3, 4, 5, 6} RD using the CC model [$\bar{U}_\infty = 12\ \mathrm{m/s},\ TI = 9.66\%$]. Note the black circular line is the outline of 1 rotor diameter

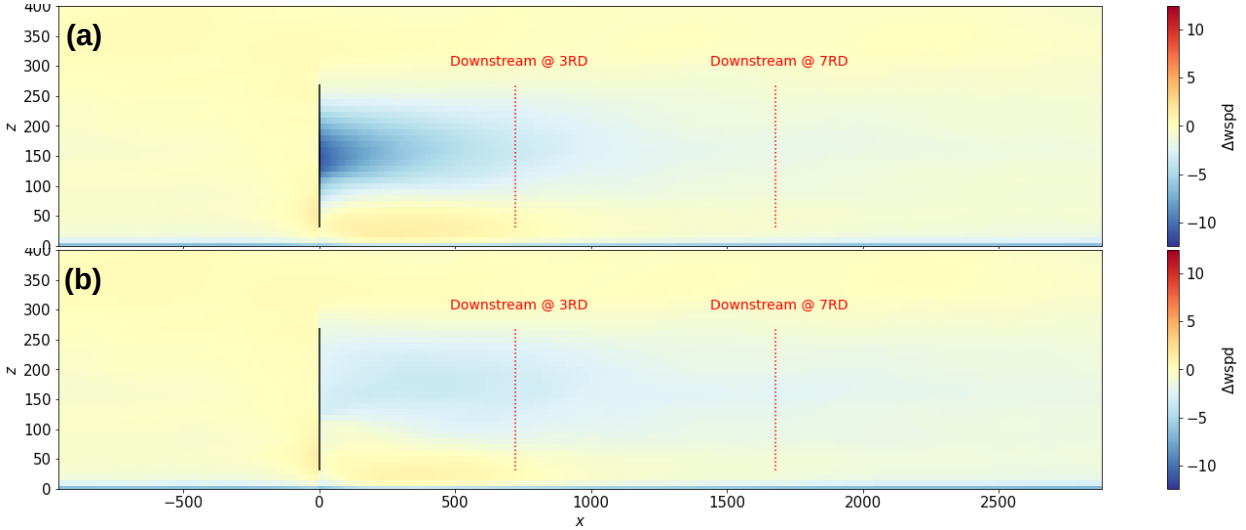

Figure 39: Contour error plot of the wind speed magnitude difference between FLORIS and AMR-Wind in the CL plane using (a) GCH and (b) CC models [$\bar{U}_\infty = 12\ \mathrm{m/s},\ TI = 9.66\%$] with default parameters. The red dotted lines highlight the near ($0 \leq x \leq 3$ RD), intermediate ($3 \leq x \leq 7$ RD) and far ($x \geq 7$ RD) wake region

There is a unique aspect to the wake structure observed in the LLJ environment such as the distortion of the wake profile rotated "bean" shape as shown in Figure 40 (a). This arises from the shallowness of the ABL in the presence of LLJ which causes the veer and shear effects to be pronounced. We note that such wake distortion extends well outside the 1 RD as shown in the later sections of this report. The distortion and extent outside the 1 RD are a departure from the typical axi-symmetrical Gaussian observed in a MS event shown in in Figure 40 (b).

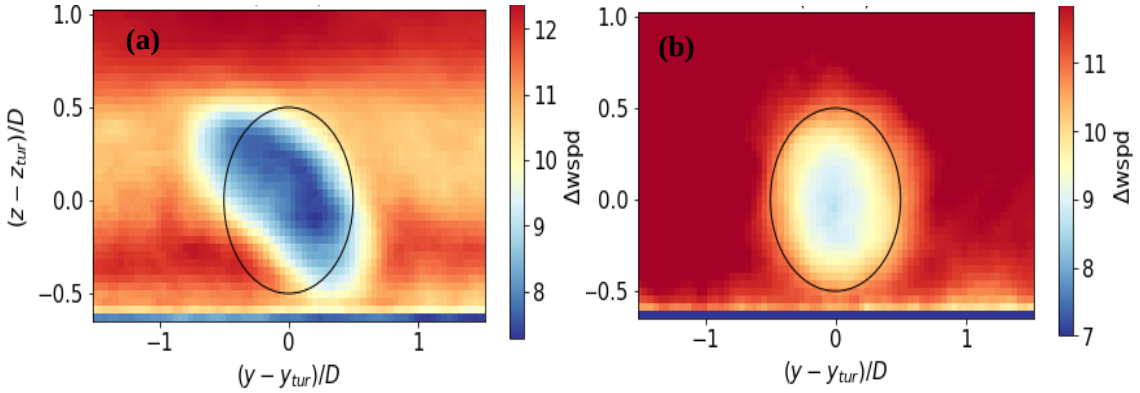

Figure 40: Contour plot of the rotor plane at -1.5 RD downstream for the LES data from AMR-Wind showing a (a) clear distortion of the wake that extends beyond 1 RD in a LLJ environment and (b) Gaussian wake outline in an MS environment. Note that the black circle represents the outline of the turbine blades at 150 m radius

In addition to the visualization of the rotor plane data, we also look at the streamwise evolution of the turbulent wakes in both a vertical plane passing through the center of the turbine(s) and aligned perpendicular to the turbine rotor plane. We denote this as the "CL (Center-Line) plane". Additionally, we also sample data in a plane oriented horizontally, passing through the turbulence center at the hub height and oriented perpendicular to the turbine rotor plane – named "HH (Hub-Height) plane". The contour plot in the HH plane of the velocity v- and w-components in Figure 41 show an overall v-component contribution and the w-component show an apparent rotation effect around the rotor center in the near-wake of the wind turbine.

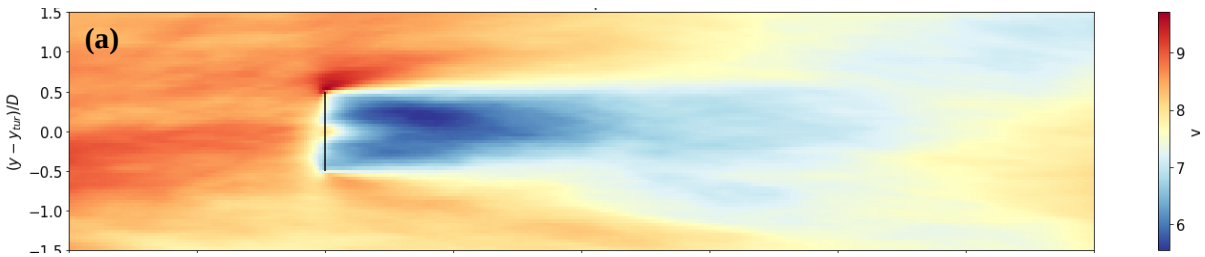

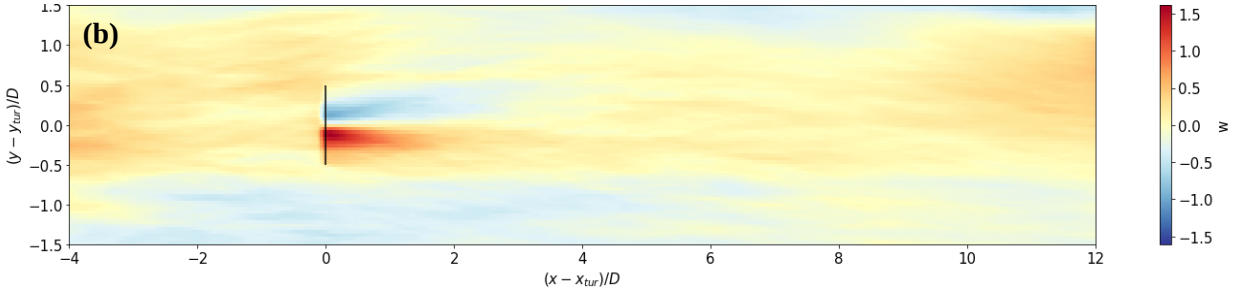

Figure 41: Contour plot of the LES data from AMR-Wind in the HH plane for the (a) v-component showing a general overall contribution in the background flow and (b) w-component showing an apparent rotation effect around the rotor center in the wake. The same were observed in the HH plane for MS event.

From the velocity profile for the LLJ event, extracted from AMR-Wind data slices at an upstream location at -4D (four rotor diameters upstream) a rotor-disc averaged estimate of the windspeed is estimated and used as the input, U_∞ to equation (1). We note that this since U_∞ is vector magnitude, it is unaffected by the presence of wind veer as is the case for the LLJ. The wind veer is roughly estimated from the orientation of the inclined major axis in the distorted rotor plane wake deficit of Figure 40 (a).

The GCH model results in a wake profile that is mirrored across the center plane if no wind veer is specified as shown in Figure 42 (a). Specifying an angle of $\theta = 310$ deg results in a distortion of the wake profile within the rotor plane with the primary axis at an angle of θ with the north as shown in Figure 42 (b). In these studies, the θ is treated as a tunable parameter to achieve the best match with the LES data. The range of values adopted for θ is from 270 → 90 degree, i.e. -90 → 90 degrees. Therefore, $\theta = 310$ deg implies a veer orientation along the south east- north west directions. This allows us to qualitatively match the wake-distortion in the LLJ environment albeit after significant tuning from LES data.

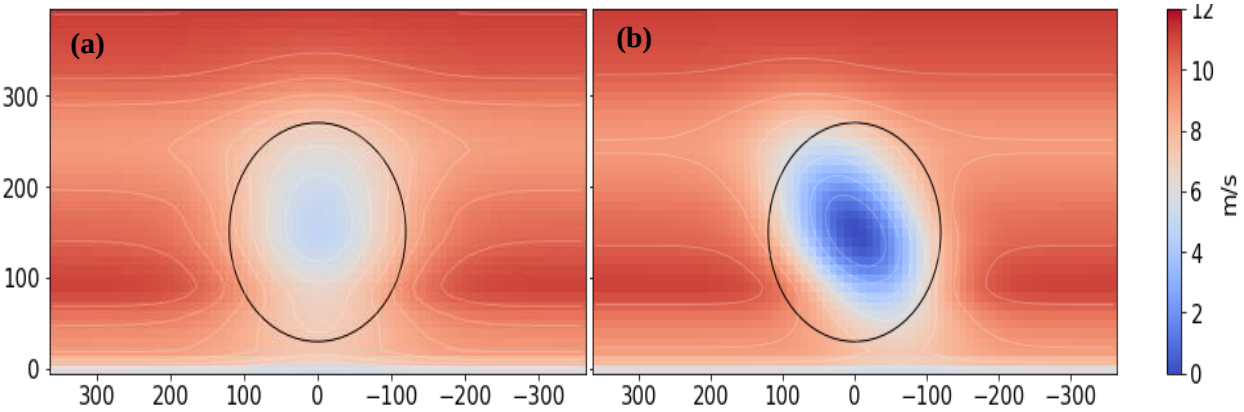

Figure 42: Contour plot of a wake profile in the rotor plane at a downstream distance of -1.5 RD in FLORIS using GCH model with a wind veer specification (a) $\theta = 0$ deg and (b) $\theta = 310$ deg. Note that the black circle represents the outline of the turbine blades at 150 m radius

In addition to such qualitative analysis, we leverage quantifications such as the Root-Mean-Squared-error (RMSE) between the velocity magnitude $\overline{U}$ across a rotor area (n grid points) predicted in FLORIS and AMR-Wind across each rotor plane at streamwise x distances. This provides for an overall quantitative metric for the wake deficits as defined below:

$$RMSE(x) = \sqrt{\frac{\sum_{i=1}^{n}\left(\overline{U}_{i\ FLORIS}(x) - \overline{U}_{i\ AMR}(x)\right)^2}{n}}. \quad (8)$$

Figure 43 shows the RMSE values across a rotor area normalized at the -4 RD rotor plane at different discretized streamwise distances. These streamwise locations are tied to the data output planes from AMR-Wind.

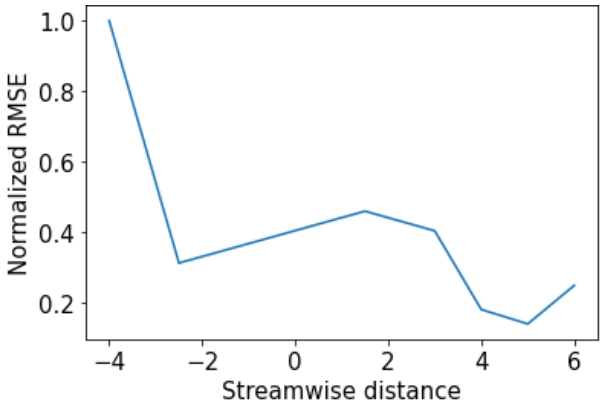

Figure 43: Normalized RMSE at streamwise distances {-4, -2.5, 1.5, 3, 4, 5, 6} RD in RP using GCH model

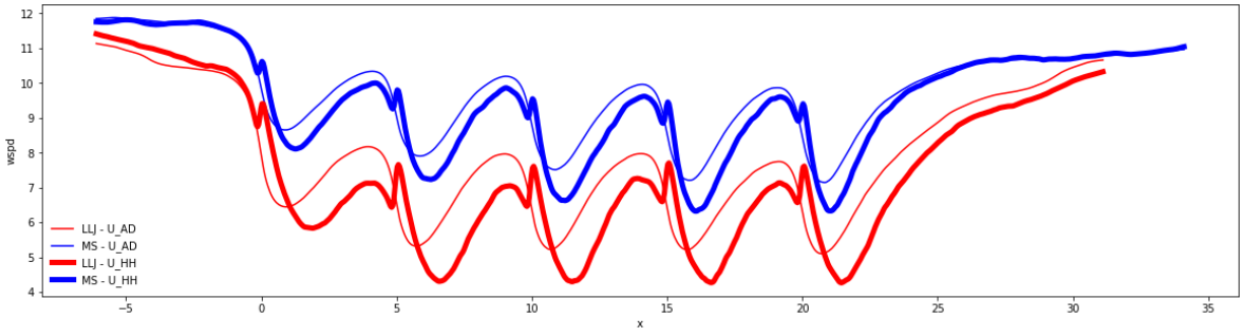

Figure 44 Comparison of hub-height and rotor-disk averaged wind sppeds for the monotonically sheared (blue) and LLJ turbulence (red).

However, as shown in Figure 44, the velocity magnitude averaged over the rotor area is very well represented by a single point velocity magnitude at the rotor center. Specifically, the LES data from AMR-wind gives us continuous flow field data (along streamwise direction) within a vertical plane passing through the turbine CL. Therefore, we can use this to extract the continuous variation of any desired velocity measure, in this case the single-point velocity at hub height, to compare outcomes from FLORIS and AMR-

Wind as shown in Figure 45. We note that in these comparisons, we convert the velocity into available power using $P = \frac{1}{2}\rho A\bar{U}^3\xi$.

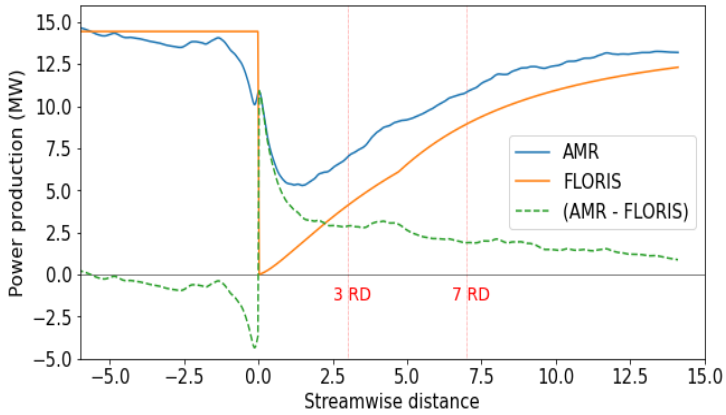

Figure 45: Power production comparison between FLORIS with GCH model (orange line) [$k_a = 0.38, k_b = 0.004, \alpha = 0.58, \beta = 0.077$], AMR-Wind (blue line) and the difference (green dashed line) for initial $\bar{U}_\infty = 12$ m/s, $TI = 9.66\%$

Using such analysis, we reported in the milestone reports 4.1 and 4.2, the tuned parameters that provide the best agreement with LES data from AMR-Wind simulations given for MS and LLJ conditions in Table 7 and Table 8 respectively. Since we are dealing with steady-state analytical models, the LES data was averaged to generate this comparison. Also, only the U-component velocity inflow was available as an input with the initial V-component velocity inflow set at zero as default, we decided to load the magnitude of all components in the U-component as initial conditions. The *loaded* U-component corresponded to a wind turbine generator of region I (Annual average wind speed of 10 m/s) instead of reflecting the true classification of the wind turbine based on its actual U-component value of region II (Annual average wind speed of 8.5 m/s) as per the IEA definition of the 15MW reference turbine [4]. Another step was taken to tune the parameters independently of the TI, thus setting $k_a = a_s - 0$ to decouple the tuning exercise. Additionally, it is important to note that the default values of the tuning parameters in FLORIS are based on experimental observations of wind turbines in region II, thus the expected mismatch between default and tuned values in Table 7 and Table 8. Secondly, we think these tuned parameters depend on the atmospheric conditions and the specifics of the tuning process (i.e. the cost function that is being minimized) and could lead to variability from published results.

Table 7: MS – Initial conditions and tuned parameters in FLORIS to match AMR-Wind predictions

Wake deficit models			**GCH**			**CC**		
Parameters	TI [%]	$\bar{U}_\infty$[m/s]	k_a	k_b	α	a_s	b_s	c_{s2}
1 WTG	9.66	12.0	0	0.04	1.40	0	0.065	0.115
5 WTG	10.0	11.7	0	0.05	1.70	0	0.145	0.120
Default	-	-	0.38	0.004	0.58	0.179	0.0119	0.133

Table 8: LLJ – Initial conditions and tuned parameters in FLORIS to match AMR-Wind predictions

Wake deficit models			GCH				CC		
Parameters	TI [%]	$\bar{U}_\infty$[m/s]	k_a	k_b	α	θ	a_s	b_s	c_{s2}
1 WTG	12.3	11.3	0	0.025	3.00	310	0.179	0.0119	0.133
5 WTG	10.9	11.1	0	0.035	0.70	0	0	0.0580	0.100
Default	-	-	0.38	0.004	0.58	0	0.179	0.0119	0.133

Figure 46 shows the improvement of the tuned parameters in the power production plots with streamwise distance from the default values ($\theta = 310$) in using the GCH model. The power production plots for the LES data are generated from velocity obtained by averaging along vertical lines from continuous AMR-Wind flow field data (along streamwise direction) within a sampled vertical plane passing through the turbine CL. The same tuning strategy is applied for the CC model with some nomenclature difference in the input file parameters where $a_s(\equiv k_a)$, $b_s(\equiv k_b)$ and c_{s2} used to change the equivalent results.

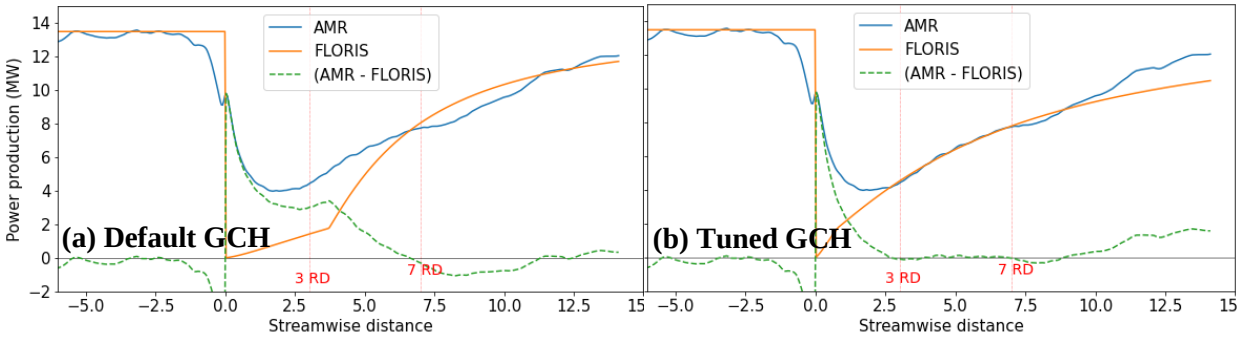

Figure 46: Power production plots illustrating the effect of the tuning parameters on the shape of the power curve with streamwise distance for (a) default settings at $k_a = 0.38, k_b = 0.004, \alpha = 0.58, \beta = 0.077$ and (b) tuned at $k_a = 0, k_b = 0.025, \alpha = 3, \beta = 0.077$ using GCH model.

However, the reasonable match in the integral power metrics don't necessarily mean the flow physics is accurately captured. We illustrate this using the following visualizations. As seen from Figure 47 The contour plots of the LES data in the rotor planes at downstream distances {-4, -2.5, 1.5, 3, 4, 5, 6} RD illustrate the rotated "bean" shape extending more than 1 RD in the immediate wake of the turbine but then dissipates into the background flow by 4 – 5 RD downstream while retaining the signature of this distortion.

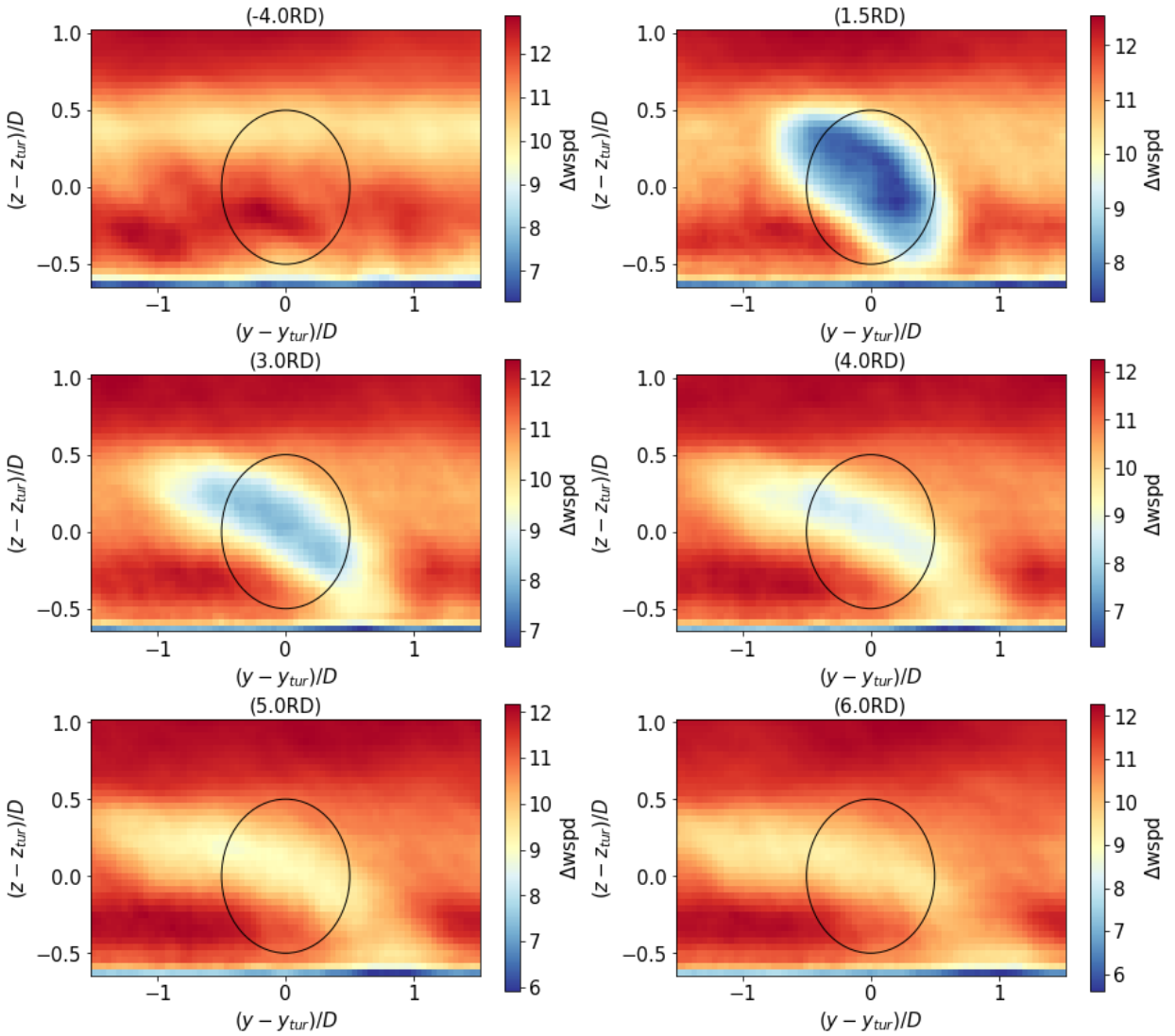

Figure 47: Contour plot of the LES wind speed magnitude from AMR-Wind in the rotor planes at {-4, 1.5, 3, 4, 5, 6} RD illustrating the rotated "bean" shape of the wake that extends well beyond 1 RD. Note the black circular line is the outline of 1 rotor diameter.

Figure 37 and Figure 38 show the contour error plots of the wind speed magnitude difference between FLORIS and AMR-Wind in the rotor planes at various distances x at $\{-2.5, 1.5, 4, 5, 6\}$ rotor diameters using the GCH and CC models respectively. As expected, FLORIS is unable to capture the wake effects close to and beyond the 1 RD regions. The GCH model is better able to capture the wake predictions inside the rotor diameter because of the artificial wind veer distortion introduced that is missing in the CC model.

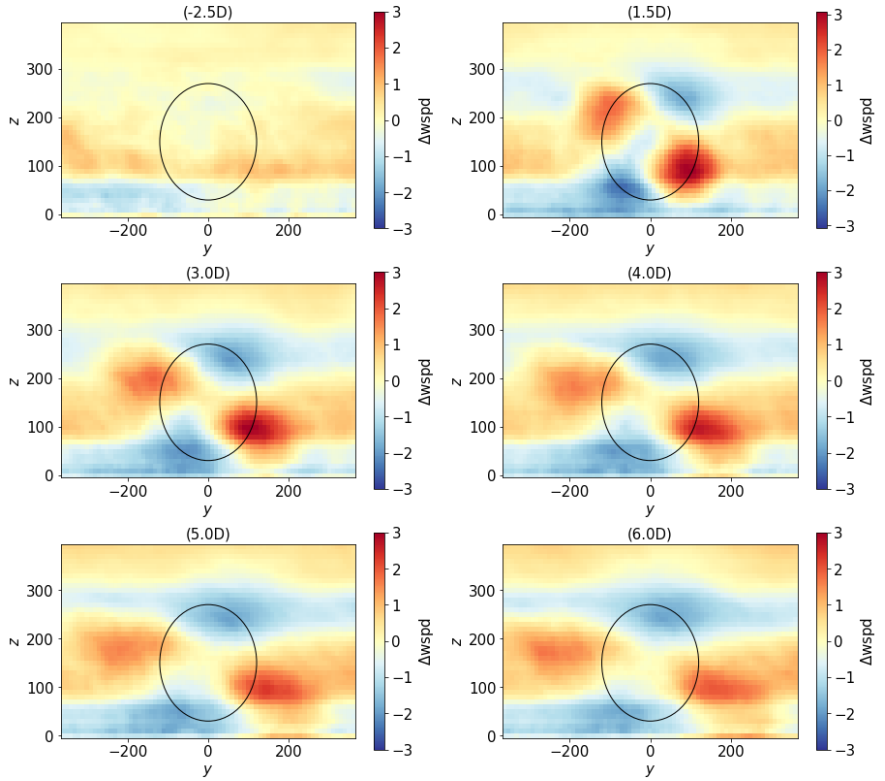

Figure 48: Contour error plot of the wind speed magnitude difference between FLORIS and AMR-Wind in the rotor planes at distances {-2.5, 1.5, 3, 4, 5, 6} RD using the GCH model [$\bar{U}_\infty = 11.3\ \mathrm{m/s}, TI = 12.3\%$] with default tunable parameters. Note the black circular line is the outline of 1 rotor diameter

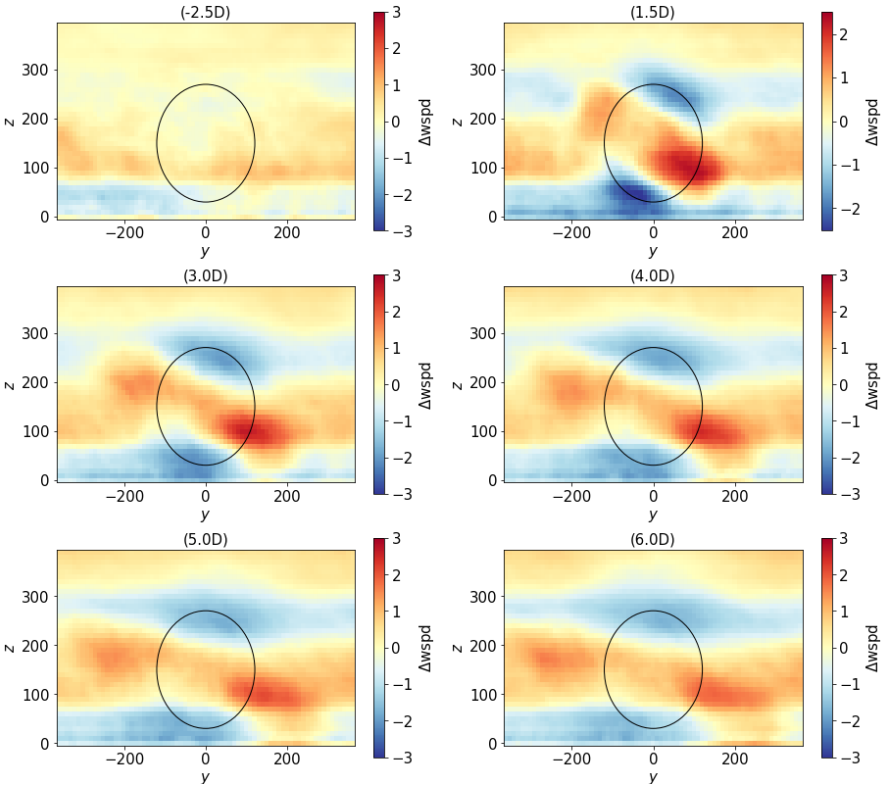

Figure 49: Contour error plot of the wind speed magnitude difference between FLORIS and AMR-Wind in the rotor planes at distances {-2.5, 1.5, 3, 4, 5, 6} RD using the CC model [$\bar{U}_\infty = 11.3\ \mathrm{m/s}, TI = 12.3\%$]. Note the black circular line is the outline of 1 rotor diameter.

In summary from the earlier milestone reports for canonical turbulence conditions, we concluded that both the tuned GCH and CC model can predict the available power and wake structure with reasonable accuracy, especially in the critical intermediate/far wake regions in the single turbine case. Concerning farm configuration, care must be taken to properly tune the models and predictions downstream of the farm is less reliable even for the better performing CC model because of global specification of the tuning parameters and absence of a blockage deficit model. For the LLJ conditions, we concluded that both the GCH and CC model can be tuned to predict the available power with reasonable accuracy but to a much lesser extent the wake structure, especially in the asymmetry across the centerline for LLJ event. Concerning farm configuration, again care must be taken to properly tune the models and predictions downstream of the farm which is less reliable even for the better performing CC model because of global specification of the tuning parameters, lack and/or limited wind veer feature and absence of a blockage deficit model. At a more fundamental level, we observe that these "analytical" or "semi-analytical" models treat the wind veer - a dominant characteristic of shallow atmospheric boundary layers – as a tuning parameter when one should use this as an input to the model. This suggests that any reasonable match in the power-prediction obtained from FLORIS may be attributed to the parameter turning process than the accuracy of the underlying wake physics model operating at its core.

6.1.2 Unsteady Wake Models

FAST.Farm is an open-source reduced order model (ROM) under development at NREL for wind farm simulation. One key distinguishing difference between the other ROM evaluated in the earlier section-FLORIS, is that FAST.Farm solves the simplified set of equations to provide unsteady characterization of wind turbines within the wind farm. FAST.Farm uses OpenFAST to solve aero-hydro-servo-elastic dynamics of each individual turbine and background velocity field is initialized using undisturbed atmospheric boundary flow. It also include modules that accounts for wake deficits, advection, deflection, meandering, and merging. These modules represent different physics domains of the wind farm. Wake-Dynamics (WD) module has several submodels for wake advection, deflection, and meandering; near-wake correction. The ambient turbulent boundary layer and array effects are all handled by the AWAE module. Additionally, the super controller and OpenFAST modules are two other models that are all linked through the FAST.Farm driver module. The following figure, Figure 50 shows all the modules and interconnection between them [3].

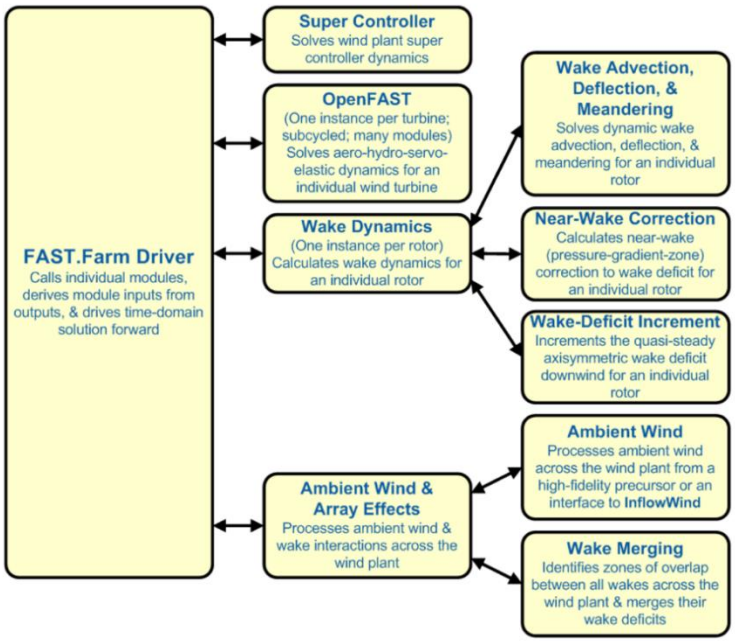

Figure 50: FAST Farm modules

FAST.Farm relies on the idea of dynamic wake meandering (DWM). The DWM model assumes that the large-scale background atmospheric boundary layer (ABL) flow are the main drivers of the wake meandering, whereas the smaller length scale eddies drive the evolution of the wake deficit downstream of the rotor. The large-scale background flow is typically provided through a low-resolution representation the undisturbed atmospheric boundary layer (ABL) generated using CFD solvers such as AMR-Wind or SOWFA. Additionally, coupling functionality with turb-sim is also available to generate the large-scale background flow. The unsteady wake-deficit evolution is solved an axisymmetric finite-difference grid consisting of several wake planes and grid nodes in the radial direction. The wake planes are aligned with the rotor centerline. Figure 51 shows a schematic of the mesh used by FAST.Farm to compute the wake evolution. Further details about the wake dynamics modules can be found in the FAST.Farm user manual [3]. In terms of inputs, FAST.Farm needs a prescription of the unsteady low-resolution background turbulent flow in the domain covering all the turbines in the wind farm. FAST.Farm also needs time evolved high-resolution undisturbed turbulent flow in a smaller region surrounding each of the turbines in the wind farm. Figure 52 shows a schematic of the various flow domains considered by FAST.Farm.

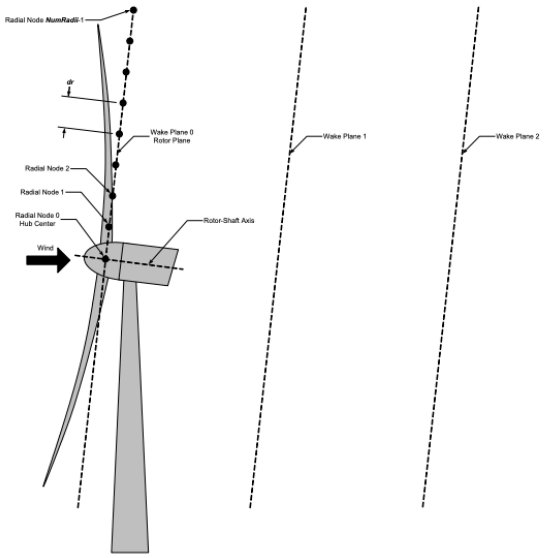

Figure 51: Finite Difference mesh used by FAST.Farm along the radial and wake directions.

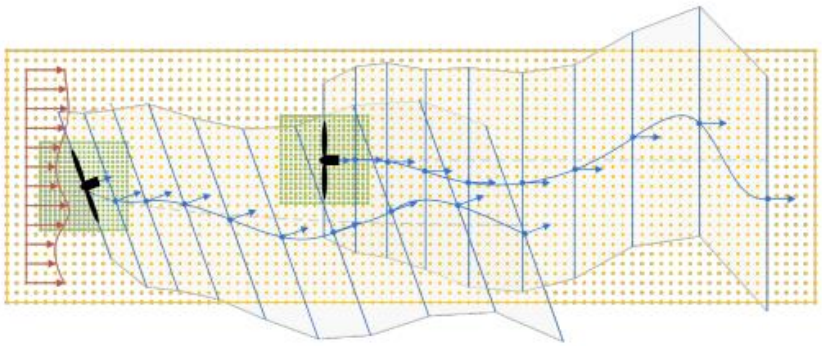

Figure 52: Schematic of the various domains considered by FAST.Farm [3]. The yellow points represent the low-resolution wind domain, and the green points represent the high-resolution wind domains surrounding each turbine. The blue points and arrows represent the centers and orientations of the wake planes, respectively, with the wake planes identified by the blue lines normal to their orientations.

In the current study, the low resolution and high-resolution flow fields are derived from the undisturbed ABL simulations that were generated as precursor simulations to support the milestones related to Task 2. The OpenFAST set up used in the single turbine and turbine array simulations performed in Task 3 is used without any modifications for all the FAST.Farm simulations described in this report. The workflow for setting up a FAST.Farm simulation is described below along with the relevant simulation parameters and computational expense.

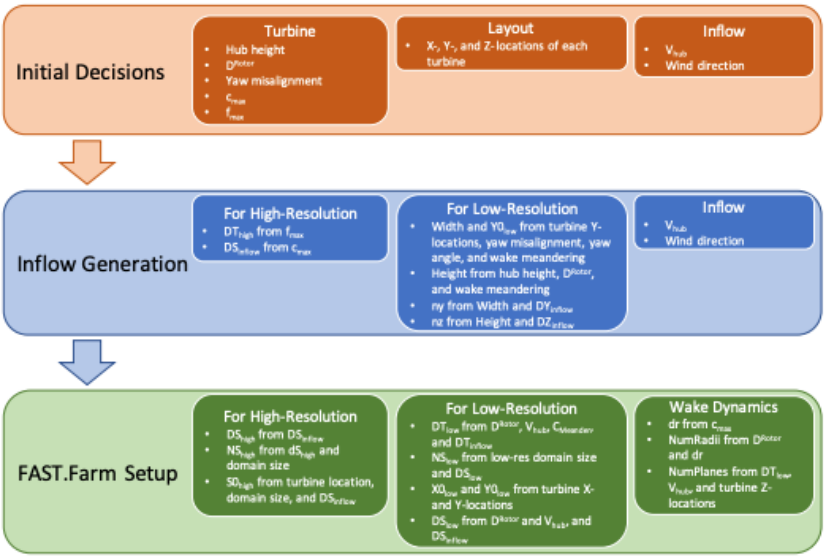

Figure 53: FAST.Farm simulation set up workflow

Figure 53 shows the workflow for setting up a FAST.Farm simulation. As a reminder, for this entire study, the IEA 15MW turbine [4] was selected for studying the impact of coastal low-level jets (LLJs). Specifically, we were interested in the accuracy of FAST.Farm predictions against LES simulations. Therefore, the turbine details and layout were set to the same as in the high-fidelity LES and thus initial decisions step will be skipped over. The best practices described in the FAST.Farm manual suggest outputting low resolution data at a frequency of $\mathbf{dt_{Low}}$ computed using the following formula

$$dt_{Low} = \frac{1.9D^{rotor}}{10\,V_{Hub}}$$

In terms of spatial resolution, the best practices in the manual suggest using $\mathbf{dX_{Low}}$ computed using dt_{Low} using the following formula

$$dX_{Low} \leq \frac{V_{Hub}^2 dt_{Low}}{15}$$

In the current study, using these formulas we estimated dt_{Low} = 1.0[s] and dX_{Low} = 10[m]. Similarly, the time step (dt_{high}) and spatial resolution (dX_{high}) of the high-resolution dataset was estimated as 0.5 [s] and 5[m] using $dx_{High} \leq c_{max}$ where c_{max} is the maximum blade chord length of the turbine. FAST.Farm was designed to read the 3D volume data output at these low and high resolution in space and time using a

custom VTK file format. FAST.Farm manual suggests designing the low-resolution domain such that it encompasses all turbines and should include wake region behind the last turbine. In the current study, for the windfarm design adopted in the LES, the low-resolution domain ([360.00, 360.00, 0.00] to [3240.0, 3240.0, 600.0]) results in ~5million cells at 10[m] resolution. The low-resolution data is output at 1[s] interval and for a total duration of ~24 minutes or 1400[s]. The resulting low-resolution data occupies 230GB of space. The high-resolution data is output at 0.5[s] apart and a resolution of 5[m] with [288, 288, 80] points over the chosen domain including a small region around the turbine ([1080.0, 1080.0, 0.0] and [2520.0, 2520.0, 400.0] with 6.635520M cells). The high-resolution dt_{high} is decided based on the highest frequencies influencing the structural excitation, including rotational sampling of turbulence and response, i.e., natural frequencies, of the pertinent structural components, fmax (in Hz).

$$dt_{high} \leq \frac{1}{2f_{max}}$$

The grid spacing in the high-resolution dataset is decided on the basis of the maximum blade chord length of the turbine, $c_{max,}$ which for the IEA 15MW is 5.77 [m]. Therefore, in this study a dx_{high} of 5[m] was chosen. In terms of other input parameters to FAST.Farm, the number of radial points and number of wake planes for the wake deficit calculation are controlled by the user. The number of wake planes is an important parameter playing a critical role in calculating wake deficits. In the current study, 92 radial points are chosen for this study. This number was arrived at in consultations with the FAST.Farm development team. Several simulations were performed to come up with an optimal estimate of number of wake planes. Eventually, the number of wakes planes was set to 160 as the best compromise against accuracy and computational time taken to complete 1 simulation. For all the other parameters the default settings, as optimized by the FAST.Farm team, were left unchanged.

6.1.2.1 Single Turbine Results

Figure 54 shows the rotor and generator characteristics as predicted by FAST.Farm. In the first 100 [s] of the simulation both FAST.Farm and LES demonstrate a strong transient fluctuating behavior due to the yaw misalignment between the incoming flow and the rotor orientation. Therefore, the comparison of results between LES and FAST.Farm is only shown between 100[s] and 1200[s].

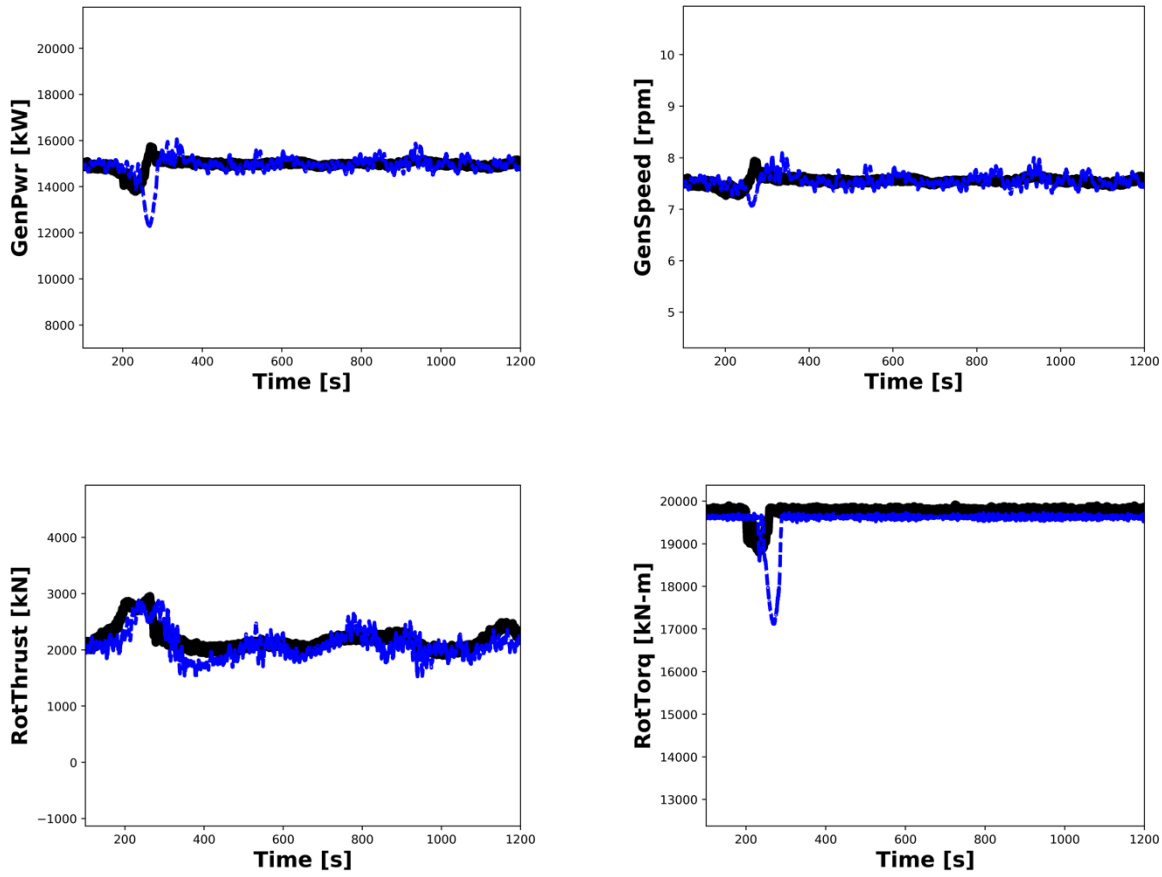

Figure 54: Comparison between rotor and generator behavior predictions between LES (blue line) and FAST.Farm (LES). Rotor Thrust in [kN] (bottom left), Rotor Torque in [kN-m] (bottom right), Generator power [kW] (top left) and Generator speed [rpm].

Overall, as can be observed from Figure 54, the FAST.Farm results match the LES predictions accurately. Both LES and FAST.Farm predict a drop in rotor torque and an increase in thrust and power at around 200[s]. However, a small offset in time is observed in the FAST.Farm predictions. As explained earlier, only undisturbed boundary layer flow is input to FAST.Farm and all the turbine induction effects along with wake deficits, wake meandering are computed by the FAST.Farm. The source of the delayed response in FAST.farm is not clear at this time. In terms of predictions of loads experienced by the rotor, Figure 55, shows edgewise and flapwise blade moments. As can be observed from Figure 55, FAST.Farm accurately reproduces the trends seen in the LES predictions.

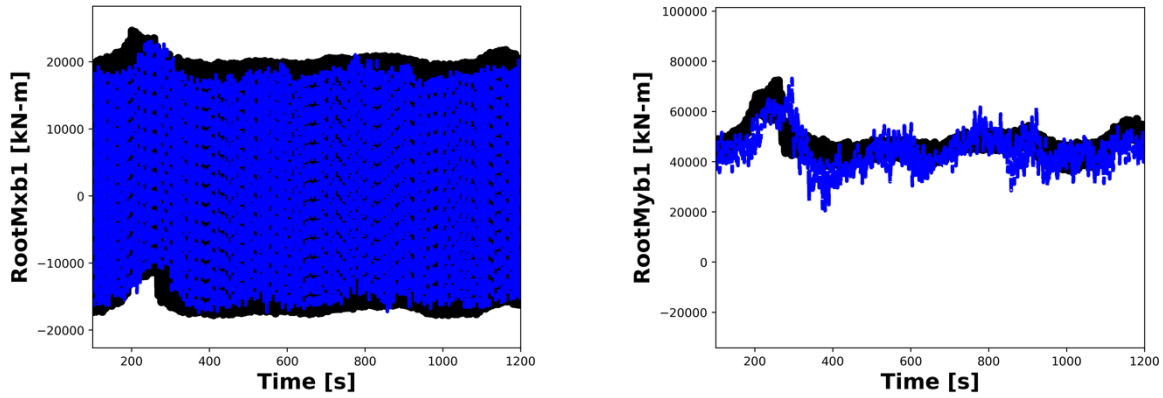

Figure 55: Comparison of Edgewise [kN-m] and Flapwise blade moments [kN-m] predictions from FAST.Farm (Black) and LES (Blue).

Figure 56 shows Tower-top/yaw bearing yaw moment predictions from FAST.Farm and LES. This accurate comparison between LES and FAST.Farm is to be expected as the inputs to the FAST.Farm and LES OpenFast instances are undisturbed ABL solution. We observe a good match in the mean, but the fluctuating component shows different amplitude levels. This can be attributed to the lower resolution of FAST.Farm simulations as compared to the LES. Regardless of these discrepancies, FAST.Farm seems to reproduce the loads observed in the LES.

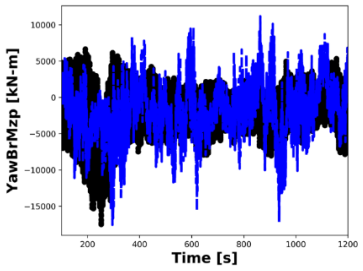

Figure 56: Tower-top/Yaw bearing yaw moment predictions from FAST.Farm (Black) and LES (Blue).

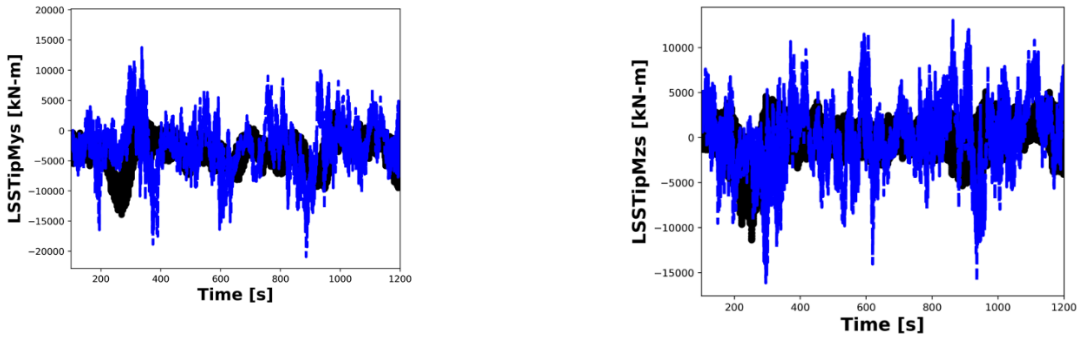

Figure 57: Low-speed shaft bending moment at the shaft tip. Moment about the ys axis (left image) and zs axis (right image). FAST.Farm results are shown using Black symbols and LES with Blue lines.

Figure 57 shows the low-speed shaft bending moments at the shaft tip. Additionally, the tower base side-to-side moment (i.e., the moment caused by side-to-side forces), tower base pitching moment (i.e., the moment caused by fore-aft forces) and tower base torsional moment are shown in Figure 58. Similar to all the other previous loads and moments predictions, FAST.Farm is able to reproduce accurately the trends observed in the LES, but with differences in the fluctuations.

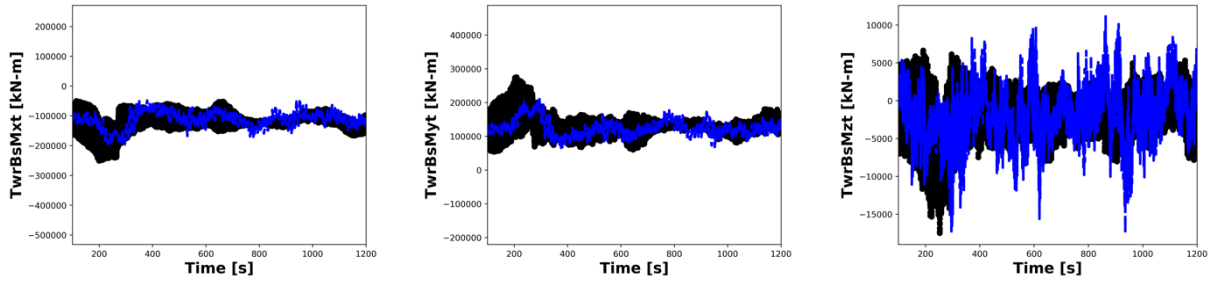

Figure 58: Tower base side-to-side moment, pitching moment and torsional moment predictions from LES and FAST.Farm.

Overall, the single turbine simulations demonstrate the potential for FAST.Farm based on comparisons against LES. However, we found FAST.Farm was found to be computationally inefficient. The NREL team worked with the FAST.Farm development team and performed the following improvements to improve the computational efficiency

1. Compile FAST.Farm in a single precision mode.

2. Decrease the sampling frequency of the high-resolution domain.

With these changes significant improvement in time to solution was observed allowing us to perform single turbine simulation in two hours on a single eagle node. For five turbine simulation using FAST.Farm the turnaround time for 40 minutes of simulation time was found to be around 24 hours. We note that this turnaround is comparable to that for fully-coupled low-resolution LES of a full five wind turbine array placed in a 10km x 10km domain with nearly 130 million grid cells and simulated on a GPU-accelerated resource such as the summit supercomputer at Oak Ridge Leadership Computing Facility (OLCF). Therefore, despite the allure of Fast.Farm as a CPU-driven framework, the proliferation of GPU-based computing implies low resolution LES may become more viable.

6.1.2.2 Results for Single-array of Five Turbines

Taking advantage of the improved simulation process, we performed several 5-turbine array calculations. For all these calculations the undisturbed atmospheric boundary layers (ABL) with low-level jets computed on the 10000[m] x10000 [m] were provided as input to FAST.Farm. As with single turbine runs, the FAST.Farm required the undisturbed flow on a low-resolution domain (30.0 [m]) encompassing all the turbines and a high-resolution domain (0.5[m]) surrounding each of the turbines. The low-resolution domain was input to FAST.Farm at 4.0[s] time intervals whereas the high-resolution domain was input at 0.5[s] intervals. These were calculated using the best practices recommended by FAST.Farm [3]. The high-resolution spatial and temporal resolution are determined by maximum blade chord length of the turbine and highest frequencies influencing the structural excitation, including rotational sampling of turbulence and response, respectively. The FAST.Farm simulation for the 5-turbine array was computed for total duration of 2400 [s] on a single node (on NREL's Eagle supercomputer) in single precision and was parallelized using OpenMP programming model where every OpenFAST instance for each turbine was initiated on a separate thread. The 5-turbine FAST.Farm simulation takes approximately 24 hours. Figure 59 shows the velocity contours along a plane passing through all the turbine pad locations in the 5-turbine array. Wakes, with significant velocity deficits, originating from each of the 5 turbines can be clearly seen in the low-resolution domain output by the FAST.Farm. The wake characteristics behind each of the turbine is shown in Figure 60.

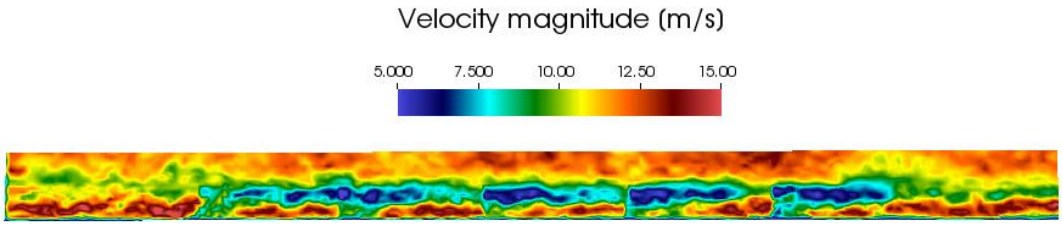

Figure 59: Velocity magnitude contours along a plane passing through all the 5-turbines. Instantaneous image is extracted at 2000 [s] from the low-resolution domain output by FAST.Farm.

From the instantaneous velocity magnitude contours shown in Figure 60, FAST.Farm predicts skewed wake shape centered around the rotor center and distorted due to the wind veer effect. This effect is also clearly observed in LES results shown in the earlier sections (Figure 47). These figures show the capability of FAST.Farm to reproduce the wake meandering due to the background motion with only undisturbed flow as the input. The axial and radial wake deficits from the waked turbine, turbine #4, is shown in Figure 61. FAST.Farm predicts -2.5 [m/s] axial velocity deficits at 5D behind the waked turbine, turbine #4.

Figure 62 shows the generator power from each of the turbine in array. The predictions from the first turbine in the array computed by FAST.Farm and LES match accurately. However, the power production power production from the downstream waked turbines is not observed to be decreasing contrary to what was observed in the turbine array LES simulations. FAST.Farm is predicting a deep wake from each of the turbines but somehow it fails to account for this reduction in inflow velocity when sending inputs to the OpenFAST to solve aero-hydro-servo-elastic dynamics of each individual turbine. This effect can be clearly observed in the rotor-disk averaged velocity profiles being output by OpenFAST, Figure 63, where waked turbines fail to show any reduction in velocity. The project team is interacting with the FAST.Farm development team to identify the primary culprit behind this problem and plans to fix this issue.

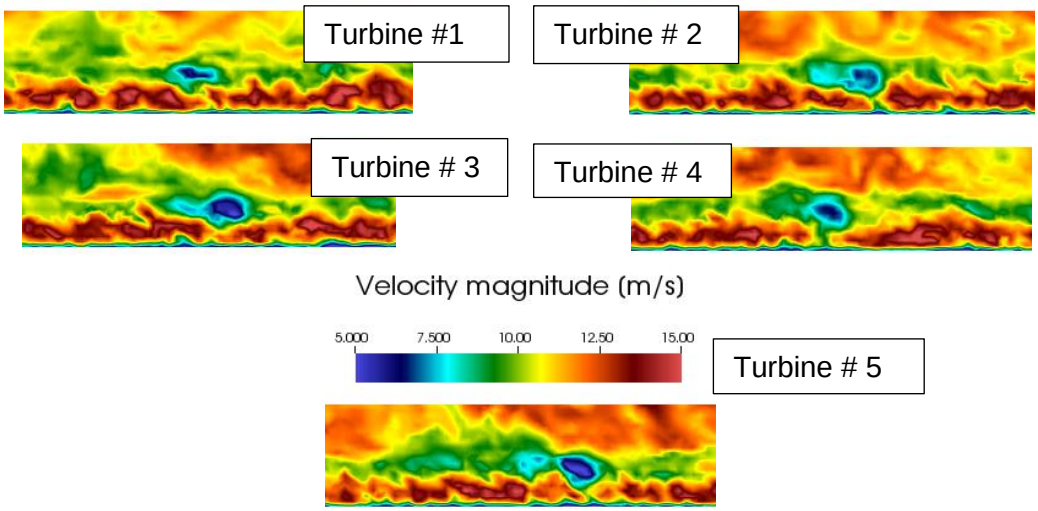

Figure 60: Velocity deficits 1.5 D behind each turbine in the array at 2000 [s]

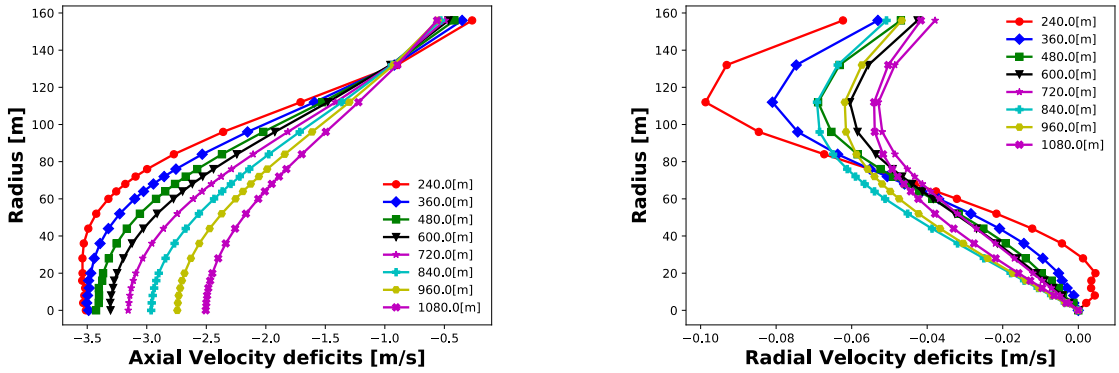

Figure 61: Axial and Radial velocity deficits behind turbine 4 in the 5-turbine array.

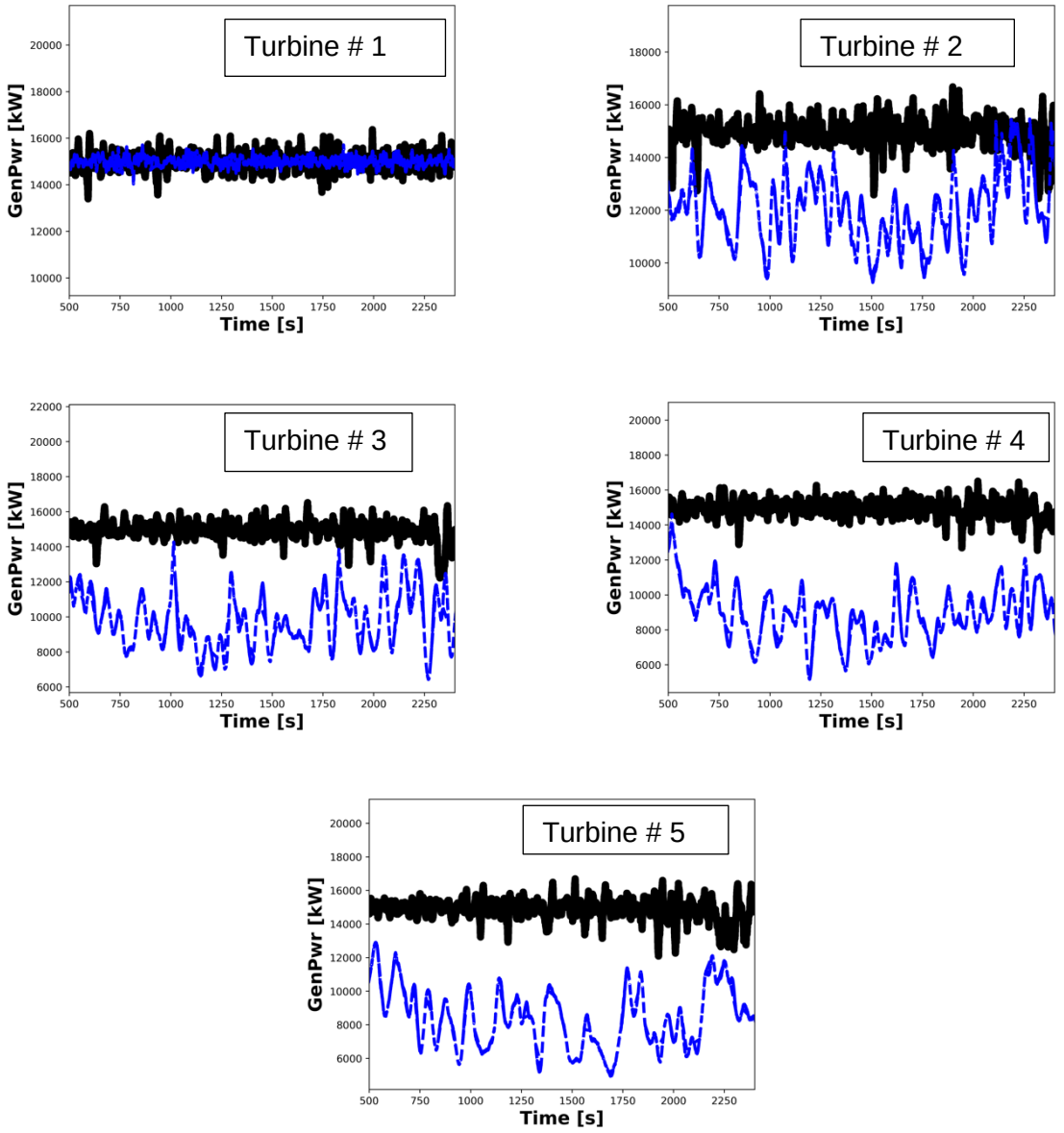

Figure 62: Generator power from each of the turbine in the 5-turbine array. Blue dashed line LES solution and line from black symbols is from FAST.Farm predictions.

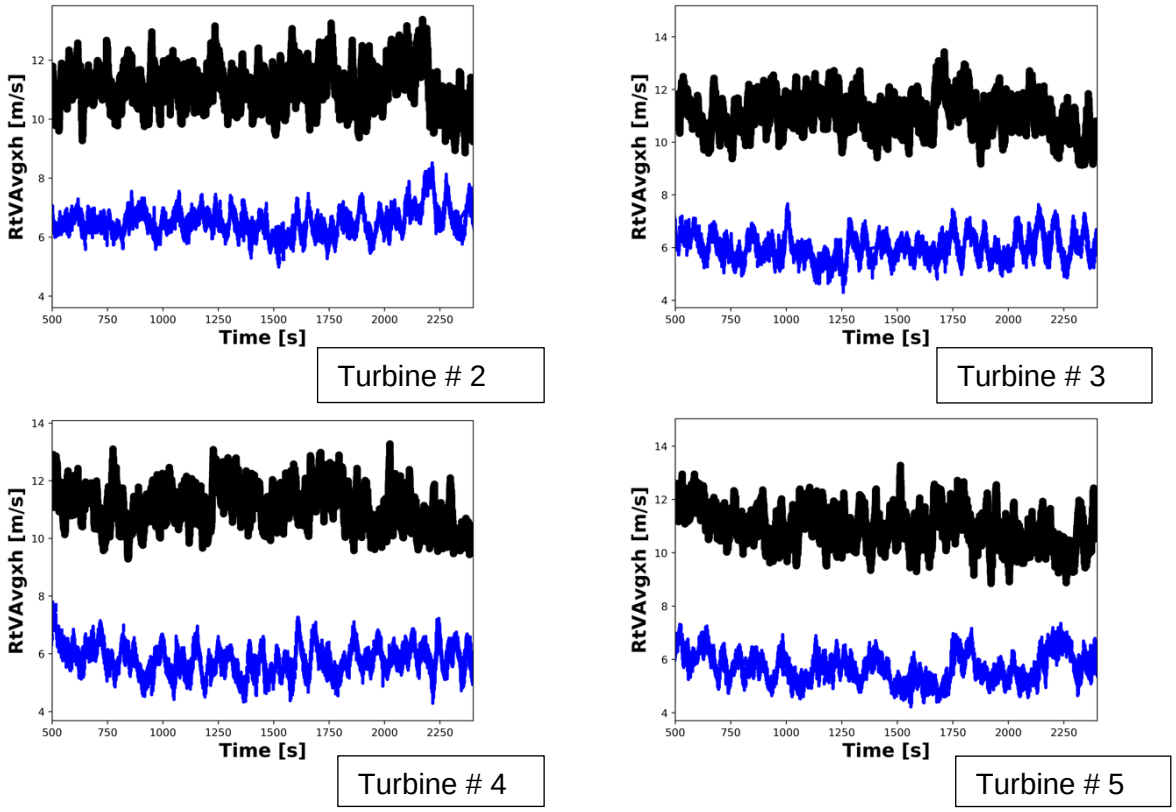

Figure 63: Rotor-disk-averaged relative wind velocity inflowing into the turbine. Blue dashed line LES solution and line from black symbols is from FAST.Farm predictions

Analyzing the five-turbine Fast.farm simulations, we see a reasonable match in the loads and power generation profiles for the first turbine (in the five-turbine array) with that of the LES. However, for all subsequent turbines in the array FAST.Farm fails to reproduce the drop in power production due to reduction in wind speed due to deep wakes observed in the LLJ case. For instance, Figure 62 shows generator power from second turbine from the five-turbine array FAST.Farm simulation.

This drop in power is primarily due to decrease in wind speed in the wake of upstream turbines. For this reason, this result suggests that the wake from the upstream turbines is not being computed properly in FAST.Farm. However, the velocity contours and profile output from FAST.Farm, shown in Figure 59 and Figure 60, clearly shows a wake prediction from each of the turbines. All this evidence points to the fact that FAST.Farm has an issue in coupling with OpenFAST where input variables to the aero-elastic turbine calculation are not accounting for wake deficits. The NREL team has been working with the FAST.Farm development team to address this issue. FAST.Farm development team suggested a few changes in terms of sampling the data and code fixes. However, FAST.Farm predictions still showed this error in the high-resolution data. At this time, this issue is still being debugged by the FAST.Farm development team and is on their high-priority list along with improving the computational efficiency of the tool.

6.1.3 Physics-resolved Models – Coarse Windfarm LES (CoWLES)

In the originally proposed research plan, we had envisioned FAST.Farm as the medium fidelity model that would allow for rapid (relative to high-fidelity computations) evaluations of wind farm performance with some loss of fidelity, yet realistic enough for engineering decision making. However, as summarized in the previous section, we found that FAST.Farm turned out to be both computationally slow for practical use as well as inaccurate for wind farm level predictions. Therefore, given the need for an affordable low-order wind farm model that can capture both the unsteady wakes and the turbine loads with reasonable fidelity, we look at single-level 'coarse' LES of wind farms as against a 3-level high-fidelity LES with local refinement around the regions of interest in the windfarms that was employed in milestones 2 and 3. A consequence of the coarse resolution is that the number of actuator points to represent the turbine also needed to be reduced. In this work, we design the coarse LES by scaling down the number of actuator points by a factor of 4 (same as the grid cell in the refinement zones) while maintaining the ratio of the actuator spreading distance to the grid cell size as shown in Figure 64.

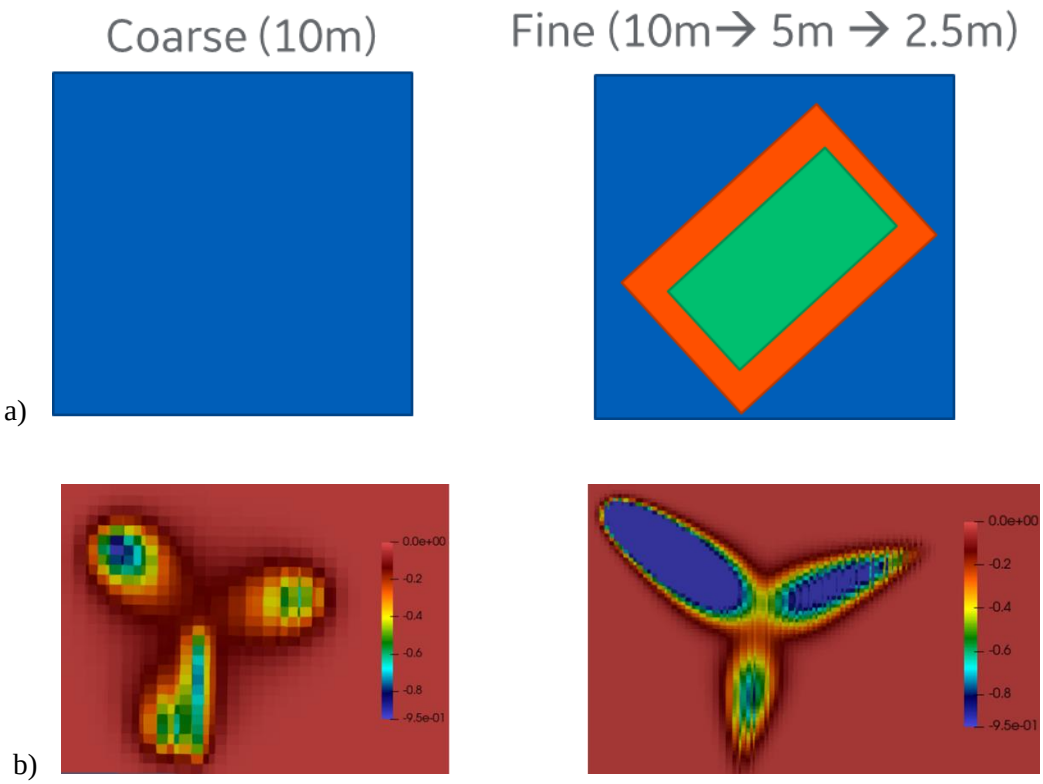

Figure 64: A comparison of the coarse (left top) and fine (right top) LES domains. The fine LES domain shows multiple refinement zones with the green being the finest, the orange being one level coarser to the

green and the blue, the coarsest level grid matching the resolution of the coarse LES domain. In the both figure, we show the representation of the wind turbine using the axial actuator force fields.

Such a low-fidelity model offers a number of advantages: (i) the analysis and simulation workflow remains the same as the high-fidelity model (HFM) to be compared against; (ii) the physics models in the ROM remain the same as the HFM; (iii) the loads channels output are the same in both models and finally, (iv) the computational cost for such ROMs is at least an order of magnitude smaller than the corresponding HFMs.

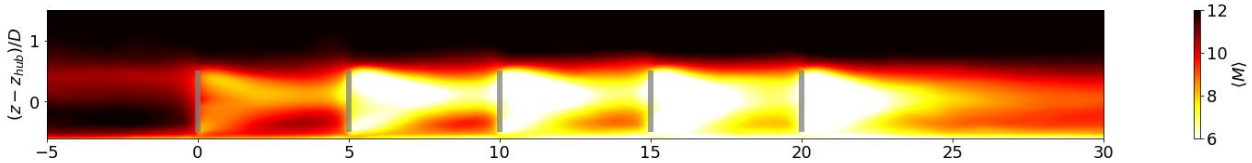

(a) Coarse LES (ROM)

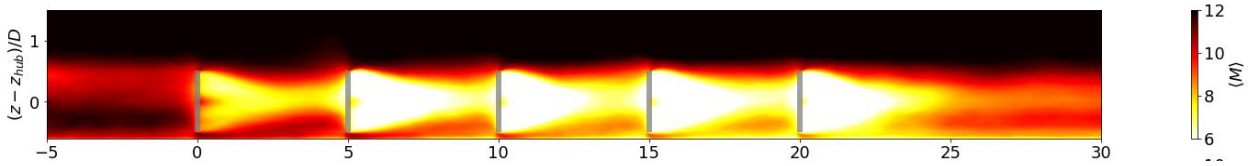

(b) Fine LES (HFM)

Figure 65: A comparison of the time-averaged coarse/ROM (top) and fine/HFM (right top) wind field for a five wind turbine array operating in the low-level jet (LLJ). We are showing a vertical plane passing through the middle of the turbine rotor disks.

In Figure 65, we compare the mean flow fields for the coarse LES/CoWLES and the fine LES/HFM in a vertical plane passing through the turbine center line. We observe that the overall qualitative and quantitative structure between the two models are mostly similar. The primary difference arises in the near-wake region structure for the first turbine which in turn impacts the evolution of the wake deficits through the rest of the wind farm. This can impact the loads being experienced by the downstream turbines in a windfarm. To assess that, we show in Figure 66 the comparison of rotor-averaged integral turbine response for the first turbine of a 5-turbine array in both LLJ and MS. The coarse LES outcomes are shown using darker colors while the fine LES (HFM) outcome is shown using lighter colors. Overall, we note that in both the LLJ and MS turbulence, the coarse LES ROM captures the broad temporal characteristic of the time series of the HFM. This agreement is more prominent for the unstably stratified MS ABL where the turbulence mixing helps the wake recover in short order. The sensitivity to the grid resolution is more discernible for the shallow LLJ turbulence where the wakes tend to be more persistent and deeper. Thus, the differences between the coarse LES ROM and the fine LES HFM show up over longer distances and durations for a farm operating in a LLJ. Nevertheless, the extent of the agreement

between the ROM and HFM is reasonably close allowing to adopt this coarse LES for evaluation of the different load mitigation and power-capture enhancement schemes.

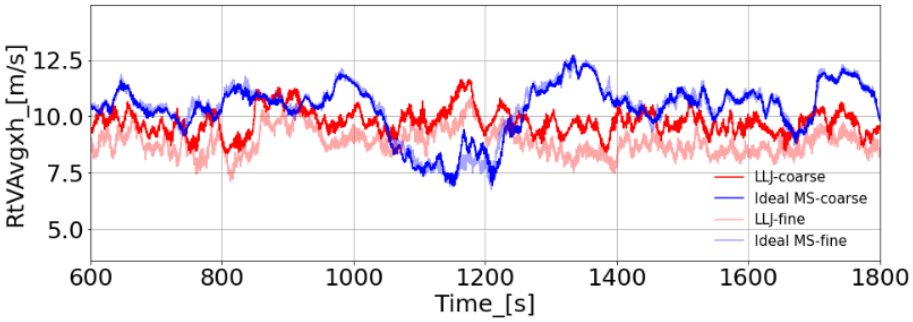

(a)

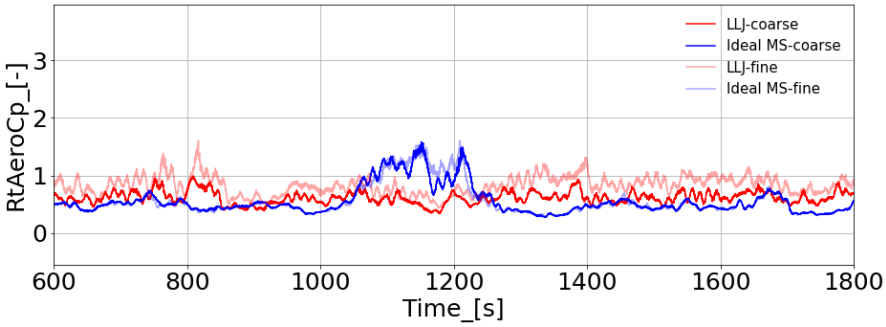

(b)

Figure 66: A comparison of the rotor-averaged axial velocity (top) and the integral aerodynamic loads for the 1st turbine of a five wind turbine array. In all these plots, we compare the coarse/ROM (in darker colors) and fine/HFM (lighter colors) data for a five wind turbine array operating in both a low-level jet (LLJ in red) and a baseline canonical ABL with monotonically shear velocity profiles. We show time-dependent data for a 20 minute period of the simulation after a 10-minute spin-up phase.

7 Summary and Future Outlook

This NOWRDC funded (with GE cost share) project allowed us to pursue a deep evaluation of the structure of the low-level jet typical of coastal Atlantic conditions and assess its impact on windfarm operations. Additionally, this also allowed us to evaluate the tools available within the Exawind suite for this purpose.

7.1 Key Takeaways

We observed that the structure of the low-level jets were similar to moderately stable shallow atmospheric boundary layers in a qualitative sense although the turbulence generation and transport processes were impacted by the non-equilibrium effects associated with such phenomena. Specifically, the key structural attributes of strong veer and shear are shared by both stable ABLs and LLJs. However, the turbulence levels within the LLJ is strongly dependent on the transport processes from above the ABL (a history-dependent nonequilibrium effect) that impacts the wake recovery within the windfarm. In terms of windfarm performance, the strong veery and shear impacts the first row of turbines. The subsequent rows are impacted by this shear and veer in an indirect way. The impact of shear is primarily felt in the wake recovery process, thereby resulting in deep wakes that extend over ten or more rotor diameters. Consequently, the downstream turbines encounter sheared velocity profiles with strong imprint of the upstream turbine-induced velocity deficits (as compared to the modest, yet significant negative shear in the atmospheric LLJ turbulent flow). Additionally, this wake-induced shear carries the temporal 1P frequencies associated the blade rotation that is absent in the background flow. The primary impact of veer is felt in the imbalanced loads across the rotor disk. In the farm set-up, the near wake flow involves swirl from the turbine rotation which dissipates in the intermediate-far wake. For the nominal windfarm spacing considered in this project, the downstream turbine sees very little of this swirl effect while the veer recovers to levels observed in the undisturbed LLJ turbulent flow, but with signatures of the 1P rotation frequency of the turbine. Consequently, the downstream turbines respond to the combined turbine-induced shear (from the wake velocity deficits) and the recovered background veer which generates complex load imbalances across the rotor disk. Additionally, these load imbalances exist not only in the mean, but also in the temporal sense due to the 1P signatures in the wake shear and veer (post mixing), thereby, impact not only the mean loads, but also the fluctuating loads. In this project we have scratched the surface of exploring the dynamics of this fluctuating turbine response and identified specific deleterious impacts that need to be mitigated. For example, the shaft out-of-plane loads show increase in the mean and fluctuating loads in the LLJ environment across the windfarm. To this end, we explored the use of different mitigation strategies, including derating, individual pitch control (IPC) and wake steering. We observed that IPC (not surprisingly) can generate significant load reductions without compromising excessively on the power capture. This is achieved by pitching each blade optimally in a phase-dependent manner which accounts for the local flow conditions. Naturally, this

would bring in challenges associated with broad-based adoption of IPC within the wind industry including designing pitch actuation systems that can withstand the rapid pitching needed to accomplish this. The other key observation is that wake steering can generate different responses from the windfarm depending on the direction of steering adopted in the presence of strong veer in such LLJ and stable ABL environments.

7.2 Potential Extensions and Next Steps

As mentioned above, we have only scratched the surface of this analysis of delineating the turbine response as well as designing mitigation strategies. We note that the findings from this LLJ project has broader implications for the generic stable atmospheric regime and therefore, highly relevant. However, the limited scope of this LLJ project allowed us to explore only a single LLJ event. One aspect of relevance to the industry is to characterize the role of LLJs with nose at different heights and how this impacts turbine reliability. Another parallel aspect of much needed investigation is the need to generalize the findings from this work to understand the role of stably stratified ABL on windfarm operations. The offshore environment is heavily skewed towards the near-neutral and stable conditions where shear and veer coexist. Therefore, it is imperative that one characterizes the role of shear and veer on turbine/farm performance in a systematic way that can be leveraged for the purposes of controller design.

From the perspective of farm-level control, one needs to revisit the relevance of wake steering strategies and reassess their effectiveness in the context of shear and veer-rich stable ABL environment offshore. Specifically, we expect that the veer and shear will generate different outcomes for different wake steering directions that what is commonly envisaged. This understanding will impact the architecture of modern farm-level control and optimization algorithms. From the modeling perspective, the fidelity of low-cost tools such as FAST.farm and FLORIS leaves room for improvement, especially when applied to LLJ and stable ABL environments. Specifically, the inability to accurately predict shear and veer-induced impact on the wind turbine wakes and farm level flows affects engineering prediction and design. Improving the predictive accuracy of such low-fidelity model approaches require redesigning the model kernels with functional forms that can handle shallow ABL with strong shear and veer. In the context of high-fidelity modeling, the meso-micro coupling strategy to accurately characterize the condition-specific turbulent environment, especially under stable atmospheric conditions with strong dependence on the flow history of the region requires in-depth investigation. In our study, we observed significant dependence of the meso-micro coupling strategy on the predictions which impacted the level of confidence in our predictions.

8 Reference

[1] New York State Energy Research and Development Authority (NYSERDA). 2022. “Milestone 4.1 Report – Impact of Low-Level Jets on Atlantic Coast Offshore Wind Farm Performance,” NYSERDA Report Number xx-yy (added by NYSERDA). Prepared by General Electric Company, GE Research, Niskayuna, NY. nyserda.ny.gov/publications

[2] Jennifer King, Paul Fleming, Ryan King, and Luis A. Martinez-Tossas. Controls-oriented model for secondary effects of wake steering. *Wind Energy Science Discussions*, 2020:3, 2020.

[3] Jonkman, Jason Mark, and Kelsey Shaler. Fast. farm user's guide and theory manual. Golden, CO: National Renewable Energy Laboratory, 2021.

[4] Gaertner, Evan, Jennifer Rinker, Latha Sethuraman, Frederik Zahle, Benjamin Anderson, Garrett E. Barter, Nikhar J. Abbas et al. IEA wind TCP task 37: definition of the IEA 15-megawatt offshore reference wind turbine. No. NREL/TP-5000-75698. National Renewable Energy Lab.(NREL), Golden, CO (United States), 2020.

[5] Garcia-Sanz, M. (2014). Introduction to Wind Energy Systems. Cleveland, OH: Case Western Reserve University.

[6] Lu, Qian, Robert Bowyer, and B. Ll Jones. "Analysis and design of Coleman transform-based individual pitch controllers for wind-turbine load reduction." Wind Energy 18.8 (2015): 1451-1468.

[7] Wheeler, Laura H., and Mario Garcia-Sanz. "Wind turbine collective and individual pitch control using quantitative feedback theory." Dynamic Systems and Control Conference. Vol. 58271. American Society of Mechanical Engineers, 2017.

[8] Mulders, S. P., Pamososuryo, A. K., Disario, G. E., & Wingerden, J. W. V. (2019). Analysis and optimal individual pitch control decoupling by inclusion of an azimuth offset in the multiblade coordinate transformation. Wind Energy, 22(3), 341-359.

[9] Disario, Gianmarco. "On the effects of an azimuth offset in the MBC-transformation used by IPC for wind turbine fatigue load reductions." (2018).

[10] Bossanyi, E. A., Fleming, P. A., & Wright, A. D. (2013). Validation of individual pitch control by field tests on two-and three-bladed wind turbines. IEEE Transactions on Control Systems Technology, 21(4), 1067-1078.

[11] C. J. Bay, P. Fleming, B. Doekemeijer, J. King, M. Churchfield, and R. Mudafort. Addressing deep array effects and impacts to wake steering with the cumulative-curl wake model. Wind Energy Science Discussions, 2022:17, 2022.